Charge Transfer to Solvent Dynamics in Iodide Aqueous Solution Studied at Ionization Threshold

im Fachbereich Physik der Freien Universität Berlin
eingereichte Dissertation

zur Erlangung des akademischen Grades des
Doktor der Naturwissenschaften (Dr. rer. nat.)

vorgelegt von

Alexander Kothe

Dezember 2014

Erster Gutachter: Prof. Dr. Emad Flear Aziz Bekhit
Zweiter Gutachter: Prof. Dr. Wolfgang Kuch
Disputation am 10.04.2015

Contents

List of Figures

List of Tables

1 Introduction

Water and aqueous solutions are arguably the most important liquids on earth. Their crucial role in biology, chemistry and human life cannot be overestimated. Although a single water molecule seems relatively simple, the interactions between many molecules in liquid phase are by far not fully understood and build the foundation of many research activities. These interactions lead to the quite anomalous behaviour of water. The volumetric anomalities for example, which are probably most commonly known, manifest in the decrease of the density of water upon heating in the range from 0° C to ∼4° C, and the decrease in density upon melting, which causes ice to float [1, 2]. In nature, neat water is rare, since it usually contains dissolved ions or molecules. These aqueous solutions are essential for life since they are buffer solutions and, in most cases, act as a solvent, accommodating dissolved atomic and molecular, neutral and charged, solutes.

In this thesis the early-time dynamics in the generation process of solvated electrons in a sodium iodide aqueous solution is investigated. The solvated electron has drawn the attention of many researchers since it is the smallest possible solute, exhibiting unique properties and being highly chemically reactive. This explains its important role in radiation damage of living materials [3, 4]. Solvated electrons are also known to play a crucial role in radiation-induced damage of DNA (DeoxyriboNucleic Acid) [5, 6, 7, 8]. Ionizing radiation, naturally occuring or as a result of medical treatment, eventually produces solvated electrons in water and aqueous solutions. For example, intense sunlight can generate solvated electrons in the surface water of the oceans up to a concentration of 10^{-15} M [9]. This is particularly interesting, since the generation process of solvated electrons involves electron-transfer photoreactions in aqueous (and also non-aqueous) solutions, which also play an important role in biology and solution chemistry.

Numerous studies have focused on characterizing the solvated electron, especially in water. These works can be typically divided into two main categories [10]: the studies on the early-time dynamics and the mechanisms leading to fully equilibrated solvated electrons, and the studies exploring the electronic properties of this species.

In most previous experiments on sodium iodide aqueous solution the electron transfer reaction was typically initiated by the resonant photoexcitation of a valence 5p electron of iodide (I^-) into a configuration with an electron and an iodine atom (I^0) being tight together. This structure constitutes a solvent-stabilized excited state, the Charge-Transfer-To-Solvent (CTTS) state. In this CTTS configuration, the electron is bound in a potential well originating from the preexisting

polarization of water dipoles oriented around the ion. Because of a large number of different hydration structures of iodide, already existing in the ground-state solution, the solvent cage rearrangement in the excited state leads to the population of a manifold of CTTS states, with different energies. The study of the CTTS states of simple anions in solvents is an important means for exploring ion-solvent, solvent-solvent, and electron-solvent interactions [11, 12]. In this case no solute intramolecular effects need to be accounted for. Although resonant excitation is indeed a crucial factor in previous experimental studies of the CTTS dynamics, the resonance condition is rather loosely defined since photon energies vary considerably in different experiments, typically between 5.1 and 6.2 eV [13, 14, 15, 16]. Importantly though, a significant fraction of the CTTS-state manifold, with energies fairly near the CTTS lowest state, is populated instantaneously by one-photon absorption. Relaxation of the CTTS states occurs within 100 - 500 fs [13, 15, 12]. The observed spread in time constants is associated with aforementioned structure diversity. A more detailed overview of the current understanding of the generation and structure of the hydrated electron is presented in chapter 2.

In this thesis the method of Time-Resolved - PE Spectroscopy (TR-PES) in the laser pump - laser probe scheme is used. Electron detection (as opposed to photon detection in a transient absorption study) is advantageous since the actual binding energies (BE) of the states involved can be determined through the measurement of the kinetic energy of the photoelectrons (PE). Therefore a direct spectral signature of the occurring transients is provided, allowing for their explicit distinction. The experimental considerations, which are necessary for such experiments, are discussed in chapter 3 with the focus on electron detection from liquids in vacuum, and ultrashort laser pulses.

The newly built experimental setup is presented in chapter 4. First, the improvements of sample handling, namely the recovery of liquid sample released by the liquid microjet, are explained and their advantages are discussed. Furthermore, the design of the newly built PE spectrometer is shown. The performance characteristics are presented for a broad range of kinetic energies at the synchrotron facility BESSYII. Here, the PEs originating from ionization of argon gas were recorded.

In contrast to the above mentioned resonant excitation into the CTTS states, the time-resolved PE spectroscopy study of early-time electron dynamics in low-concentration NaI aqueous solution presented in chapter 5, the main topic of this thesis, investigates the case of populating CTTS states via absorption of two photons of 4.65 eV photon energy as illustrated in Figure 5. This energy

is significantly smaller than the photon energies of 5.1 eV, 5.2 eV, 5.5 eV, and 6.2 eV [16, 15, 13, 14], applied in previous experiments to populate the CTTS state of iodide aqueous solution via direct one-photon absorption. The two-photon absorption leads to the population of highly excited continuum states with energies above the vacuum level.

The outlook in chapter 6 addresses preliminary results of time- and polarisation-resolved measurements, and a strategy for future measurements, which motivates the use of High-order Harmonics (HH) as probe.

2 Solvated electrons

This chapter represents a review of the solvated electron. The history of the solvated electron from its first observation in the beginning of the 19th century until its discovery in 1962 is depicted and its importance for chemistry, biology and life is discussed in the first section. Section 2.2 shows the different initial excitation steps which eventually lead to the generation of solvated electrons in water and aqueous solution. The current scientific knowledge of the relaxation processes occuring after this excitation is reviewed and the difference to the mechanism presented in chapter 5 is already depicted. Finally, the properties of the solvated electron in its ground and excited states are described in the last section 2.3.

2.1 Discovery and importance of solvated electrons

An electron located in a solvent unbound from atoms or molecules is called solvated electron. In a polar solvent molecules orient around the electrons to form the solvation shell. The process of solvation is based on the ion-dipole interaction, where the partial charges of the polar molecules of the solvent interact with the ion. Considering solvated electrons in water[1], the positive partial charges at the H-atoms are oriented towards the electron in the first layer of the solvation shell (see Fig. 1). Due to long-range interaction of the hydrogen bonds the solvation shell extends over several layers.

The generally accepted picture is that solvated electron occupies a quasi-spherical void in the surrounding solvent network. In water, the O-H bonds point to this void, which has a radius of 2.4 Å [17, 18, 19, 20]. This is called the cavity model of the hydrated electron. Theoretically, this cavity can be described by pseudopotentials [21, 19, 22]. Corresponding simulations agree reasonably well with experiments. A pseudopotential combines an atomic core and its inner-shell electrons to an effective potential. This approximation reduces computation time tremendously and is often used for simulations of chemical bonds.

Once this cavity structure is fully equilibrated and the properties no longer change, one speaks of the solvated electron. This cavity and the properties of the solvated electron can have different equilibrium conditions, though, according to the environment. In particular, structures can be examined in the bulk, in finite clusters of various size, at the water-air and water-vacuum interfaces, or in thin layers deposited on a metal substrate [10].

[1] In the literature the solvated electron in water is often called the *hydrated* electron. This thesis will not use this notation.

Being the smallest possible solute makes solvated electrons a benchmark system for understanding the quantum mechanics of solvation [23]. Its properties, such as chemical reactivity, diffusion constant or BE can be compared in many different solvents. For example, even though the value of the diffusion constant of the solvated electron varies in different solvents, it is larger than that of ions. Since the solvated electron represents the simplest reducing agent, a free radical, it exhibits high chemical reactivity. Once stabilized in solutions such as ammonia and in the absence of impurities the lifetime of these thermodynamically stable solvated electrons can be on the order of years.

Next, the history of the discovery of the solvated electron will be reviewed and present-day research activities will be described. The first publication related to solvated electrons is probably the laboratory book of Sir H. Davy, who observed a blue coloring after bringing potassium in contact with gaseous ammonia in 1808 [24]. In 1864, W. Weyl noticed the blue coloring after adding alkali metals to liquid ammonia and other solutions. He also found that the resulting solutions exhibit reducing properties [25]. If, for example, sodium is added to liquid ammonia the following reaction occurs:

$$\mathrm{Na_{metal}} \xrightarrow{\mathrm{NH_3\ Liq}} \mathrm{Na^+_{liq}} + e^-_{\mathrm{liq}}. \tag{1}$$

This mechanism, i.e., the detachment of an electron from Na as illustrated in Figure 1(a), had not been presented by W. Weyl at that time because a non-dividable electrical charge had just started to be discussed. A non-dividable charge, the electron, was postulated only in 1874 by G. J. Stonley [26], and detected in 1897 by J. J. Thomson. He showed that the charged particles in cathode rays, i.e., electron beams in vacuum, are independent of the cathode material and of the residual gas in the cathode ray tube [27]. Conductivity measurements of ammonia solutions containing alkali metals (Li, Na, K), performed by C. Kraus in 1908 [28, 29], revealed the negatively charged species with higher conductivity than that of anions. This species was independent of the alkali metal used. C. Kraus therefore suggested this species to be electrons behaving like anions surrounded by ammonia molecules.

With the appearance of radiation chemistry as a new field of research in the beginning of the 20th century, scientists were able to induce changes in matter by radiation. In 1952 the exsistence of solvated electron was postulated by G. Stein [30]. In 1962 E. J. Hart and J. W. Boag identified the solvated electrons in water directly after the exposure of the solution to electrons of 1.8 MeV energy. In particular, they performed pulsed radiolysis measurements on aqueous solutions and observed the solvated electron directly through its transient absorption

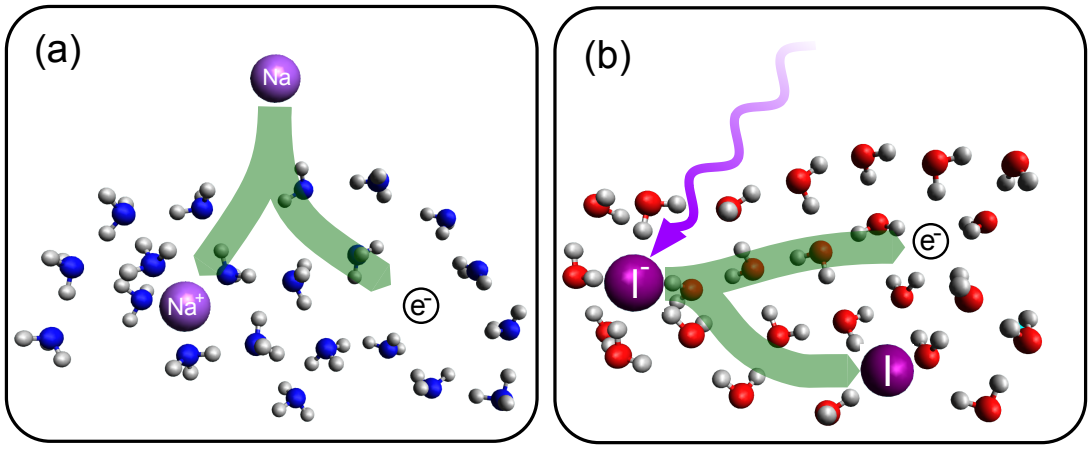

Figure 1: Two-dimensional illustration of different methods to generate solvated electrons: **(a)** After introducing sodium to liquid ammonia, electrons detach from the sodium atoms according to equation (1). The polar ammonia molecules orient themselves to form solvation shells around the cation and the electron. **(b)** In sodium iodide aqueous solution detachment of an electron can be induced by photoexciting the iodide atom with UV light resulting in an iodine atom and a solvated electron.

spectrum, which is in the range of 720 nm at room temperature (see Figure 7) [31, 32].

The significance of the solvated electron and the intermediate states, which occur directly after excitation, for radiation chemistry, and chemistry and biology in general, lies in the role as a highly reactive intermediate species in chemical reactions. It has been reported, that free secondary electrons or excess electrons of low energy (0.1 - 20 eV) play an important role in low energy radiation damage to DNA [6, 7, 8]. Here, the ionized electrons can transfer energy to the solvent by inelastic scattering. These secondary electrons can induce DNA-strand breaks of DNA in vacuum. The chemical bonds break through resonant electron excitation transfer [6, 8]. It was observed, that the yields of strand breaks in DNA in water induced by γ-radiation are three orders of magnitude higher than those in dry DNA [33]. Furthermore, precursors in the relaxation of resonantly excited water, which also yield solvated electrons (see chapter 2.2.2), cause molecular bond breaks in DNA [34].

Solvated electrons have also been reported to be involved in aerosol nucleation in the upper atmosphere [35]. Collisions of free electrons with clusters composed of water molecules give rise to solvated electrons within those clusters. In the

1990ies researchers investigated water clusters of different size and found the dependency of the electron BE on the number of molecules n in the cluster to follow BE $\sim n^{1/3}$. This dependency agrees qualitatively with a cavity model. J. V. Coe et al. extrapolated the BE from negatively charged water clusters to bulk water yielding 3.3 eV [36]. Later J. R. R. Verlet et al. found three different isomers for clusters exhibiting negative charge [37]. The BE of the isomers for different cluster sizes is shown in Figure 2. The isomer with the largest BE of the solvated electron exists only for high temperature clusters. Exprapolation to the bulk yields 3.6 eV BE which is associated with the equilibrated solvated electron in the bulk solution [38]. Until recently, the second isomer was assumed to be a hypothetical surface bound state of the solvated electron with an extrapolated BE of 1.6 eV [37]. This interpretation is questionalbe, since water cluster experiments are carried out at low temperatures at which the cluster may solidify [39, 40] and the extrapolation of the respective BEs can be associated with surface (solvated) electrons at the ice surface but not with the liquid water surface. This view is supported by most recent theoretical calculations showing that an excess electron cannot be stabilized at the liquid water surface [41]. The theoretical description of the solvated electron is based on Density Functional Theory (DFT) and provides a faithful description of solvated electrons in large water clusters and in bulk water [42].

The first ones to directly measure the BE of the solvated electron in bulk liquid water were K. Siefermann et al. (3.3 eV) [43] using the liquid microjet technique (see chapter 3.1.2). Later several other groups measured similar or slightly higher values for the BE also using the microjet technique: Y. Tang et al. (3.27 eV) [44], A. Lübcke et al. (3.4 eV) [14] and A. T. Shreve et al. (3.6 eV) [45]. The differences in the values can be attributed to somewhat different experimental conditions. In particular, N. Kurahashi found that the potential of the microjet in comparison to the grounded detector depends on solute concentration [46].

While Siefermann et al. obtained the value of 3.3 eV for the BE of the solvated electron in the bulk solution using a potassium hexacyanoferrat ($K_4Fe(CN_6)$) aqueous solution, for neat water[2] they suggest the existence of an additional species with a BE of 1.6 eV (see Figure 2), which exists for at least 100 ps. They argued that this low-BE species is a surface bound solvated electron in correspondence to the early interpretation of the second isomer found in water clusters [37]. However, the results of Siefermann et al. could not be reproduced by other researchers until today even though tackling the problem by using slightly

[2]In the case of neat water they used a 5 mM NaCl aqueous solution (see supplementary information of [43])

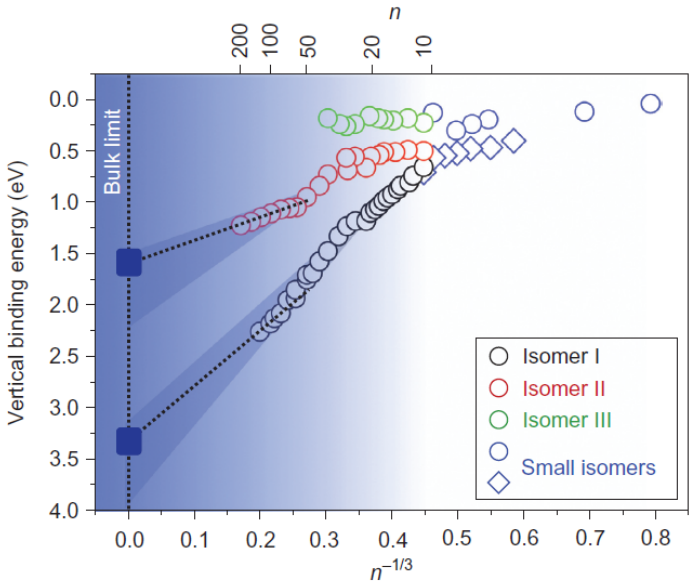

Figure 2: Experimental VBEs (or VDEs) of excess electrons in anionic water clusters of various sizes (n for the upper and lower axes represents the number of water monomers), together with experimental BE using the microjet technique [43] (blue filled squares). Blue open circles and diamonds are data for small clusters from [47]. Black (isomers I), red (isomers II) and green (isomers III) open circles are cluster data from [37]. The dotted lines interpolate between bulk data and the data for the largest anionic clusters. The shaded area represents the uncertainty of an extrapolation from the cluster towards the bulk data for $n \to \infty$. From [43].

different experimental approaches. For example, Buchner et al. found a transient state with a BE of 1.6 eV, which only exists on the order of 100 fs after excitation [15]. They assign the 1.6 eV BE peak to a first excited state of the solvated electron. Also, Y. Yamamoto et al. observe no surface-bound solvated electrons [48]. Their results indicate that surface and subsurface species, i.e., parent species such as DABCO (1,4-diazabicyclo[2,2,2]octane), create solvated electrons rather inside the bulk.

2.2 Dynamics and precursors of solvated electrons

Since its spectral identification in 1962 [31], the solvated electron was investigated intensely. Until today there are thousands of publications related to solvated electrons. Besides numerous solvents and ionic liquids in which the solvated electron

can be generated, this large number of works arises also from improving experimental techniques. In the case of radiation induced generation of solvated electrons, advances in laser technology regarding shorter pulse duration offer the possibility to examine the states and processes that occur between the initial electronic excitation and the fully equilibrated solvated electron. Further advances in liquid sample handling (see section 3.1.2) and the accompanied possibility of applying PE spectroscopy (see section 3.1.1) for probing short-lived transient states led to a deeper understanding of the ultrafast processes involved in the generation of solvated electrons, which are presented below. As discribed above, there are a number of processes which initiate the generation of solvated electrons in different solvents. Here the focus will be on water and aqueous solutions and UltraViolet (UV) excitation.

2.2.1 The CTTS state of iodide

Solvated electrons can be generated through high-energy electrons or high-energy photons like γ-rays, which ionize molecules in the solution [31, 49, 50, 51] according to the following reaction in the case of water

$$H_2O \xrightarrow{\gamma} \left(e^- + H_2O^+\right)^* \rightarrow e^-_{aq} + H_2O^+ \quad . \tag{2}$$

In the case of photons with energies below the vacuum threshold, but sufficiently high intensities can induce multi-photon processes to overcome the ionization threshold. In water, the Highest Occupied Molecular Orbital (HOMO) is the $1b_1$ level with a vertical ionization energy of 11.16 eV [52]. Such excitation above this threshold can be achieved for example by 2 photons in the UV [53, 54, 55, 56] or 4 photons of 400 nm wavelength [57, 58]. It is assumed that the ejected electron moves in a conduction band formed by collective delocalized orbitals throughout the disordered bulk [12]. It can be considered to have similar funtionality as the conduction band in solids. At these low photon energies the electron detachment occurs via electron transfer from a molecular-based to a delocalized bulk excitation [12]. Experiments investigating the ionization mechanism in the range from 8.3 eV to 12.4 eV have shed light on the ejection length of the detached electron [59]. This ejection length is approximately constant at ~ 9 Å until ~ 9 eV, and increases drastically for energies above 9.5 eV where it is already on the order of 30 Å at the vertical ionization energy (11.16 eV) [59, 52]. This increase can be explained by an autoionization mechanism, which is increased due to a minimization of nuclear reorientation of the water molecules in the transfer of the electron into the conduction band. While these experiments measured the absorption

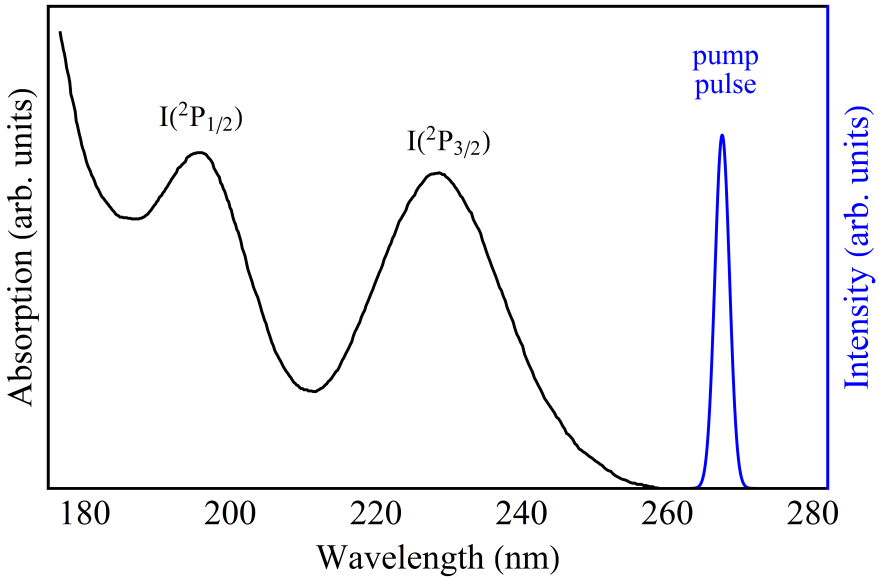

Figure 3: Absorption spectrum of a 5 mM sodium iodide aqueous solution (data taken from [60]). Absorbance leads to electron transitions from iodide into a CTTS state with $I(^2P_{3/2})$ and $I(^2P_{1/2})$ final states. For comparison the pump pulses with a central wavelength of 267 nm used in ou experiment is shown.

and its changes directly by the changes in the transmission of a probe beam, the detection of the PE would give additional insights into the autoionization processes. The measurement of PE from neat bulk water and their attribution to physical properties such as binding energies is complicated by the fact, that neat water is an insulator, which can remain (locally) charged for some time after ionization, especially in the case of intense irradiation. Experimental techniques, which introduce the sample into vacuum under constant renewal face another difficulty. For example, the liquid microjet technique uses a quartz nozzle with a channel of 10 - 25 μm through which the liquid is pressed. The friction between the moving liquid and the nozzle, which is also an insulator causes charging. In the case of neat water, charging can be minimized by adding ions to increase the conductivity of the solution. In most cases simple salts like sodium chloride or sodium iodide are used. These issues are explained in detail in section 3.1.2.

Aqueous solutions from different salts, like sodium iodide (NaI) or potassium ferrocyanide ($K_4Fe(CN)_6$) have been the basis for investigating solvated electrons [61, 14, 43]. Here the addition of salts to water produces dissolved anions, in addition to the cations, having a lower vertical ionization threshold compared to

water making it easier to detach an electron from the anion. The values for the vertical binding energies are 6.11 eV for $Fe(CN)_6^{4-}$ [62] and 8.03 eV for I^- [63] in water.

Aqueous halide solutions exhibit discrete absorption bands in the UV as shown in Figure 3 [11]. These absorption bands are due to the excitation into the so-called Charge-Transfer To Solvent (CTTS) states. For lighter halide atoms the lower CTTS states lie energetically below the vacuum level and are thus locally bound to its anion. The origination from a vertical electronic transition, and the probability, that this nonequilibrium state can relax through electron delocalization from its parent atom into the solvent gives it the name [64]. Such absorption bands are not restricted to mono-atomic species. Nevertheless, since mono-atomic ions have no vibrational degrees of freedom all observed dynamics must originate from solvent rearrangement. These absorption bands were not found in atoms or ions in gas phase experiments, which follows that CTTS states exist solely in solvated systems, where they are supported by the solvent molecules.

It is not only the solvent which affects the energetics of the CTTS states, also the neutral parent core has an influence on their formation and properties [65]. For example, absorption bands due to the CTTS state are deeper in the UV for lighter halides. Thus aqueous iodide solutions are used as a model system for these bands, since their absorption band rises approximately from 260 nm to its maximum at $\sim$ 225 nm (5.5 eV) [12] as shown in Figure 3. This wavelength range is readily acccessible with standard short-pulse laser systems. A second absorption band originating from the spin-orbit splitting of iodine lies deeper in the UV [66]. Excitation into these bands leads to the above mentioned electron delocalization and subsequent formation of solvated electrons in high yield [67].

2.2.2 The electron detachment process

As indicated in the previous sections, the initial excitation of water or aqueous solutions is followed by a series of not well understood relaxation processes, eventually leading to the generation of solvated electrons. The intermediate states are distinguished by the bonding of the electron with its parent core and the grade of alignment of the solvation shell of the detached electron at later times.

In neat water the relaxation process following two-photon excitation in the UV was resolved to the point, that three intermediate states could be identified [55]. Transient absorption pump - probe experiments revealed different temporal evolution of the transient signals at different energies. The interpretation is that one H_2O molecule is promoted into the excited state H_2O^*, which quickly transforms

into an OH:e^- complex by protonating another H_2O molecule to H_3O^+. The OH:e^- complex, where the electron and its parent species are situated within the same solvent sphere, is referred to as the caged pair [12]. The electron detachment happens on a time scale of 110 fs until the electron is surrounded by water, e^-:$(H_2O)_n$. The alignment of the water network to form the solvation shell around the electron starts after another 200 fs and is called the "hot" or "wet" solvated electron. The solvation shell reaches equilibrium conditions after another 540 fs.

For an aqueous sodium iodide solution the ionization of iodide and the solvation of the electron after irradiation is illustrated in Figure 1(b) and can be expressed by the following reaction:

$$\mathrm{Na^+_{aq}} + \mathrm{I^-_{aq}} \xrightarrow{h\nu} \text{intermediate states} \longrightarrow \mathrm{Na^+_{aq}} + \mathrm{I_{aq}} + e^-_{\mathrm{aq}}. \tag{3}$$

In aqueous iodide solutions, where the lowest CTTS state of iodide is excited by a 255 nm laser pulse, an induction time of ∼225 fs was found in the appearance of a transient absorption [12, 68]. This transient absorption is assigned to the full seperation time of the electron, where its parent anion is trapped in its ground state [12]. The transient absorption spectrum in the range from 500 to 1000 nm is shown for delay times from 0 to 1000 fs in the contour plot of Figure 4 (a). There is a shift of the transient absorption spectrum to shorter wavelengths on a time scale of 850 fs. This shift is attributed to the solvent relaxation around the newly detached electron forming the solvation shell. This conclusion is supported by experiments where ethylene glycol is added to the water environment [68] or alcohol is used as solvent [70]. Solvent changes affect the time scale of the above mentioned shift. Lowering the water temperature also slows down the solvent relaxation after the electron ejection [16].

In 2010, only months after the breakthrough of the first measurements of the BE of the solvated electron [43], Time-resolved PE spectroscopy (TR-PES) was also applied to investigate the actual ultrafast dynamics of the generation process of solvated electrons in aqueous solutions on a femtosecond timescale by Y. Tang et al. [61] and A. Lübcke et al. [14]. Both used similar experimental techniques and almost the same experimental conditions to study the excited state dynamics of aqueous NaI solutions. Note, that the experiment carried out by Siefermann et al. [43] only looked at long delay times,i.e., 100 ps after excitation. The main difference in their experiments is the excitation wavelength and therefore the resulting transition. While Y. Tang et al. excited the iodide into the CTTS band associated with the iodine I($5p_{3/2}$) state using 243 nm pulses, A. Lübcke induced the transition into the CTTS state of I($5p_{1/2}$) using pulses with a wavelength of

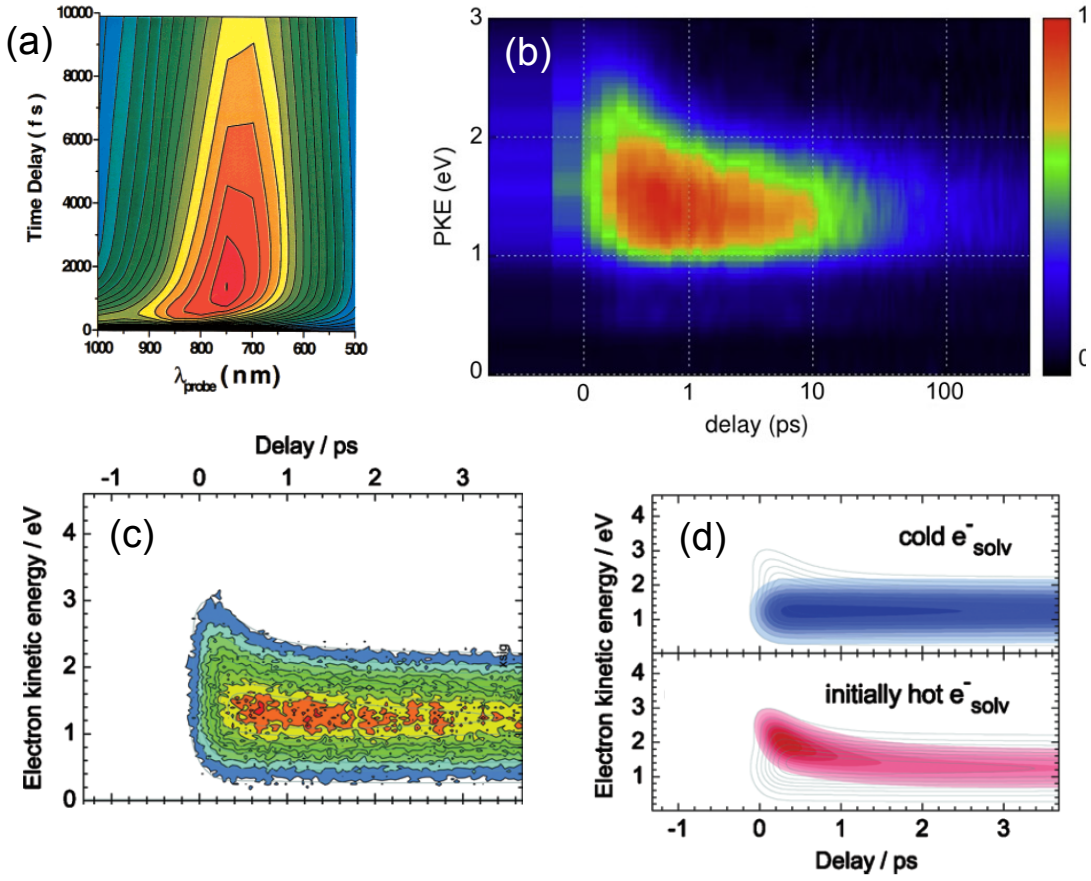

Figure 4: Transient absorption and photoelectron absorption spectra measured in iodide aqueous solutions after resonant excitation of the CTTS state. **(a)** Transient absorption spectrum after excitation with 255 nm pulses. From [68]. **(b)** Transient photo electron spectrum after excitation with 243 nm (5.1 eV). The probe was 260 nm (4.77 eV). From [61]. **(c)** Measured transient photo electron spectrum pumped with 200 nm and probed by 266 nm, respectively [69]. **(d)** Contributions of two different species ("cold" solvated electrons and initially "hot" solvated electrons) according to data analysis of (c) [69].

200 nm. The transient PE spectra are shown in Figure 4 (b) and (c), respectively. Both spectra exhibit a shift in energy of the transient signal with increasing delay times to lower electron kinetic energies, which corresponds to higher BEs of the state which is being ionized.

Y. Tang et al. evaluated their transient signals (see Fig. 4 (b)) by simultaneous fitting of the time profile and the average distribution of the measured kinetic energies of the electrons at different times [61]. They obtained three time constants, 0.65, 18 and 500 ps. These values are in good agreement with the constants obtained by Iglev et al. in transient absorption measurements perfomed on the same system. These are 0.2, 0.7 and 21 ps [16]. They also agree to values obtained by S. Bradforth and coworkers (0.2, 0.85, and $19-22$ ps), who excited water with 255 nm laser pulses [12, 68, 71]. Figure 5 illustrates the intermediate states assosiated to those time constants and their possible transition and recombination channels. For comparison, the two-photon above-threshold excitation and the observed relaxation dynamics presented in chapter 5 are illustrated in the green frame. The smallest time constant of 0.2 ps was not observed in the TR-PES experiments, which indicates similar ionization cross-sections of the corresponding states [61], i.e., the iodide ground state and its excited CTTS state. The three time constants measured by Y. Tang et al. are assigned to transitions from the CTTS state into a first and subsequent second intermediate state, which can transform into a solvated electron. In addition to these transitions, both intermediate states can also decay by geminate recombination between the electron and the neutral iodine atom. Figure 5 illustrates the scheme of the dynamics according to their interpretation. The advantage of TR-PES is the direct attainable information of the BE of the states. Here, Y. Tang et al. obtained a value for the electron BE for the CTTS band of ~ 2.6 eV [61]. The electron BE increases with time and reaches equilibrium at ~ 3.25 eV, when the electron is fully solvated.

Similar changes to higher electron BE were observed by Lübcke et al. using laser pulses with a wavelength of 200 nm [14, 69] for excitation. Their data is displayed in Figure 4 (c). In contrast to reference [61], their data evaluation yields an additional channel which decays directly from the CTTS into the solvated electron. Thus solvated electrons are being generated very fast, i.e. within the duration of the excitation ($\ll 100$ fs). They call this species *"cold" solvated electrons* and the other species *initially "hot" solvated electrons*. The representation of both contributions to the transient signal is shown in Figure 4 (d). The recombination rate of the initially "hot" solvated electrons is specified to be on the order of 1 ps^{-1}. These "hot" solvated electrons also thermalize on a subpicosecond time scale thus adding population to the "cold" solvated electrons. Those undergo

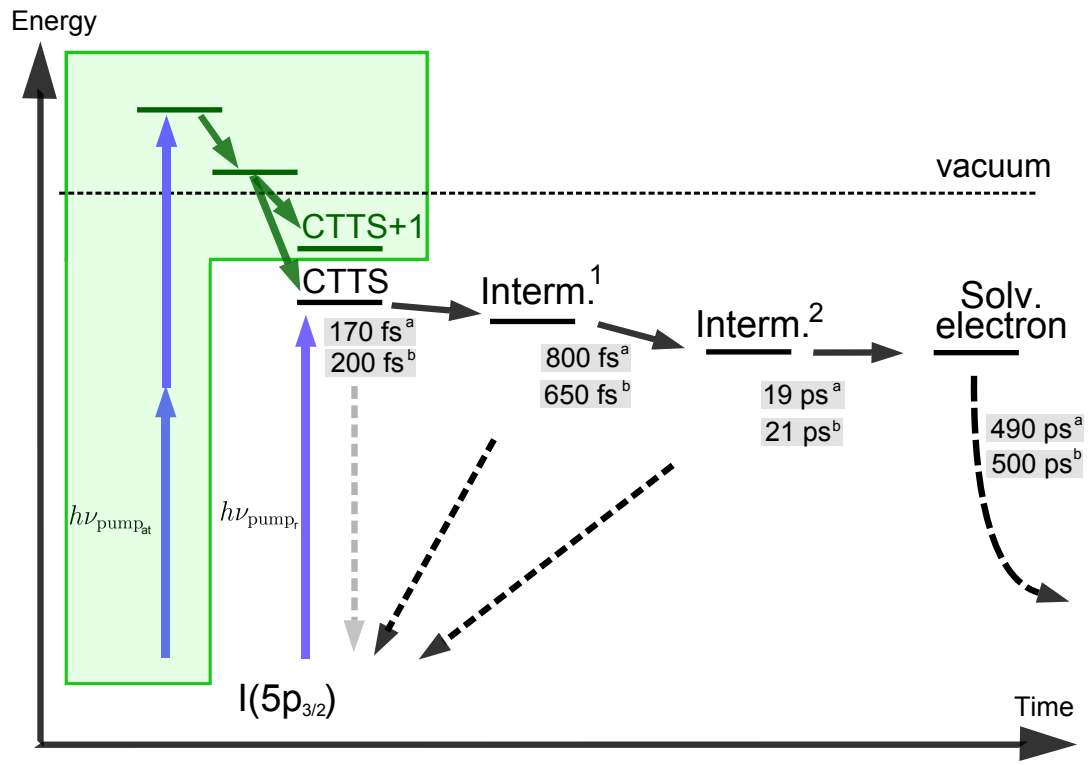

Figure 5: Scheme of the relaxation dynamics of iodide in aqueous solution following resonant one-photon excitation of the CTTS state with 243 nm pulses. The CTTS state does not undergo geminate recombination, indicated by the transparent arrow. The sequential steps, i.e. the intermediate states, in the generation of solvated electrons have the possibility to recombine with the parent iodine atom. The lifetimes of the states obtained from TR-TAS [a][16] and TR-PES [b][61] measurements are in good agreement. The two-photon above-threshold excitation and the found relaxation dynamics presented in chapter 5 are illustrated on the left and in the green frame for comparison.

geminate recombination with a rate of $\frac{1}{22}$ ps^{-1} [69].

Another way to investigate ultrafast dynamics is to measure the flourescence, which occurs at a certain time after excitation. This enables access to information about the relative energies of the involved states. The photon energy corresponds to the energy difference of the respective states. The duration of the fluorescence can unveil the decay or recombination processes of the system under investigation. If the fluorescence spectrum shows an onset, meaning it arises not instantaneously with the excitation but some time later, one can associate this signal to an intermediate state originating from the decay of the initially excited

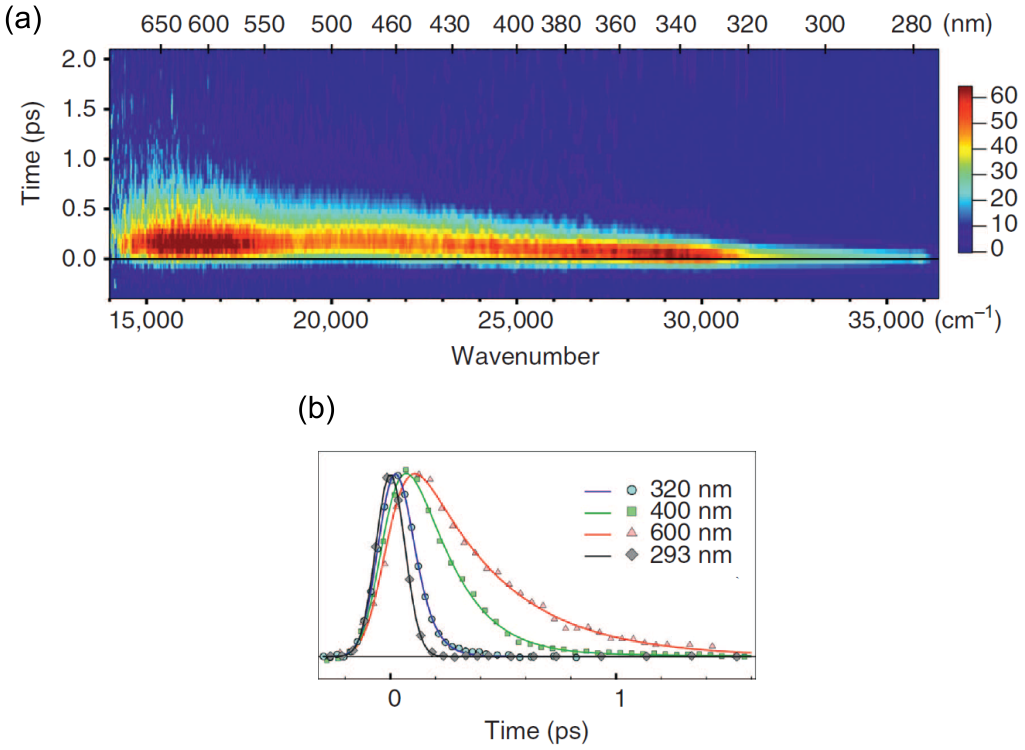

Figure 6: Fluorescence signal from a 1 M sodium iodide aqueous solution after 266 nm excitation. The Raman signal from water was substracted. **(b)** Normalized traces of the temporal evolution of the signal at different wavelengths with their representative fits (continuous lines). Both from [72].

state.

Messina et al. carried out time-resolved emission measurements from 1 M sodium iodide aqueous solution [72], by utilizing the fluorescence up-conversion technique in the UV region [73]. They excited the sample with 266 nm laser pulses and measured the fluorescence spectrum shown in Figure 6 (a). The fluorescence signals attribution to the excitation of the iodide CTTS states was verified by its linear response to variations in the iodide concentration and by variations in the pump intensity, and by its independence on the counter ion and solvent. Figure 6 (b) shows the kinetic traces at different wavelengths. The black (293 nm) and purple (320 nm) lines reveal short-lived emission on a time scale of $\sim$ 60 fs over a broad range for wavelengths shorter than $\sim$ 330 nm. For all wavelengths longer than $\sim$ 330 nm an onset of the fluorescence signal of $\sim$ 60 fs was observed, as can be seen by the green (400 nm) and red (600 nm) lines in Figure 6 (b). This onset

is concomitant with the disappearance of the emission in the UV, which indicates a sequential relaxation. The emission lifetimes in the visible range increase with increasing wavelengths from 100 fs up to 400 fs. Thus two relaxation processes were asigned to thess observations with time constants of $\tau_1 \approx 60$ fs and $\tau_2 \approx 250$ fs. The first process is argued to originate from close-range interactions with first-shell molecules rearranging to the new charge distribution similar to findings for iodide in liquid tetrahydrofuran [74]. The second process is assigned to the appearance time of the transient absorption signal of the non-emissive $I^0{:}e^-$ pair, which was quantified by ∼200 fs using TR-TAS [12, 75, 16].

2.3 Photoexcitation of the solvated electron

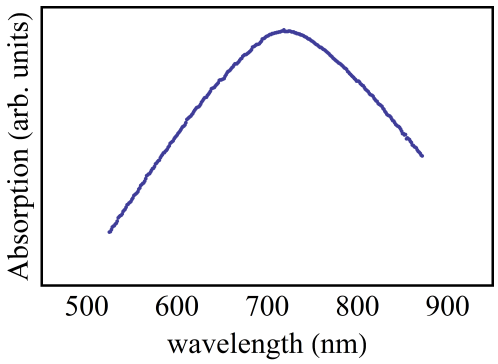

Figure 7: Absorption spectrum of the solvated electron in water at 22° C. Data taken from [76]

As discussed in section 2.2.2 in neat water the solvated electron exhibits a strong absorption band centered at 720 nm as shown in Figure 7, which gives a characteristic transient absorption signal in many pump-probe experiments, since neat water or aqueous solutions do not absorb photons at that energy. The transition induced by this absorption promotes the solvated electron from its ground s-state $|s\rangle$ into a manifold of excited p-states $|p\rangle$ within their cavity [31]. First ultrafast transient absorption experiments investigating the relaxiation of the excited p-states were carried out by P. F. Barbara and coworkers [77]. They could distinguish three time constants and named them τ_p, τ_{IC} and τ_s, which represent solvent relaxation in the p-state 50 - 80 fs after excitation, $|p\rangle \rightarrow |s\rangle$ internal conversion in 200 - 400 fs, and solvent relaxation in the s-state in $\sim$ 1.1 ps, respectively. This data was later reproduced [78, 79]. Theoretical simulations of these processes proposed two models, the adiabatic model and the non-adiabatic model [10]. Both models are depicted in Figure 8. The difference between those

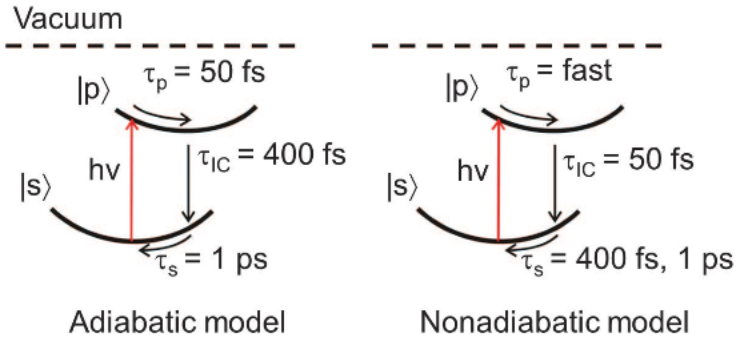

Figure 8: Relaxation mechanisms of the photo-excited solvated electron. Initial p-state solvent relaxation is followed by internal convertion and then s-state solvent relaxation. Adiabatic (left) and nonadiabatic (right) models differ primarily in τ_{IC}. From [80]

models is the asignment of the different time scales. The time scales of the above mentioned experiments were explained best by the adiabatic model.

Recent experiments by D. M. Neumark and coworkers revealed the validity of the non-adiabatic model [80]. They produced solvated electrons by resonantly exciting the CTTS state in a 100 mM aqueous iodide solution with a first laser pulse (wavelength: 239 nm). After a sufficient time of 200 ps, where all solvated electrons are equilibrated, they induce the $|s\rangle \rightarrow |p\rangle$ transition with a second 800 nm pump pulse. The system was probed using PES with a third 266 nm pulse. They found a sequential three-step mechanism, where τ_p is shorter than their resolution. Thus they do not observe relaxation of the excited p-states. The p-states convert internally to the s-states after $\tau_{IC} = 75$ fs. Solvent relaxation of the s-state occurs on a time scale of $\tau_s = 410$ fs.

3 Experimental considerations

3.1 Photoelectron spectroscopy from liquids

3.1.1 Photoelectron spectroscopy

PhotoElectron (PE) spectroscopy is an important tool for accessing the electronic structure of matter in gases, solids and even liquids. It is based on the photoelectric effect which was discovered by H. Hertz in 1887, who observed that the creation of electric sparks due to illumination is easier for smaller wavelength [81]. The photoelectrical effect was explained by A. Einstein in 1905 by postulating discrete wave packets (photons) as light energy carriers [82]. A detailed historical development of PE spectroscopy can be found in reference [83]. In PE spectroscopy, a sample is illuminated by monochromatic light capable of ionizing an atom or molecule in the sample leading to the ejection of a PE. From the kinetic energy E_{kin} of the PE and the energy of the photon, $h\nu$, the binding energy (BE) of the ionized state can be derived by

$$BE = h\nu - E_{kin} - \phi \quad . \tag{4}$$

In the case of solid samples, BE is usually given as a positive value with respect to the Fermi level, ϕ is the work function of the material, which is the energy difference between the vacuum and the Fermi level. Binding energies in gaseous samples are usually represented with respect to the vacuum level, which is defined as the energy of a motionless free electron in 'perfect' vacuum. In liquids it is also convenient to refer to the vacuum level since most liquids are insulators for which a Fermi level can not be explicitly defined. This convention is used throughout this thesis.

Besides the direct determination of binding energies, PE spectroscopy gives access to a lot more important information of an atomic or molecular system. In X-ray PE spectroscopy (XPS) X-rays are used to determine BE by ionizing the core levels, which can be used to assign specific atoms in the sample. This is also referred to as Electron Spectroscopy for Chemical Analysis (ESCA). A different chemical environment, for example a bond in diatomic molecules or the ligand field in macro-molecules lead in general to variations of BE and thus of the measured kinetic energy of the photoelectrons. Even the environment of macro-molecules affects the configuration of the core level electrons of specific atoms. An example is hemoglobin. Its active center, i.e., a heme group with an iron in its center, can bind oxygen in the lungs and transfer it to the tissues.

This function depends strongly on the molecular environment. In contrast to hemoglobin in a buffered aqueous solution, dried hemoglobin has a different X-ray absorption spectrum for the iron L-edge [84], showing a significant difference in the configuration of the valence electrons.

In this thesis, XPS was used to calibrate and characterize the TOF spectrometer. In particular, the $2p_{1/2}$ and $2p_{3/2}$ core levels of Argon were ionized. From the well-known ionization potentials [85] and photoionization cross-section [86] of these states the energy resolution and the collection efficiency of the spectrometer could be quantified.

In addition to the PE from direct ionization, core level ionization is usually accompanied by the emission of another electron. The ionized system with a vacancy in the inner shell or the core level can be considered an excited system, which relaxes within the core hole clock by emission of a second electron or the emission of a photon. The emission of another electron is called an autoionization process, and mostly originates from the so-called Auger-decay. This non-radiative electronic relaxation is more probable for lighter elements (C, N, O, ...) than radiative decay [87]. The vacancy in the inner shell or core level can be filled by an electron from the valence band while transfering the energy to another electron. This electron is emitted and leaves the system in its 2+ charge state. Its energy is independent of the photon energy and depends only on the energy difference of the states involved in the so-called normal Auger decay.

Auger decay can also be induced by promoting an inner-shell or core-level electron into an unoccupied, but bound state of the system. This excitation is resonant in this case and thus requires discrete photonenergies. The emission of this Auger electron leaves the system in its 1+ charged state and is called resonant Auger decay. The emitted electron can originate from the simple falling back of the same electron into the vacancy, which resembles the PE signal from direct ionization. This process is called participator Auger decay. In all other cases, the excited electron serves as a screening charge. In the so-called spectator Auger decay, the emitted electron kinetic energy is increased.

Below photon energies of 100 eV one speaks of UPS (Ultraviolett Photoelectron Spectroscopy). This energy range is used for the investigation of valence electrons due to the higher absolute resolution compared to XPS. In the beginning of this century a resolution of 3 meV at a kinetic energy of 20 eV of the PE could be achieved, while it is on the order of 50 meV for PE with 500 eV kinetic energy [88]. Therefore, UPS is a standard tool for studying the electronic bandstucture in solids and for example differences due to variations in impurities. Due to the relatively short mean-free-path of the PEs in solids (sim10 nm), UPS is a

standard tool to explore solid surfaces. For example, the binding of adsorbed species to the surface and their orientation can be studied.

Angular-Resolved PE Spectroscopy (ARPES) provides the possibility to determine not only kinetic energy but also the angle under which the electron is ejected for the sample. This enables direct observation of the Fermi surface and underlying electronic structure of crystals, which are the basic concepts necessary to describe all the electronic properties of solids and to reveal the nature of interactions of the electron with the periodic crystal potential or inhomogenities of the crystal lattice due to defects or impurities [89]. The most general form of a Photoelectron Angular Distribution (PAD) is given by

$$I(\theta,\phi) \propto \sum_{L=0}^{L_{\max}} \sum_{M=-L}^{L} B_{LM}\ Y_{LM}(\theta,\phi) \quad , \tag{5}$$

where $Y_{LM}(\theta,\phi)$ is a spherical harmonic function, and B_{LM} is a coefficient that depends on the dynamics of photoionization, the geometry of the experiment, the orbital, from which the electron is ejected, the spacial distribution of the sample, and the photoionization energy [90]. Equation 5 rests on the fact, that a PE wavefunction can be expressed in terms of a superposition of spherical harmonics.

In the case of linearly polarized light and an isotropic ensemble of the sample, the PAD can be expressed by

$$I(\theta) \propto (1 + \beta P_2(\cos(\theta))) \quad , \tag{6}$$

which was shown by J. Cooper and R. N. Zare for closed-shell atoms [91]. Here, $P_2 = \frac{1}{2}(3\cos\theta - 1)$ is the Legendre polynominal of second order, and θ is the angle measured between the detection and the polarization vector of the light beam. The PAD is fully determined by the anisotropy parameter β, which ranges from -1 to 2, where $\beta = 0$ represents the case of isotropic photoemission.

An additional axis of symmetry can be introduced by ordered molecules on a surface [92] or the alignment of molecules in a laser field [93] leading to non-cylindrical symmetry with respect to the polarization vector in PAD measurements.

A complete overview of these and other methods of PE spectroscopy is given in [88].

3.1.2 Volatile liquids in vacuum

Solid samples require ultra high vacuum (UHV) to obtain clean surfaces in a preparation process and to minimize adsorption of gas onto the surface, which can be expressed in terms of L (Langmuir). 1 L is defined as the product 10^{-6} torr $\times 1$ s (1.33×10^{-6} mbar $\times 1$ s) [94]. This corresponds to the accumulation of one monolayer to the surface within 1 s at a pressure of 1.33×10^{-6} mbar. In the case of highly volatile liquids or solutions, e.g. water or alcohols, one faces high vapor pressures. For water with a vapor pressure of 8 mbar at 0° C the evaporation of one monolayer takes 100 ns [95]. This difference in the time scales of 4 orders of magnitude shows the advantage, that in the case of liquids, UHV is not required to maintain the same surface conditions.

But since PE spectroscopy inevitably requires high vacuum conditions due to the electrons strong interaction with matter, solvent evaporation necessitates additional technical effort to maintain high vacuum conditions. Evaporation can be minimized by reducing the samples surface. Since this is equivalent to a small volume, the replacement of the evaporated sample must be ensured. Otherwise sample conditions can change over time. Examples are a change in concentration of a dissolved species, where only the solution evaporates, or the size of the sample can exhibit different properties of the species under investigation as discussed in chapter 2.2.2 on the dependence of the BE of the solvated electron on cluster size. Thus permanent and steady refreshment ensures stable measurement conditions.

The first experiments on liquids in vacuum were performed by R. Wierl in 1930 using a mercury drop at the end of a capillary [96]. In the 1970ties H. Siegbahn and K. Siegbahn measured a PE spectrum from liquids for the first time [97] by using a liquid jet of 0.2 mm diameter in vacuum to investigate the C 1s, N 1s and O 1s core levels of formamide using Mg K_α radiation. Although the liquid jet method was a breakthrough for PE spectroscopy of liquids, their technique was still restricted to solutions with a low vapor pressure, e.g. formamide ($HOCN_2$), triethylphosphate ($(C_2H_5O)_3PO$), or highly saline aqueous solutions cooled down to -40° C. They also developed different techniques utilizing adhesion on a substrate surface to conduct PE spectroscopy measurements. For example, they used a wetted metal wire, where the liquid is transported on the surface of a thin wire from a reservoir to the interaction region. They were able to reach a pressure of 10^{-2} mbar for liquids with moderate vapor pressure [98]. In 1981 K. Siegbahn was awarded the Nobel prize in physics “for his contribution to the development of high-resolution electron spectroscopy”.

Influenced by gas jets for collision experiments, M. Faubel developed the microjet

technique, which turned out to be the ideal tool for measuring water and other volatile solutions in vacuum. Faubel studied the collision-free evaporation from steady-state and temperature-controlled liquid surfaces [99, 100]. Inprovements of this technique resulted in the first photoelectron spectra from liquid water and several alcohols [101, 102]. Today, many groups world-wide use the liquid microjet technique successfully for, e.g., PE spectroscopy or soft X-ray emission spectroscopy [103, 104, 43, 69, 105, 106].

In our experiments the liquid microjet is formed by a quartz capillary with a channel of 20 - 25 μm diameter at one end. The capillary is mounted in a holder and pressurized liquids produce a cylindrical micrometer-sized liquid jet. The liquid leaves the nozzle as a laminar liquid jet. After a few millimeters in vacuum turbulences will dominate and several centimeters further away from the nozzle the liquidjet will break into (ice-)droplets. The length of the laminar flow region is defined by the channels orifice diameter and the flow rate of the liquid. Measurments are only meaningful and stable when the laser beam hits the laminar flow region. We use an HPLC[3] pump (TECHLAB, ECONOMY 2/ED) that generates a very stable flow rate of $\sim$1 ml/min. The backing pressure depends on the viscosity of the liquid used, for water it is approximately 2-3 bar. A more detailed description can be found in reference [107]. The velocity v_{jet} of the jet is a function of the flow rate f set on the HPLC pump divided by the size of the orifice πr^2 [108]. For a flow rate of 1 ml/min used here, this gives a velocity of 37 m/s. Considering a repetition rate of 5 kHz of the measurement, the molecules in the jet will have moved by more than 7 mm in 200μs. This ensures a fresh sample for each lasershot as the area is less than 50μm for every measurement.

The major role of the liquid microjet technique for PE spectroscopy can be understood by taking a closer look at short electron mean free path in vapor surrounding the liquid. For example, water has a vapor pressure of 23 mbar at 20° C and 8 mbar at 0° C. The electron Inelastic Mean Free Path $IMFP$ is anti-proportional to the average electron scattering cross section σ_{el} and the density ρ_{gas} of the gas [95]:

$$IMFP \propto \frac{1}{\sigma_{el}\ \rho_{gas}} \quad . \tag{7}$$

Therefore, applying a strong gas density gradient with distance from the liquid surface improves the measurement conditions significantly by reducing the possibility of PE interacting with gas molecules. For geometrical reasons, only a

[3]High-Performance Liquid Chromatography

liquid cylinder with a diameter of a few micrometers can reduce the density of the evaporating gas on this scale. Thus, the density decreases as a function of the radial distance r even close to the cylindrical microjet. The anti-proportionality $\rho_{gas} \sim 1/r$ follows an electron mean free path s that is proportional to r. For typical experimental conditions using water jets the effective electron mean free path is on the order of 1 mm [103]. In our experimental setup the entrance of the TOF spectrometer is approximately 0.7 mm away from the liquid jet. Once the photoelectrons have passed the ~ 200 μm orifice, the mean free path is up to 1 meter, due to differential pumping of the TOF and the resulting decrease in the density of the gas, which is now proportional to r^2 since spectrometer orifice can be considered a point source for the inflax of the gas.

Another important aspect to consider is the Electron Attenuation Length (EAL) inside the liquid. It is a value for the distance where the amount of electrons of a certain kinetic energy has dropped to $1/e$ of its initial value. Attenuation can be caused by elastic and inelastic scattering of the electrons. Both processes can be expressed in terms of Elastic and Inelastic Mean Free Path (EMPF and IMPF, respectively) of the electrons. While in the case of elastic scattering, information about the electron binding energy is conserved, information about the angular distribution of the emitted PE is lost. On the other hand, inelastic scattering changes the kinetic energy of the electrons, since energy is transferred to the molecules involved in the scattering process. In water, for example, vibrational levels can be excited leading to an energy loss of the electron of 0.2 eV or 0.5 eV. Thus statements about the binding energy of the electrons origin is difficult. For electrons with a kinetic energy of 3 eV the EAL was reported to be on the order of 5 nm [15]. Recent experiments investigating the PAD of water revealed of the IMFP of electrons with low kinetic energies (< 100 eV) is shorter than theoretically estimated [109]. Hence, the electron probing depth in water, near threshold ionization, appears to be considerably smaller than so far assumed. This indicates that for these electron kinetic energies the detection of PEs from or near the surface compared to the bulk is enhanced.

Furthermore, the temperature of the microjet technique must be considered, which is reduced by evaporative cooling of the liquid in vacuum on a timescale of a few tenths of nanoseconds [99]. It was shown [99, 108] that the temperature profile along the jet axis can be discribed by

$$\frac{dT_0}{dz} = -2\frac{\dot{r_0}(T_0)}{v_{\mathrm{jet}}}\frac{\Lambda}{C_p}R_0^{-1}, \tag{8}$$

where T_0 is the temperature at a certain position z downstream from the orifice.

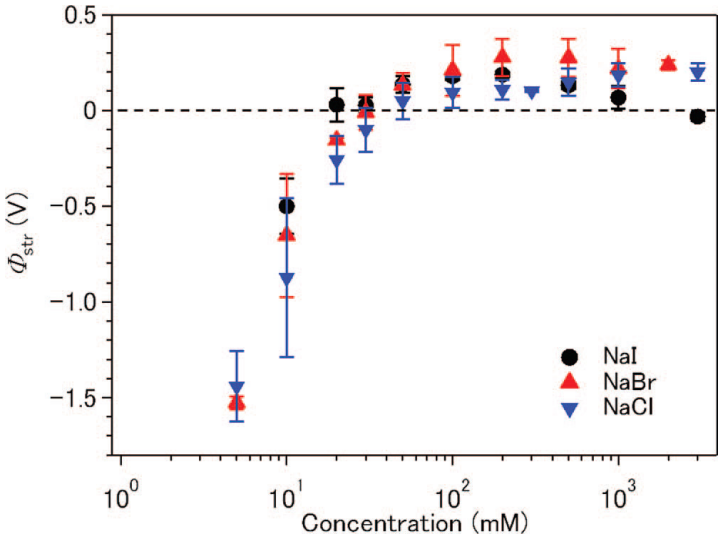

Figure 9: Dependence of the streaming potential of aqueous solutions of NaI, NaBr and NaCl on their concentration. From [63].

It is a function of the jet velocity v_{jet}, the heat of evaporation Λ, the specific heat capacity C_p and the radial ablation rate $\dot{r_0}(T_0)$, which describes the decreasing radius of the jet due to evaporation. Assuming that C_p, Λ and the densities of the vapor ρ_v and the liquid ρ_v are independent of their temperature T, and a Gaussian distribution of the mean velocity of the evaporated molecules one gets

$$\dot{r_0}(T_0) = \sqrt{\frac{kT}{2\pi m}} \frac{\rho_v(T_0)}{\rho_l} \tag{9}$$

for the ablation rate. According to the Clausius-Clapeyron relation, equation (8) can be rewritten to

$$\dot{r_0}(T_0) = r_{\text{ref}} \sqrt{\frac{T_0}{T_{\text{ref}}}}\ e^{-\frac{\Lambda}{kT_{\text{ref}}}(\frac{T_{\text{ref}}-T_0}{T_0})} \tag{10}$$

with an initial ablation rate $r_{\text{ref}}(T_{\text{ref}})$ as a reference. This equation can be solved numerically. For a nozzle orifice of 20μ m and a jet-velocity of 20 m/s the temperature will drop by 10 K after 1 mm if the initial temperature was 300 K at the orifice [110].

Besides the advantage of the constant renewal of the sample using the microjet technique, which prohibits sample damage, the friction between the moving liquid and the nozzle causes a streaming potential. This potential was measured by N. Kurahashi et al. for different aqueous salt solutions by recording O(1s) PE

spectra from evaporated water between the jet and the detector entrance [63]. They found, that the kinetic energies of the PEs varied depending on the distance between the ionization point and the liquid beam, from which the streaming potential can be determined. As shown in Figure 9, this streaming potential depends on the concentration. Extrapolation of the concentration to neat water indicates the difficulties in measuring and interpreting PE spectra. Thus ions are typically added to increase the conductivity. In most cases simple salts like sodium chloride or sodium iodide are used.

3.2 Time-resolved experiments using femtosecond laser pulses

3.2.1 Femtosecond laser pulses

After the postulation of stimulated emission by Albert Einstein in 1916 [111] the technical realisation of a LASER (Light Amplification by Stimulated Emission of Radiation) was achieved by Theodore Maiman in 1960 using a ruby crystal [112]. In 1986 the first Ti:Sapphire laser was developed by Moulton [113]. Ti:Sapphire lasers are tunable in a wide wavelength range between 650 to 1100 nm, the optical properties of the crystals allow 100 fs pulses by mode-locking with little technical effort. This makes them the commercially most sucessful ultrafast laser systems.

Typically, the shape of an ultrashort pulse can be represented by a bell shaped function. The general Fourier transfomation of a pulse is given by

$$E(t) = \frac{1}{2\pi} \int_{-\infty}^{\infty} E(\omega) e^{-i\omega t} d\omega \tag{11}$$

for the time-evolution of the electric field of the pulse in time and

$$E(\omega) = \int_{-\infty}^{\infty} E(t) e^{i\omega t} dt \tag{12}$$

for the frequency-evolution, respectively. Using standard statistical definitions to calculate the duration and the spectral width,

$$\langle \Delta t \rangle = \frac{\int_{-\infty}^{\infty} t \mid E(t) \mid^2 dt}{\int_{-\infty}^{\infty} \mid E(t) \mid^2 dt} \quad , \tag{13}$$

$$\langle \Delta \omega^2 \rangle = \frac{\int_{-\infty}^{\infty} \omega^2 \mid E(\omega) \mid^2 d\omega}{\int_{-\infty}^{\infty} \mid E(\omega) \mid^2 d\omega} \quad , \tag{14}$$

it can be shown [114], that both quantites follow the Fourier inequality

$$\Delta t \Delta \omega \geq \frac{1}{2} \quad . \tag{15}$$

This relationship leads to the uncertainty principle between time and energy and has the consequence that an ultrashort pulse must exceed a certain spectral width. Vice versa a pulse of a certain spectral width cannot be shorter than the duration of the so-called Fourier-transform-limited pulse, which is given by the equality of equation 15. For practial reasons, it is easier to measure the Full Width at Half Maximum (FWHM) of the duration Δt and the spectral width $\Delta\lambda$. Thus, equation 15 becomes $\Delta\nu\Delta t \geq K$, or in terms of the wavelength λ

$$\Delta t \geq K \frac{\lambda_0^2}{\Delta\lambda c}. \tag{16}$$

λ_0 is the central wavelength and c the speed of light. One usually assumes Gaussian shaped light pulse, which follows $K = 0.441$. Gaussian-shaped pulses can be expressed by

$$E_y = Re\left(E_0 e^{(-\Gamma t^2 + i\omega_0 t)}\right) \tag{17}$$

or by its frequency in the Fourier-transformation form:

$$E_0(\omega) = e^{\left(\frac{-(\omega-\omega_0)^2}{4\Gamma}\right)} \quad . \tag{18}$$

If this pulse travels a distance x through a transparent medium its spectrum is described by

$$E(\omega,x) = E_0(\omega) e^{(-ik(\omega)x)} \quad , \tag{19}$$

where $k(\omega) = n\omega/c$ is a frequency dependent propagation factor. Assuming $\Delta\omega \ll \omega_0$ one can use a Taylor expansion of $k(\omega)$ to get

$$E(t,x) = \sqrt{\frac{\Gamma(x)}{\pi}}\; e^{\left(i\omega_0\left(t-\frac{x}{v_\Phi(\omega_0)}\right)\right)}\; e^{\left(-\Gamma(x)\left(t-\frac{x}{v_g(\omega_0)}\right)^2\right)} \tag{20}$$

after inverse Fourier transformation, where $v_\Phi(\omega_0) = (\frac{\omega}{k})_{\omega_0}$, $V_g(\omega_0) = (\frac{d\omega}{dk})_{\omega_0}$ and $\frac{1}{\Gamma(x)} = \frac{1}{\Gamma} + 2i\frac{d^2k}{d\omega^2}x$. The phase velocity v_Φ is the propagation speed of the planar wave component of the pulse. The group velocity v_g is a measure of the delay of the envelope of the pulse after a distance x and Γ is called the form factor of the pulse depending on the second derivative of $k(\omega)$. In ordinary media,

where $v_g < v_\phi$, Γ is smaller than in vacuum [114]. As a consequence, short pulses propagating through media like lenses, filters or vacuum windows undergo broadening in the time domain.

3.2.2 The pump-probe method

The pump-probe method is often used to investigate ultrafast dynamics of a large variety of systems [114]. As illustrated in Figure 10 it needs at least two ultrashort light pulses, which are correlated in time. The photons of the first pulse interact with the sample and can either induce transitions into excited states or ionize. This instance is denoted as time zero, t_0. In many systems the relaxation of the excited system is not instantaneous but rather involves intermediate states, which exhibit certain lifetimes, transitions, transition rates, BE. In practice, one uses monochromatic light to resonantly induce a specific transition into a single excited state.

The second pulse acts as a probe to investigate the properties of the excited and evolving intermediate states. Depending on the probing techniques, one is able to characterize different dynamical aspects of the system under investigation. One way is to measure the difference in photon intensity I of the probe pulse after passing the sample between the pumped and the unpumped system directly. From this difference one may draw conclusions about the excited states. This method is called Time-Resolved Transient Absorption (TR-TA) spectroscopy and is illustrated in Figure 10. A sample in its groundstate has a transmission T of the probe pulse. According to the Beer-Lambert law,

$$T_{\lambda,\, gr} = \frac{I_{\lambda,\, gr}}{I_0} = 10^{-\epsilon_{\lambda,\, gr} l N_{gr}} \quad , \tag{21}$$

where I_0 is the pulse intensity before hitting the sample, $\epsilon_{\lambda,\, gr}$ is the samples wavelength dependent absorption coefficient, l the pathlength through the sample and N_{gr} the population of absorbers. Assuming negligible absorption of the excited states the probe pulse, passing the sample at a time Δt after excitation, exhibits a measured intensity of

$$I_{\lambda,\, ex}(\Delta t) = I_0 10^{-\epsilon_{\lambda,\, gr} l N_{gr}(\Delta t)} \quad . \tag{22}$$

By varying the delay time Δt of a given wavelength λ, the optical density $OD_\lambda(\Delta t) = \log \frac{I_0}{I_{\lambda,\, ex}} = 10^{-\epsilon_{\lambda,\, gr} l N_{gr}(\Delta t)}$ of the sample can be expressed by

$$\ln OD_\lambda(\Delta t) = \ln(N_0 \epsilon_{\lambda,\, gr} l) - \Delta t/\tau \quad , \tag{23}$$

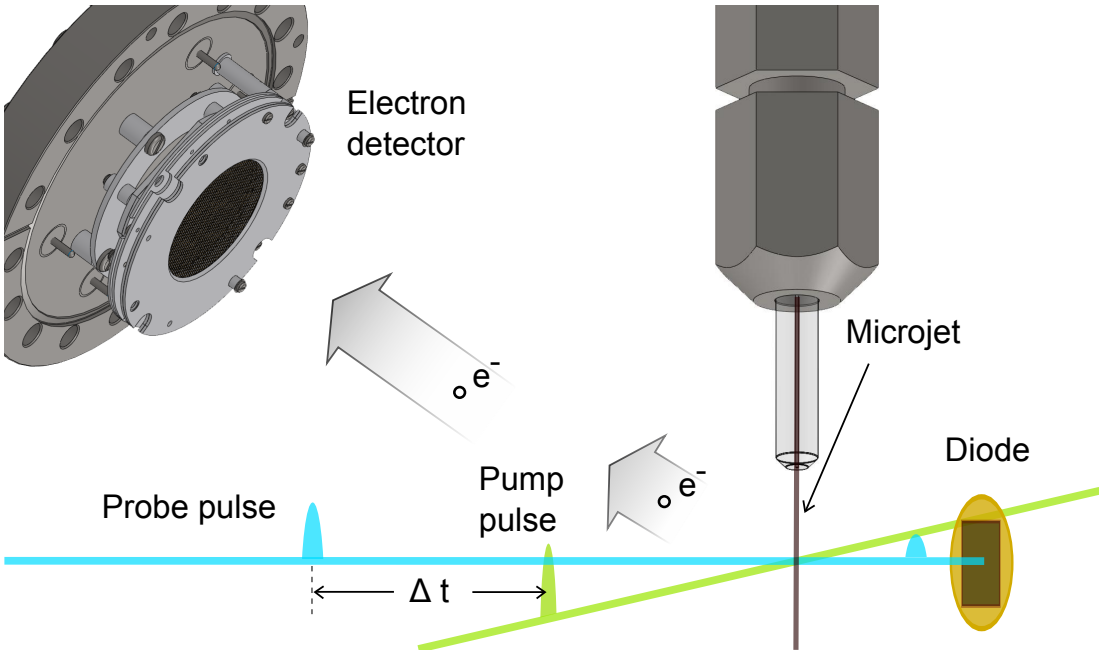

Figure 10: Illustration of the pump-probe scheme: A pump pulse and a probe pulse, delayed by Δt, interact with the sample (microjet) at the same spot. A diode can detect the difference in the absorption of the probe pulses between the pumped and unpumed system (TR-TA). The probe beam can also ionize the sample and the emitted electrons can be detected, while also measuring their kinetic energy. A possible difference in the resulting spectra for the pumped and the unpumped system can therefore reveal information about the excited system (TR-PES).

if the population decays exponentially. Here, N_0 is the population of the excited state at t_0 and τ represents its decay time.

Another probing technique to measure the properties of the excited states is the observation of signals, which occur only after excitation. For example, an excited state can show probe-induced fluorescence at different wavelengths than the ground state. Since fluorescence due to atomic core or inner shell excitation usually occurs on a sub-picosecond timescale, it is feaseble to conduct pump-probe experiments in fluorescence yield using soft X-rays at synchrotrons. Here, the attenuation length of the necessary photon energy is on the micrometer scale, making it impossible to measure absorption in transmission of thicker samples.

In this thesis, the sample is probed by PE spectroscopy. The emitted electrons of the probe pulses are detected at a certain distance away from the sample as illustrated in Figure 10. By measuring their Time-Of-Flight (TOF) spectrum,

we can determine their kinetic energies. As discussed in section 3.1.1, PE spectroscopy gives direct information about the BE of a given state. The difference in the spectra between the excited and the ground state PE spectrum is the transient spectrum, that can be interpreted analogously to normal PE spectra. This spectroscopic method is called Time-Resolved PE Spectroscopy (TR-PES). In the scheme of pump-probe experiments with a femtosecond resolution, the process of photo emission can be viewed as instantaneous. Recent experiments showed a delay of ~ 20 as in the emission of the electron wave package from the 2p state of Neon and the 3p state of Argon compared to their 2s and 3s states [115, 116, 117].

4 Experimental setup

In this chapter I will present the vacuum chambers and the equipment I designed and worked with during my PhD. Figure 11 shows a sketch of the setup used for UV-vis pump - XUV-vis probe experiments on liquids. Among others it consists of an interaction chamber, a detector unit and a revocery element to collect and reuse the liquid samples. In the following sections I will describe this setup in more detail. At the end I will also give a brief overview of our laser system.

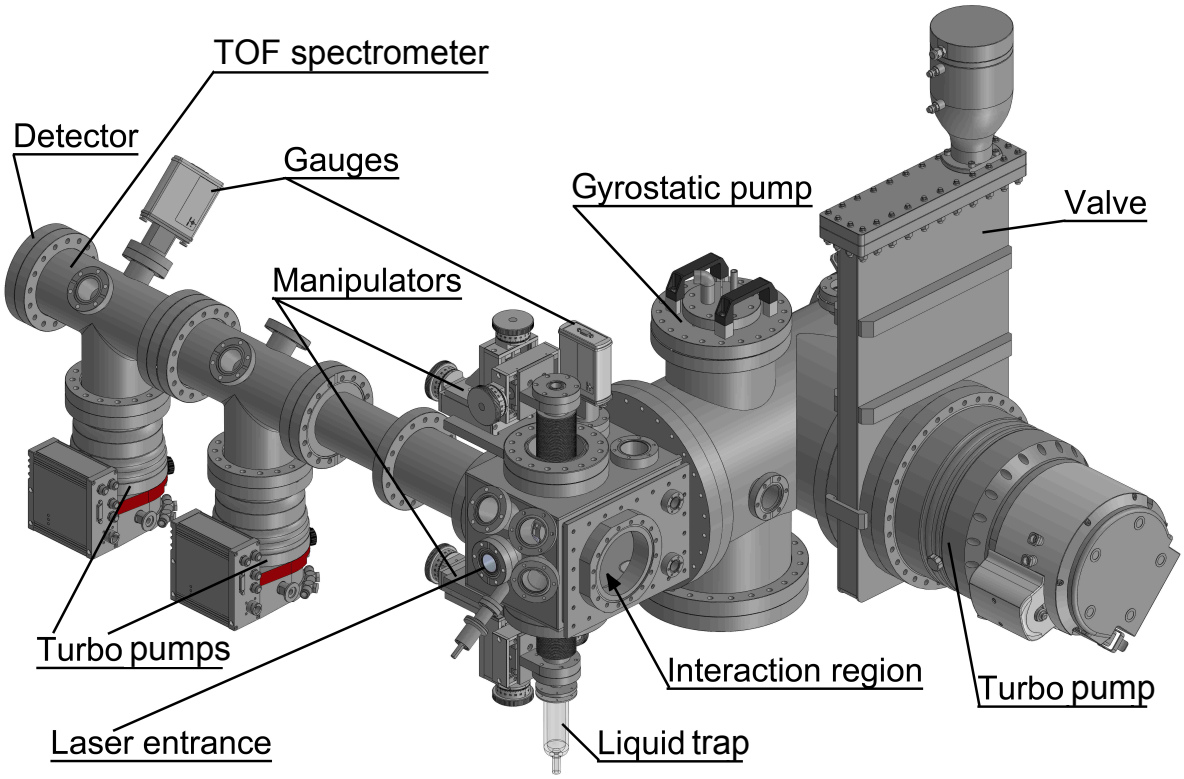

Figure 11: Overview of the experimental chamber and the electron TOF spectrometer. A detailed description is given in the text.

4.1 Recovering of liquid samples

This section is reproduced from [K. M. Lange, A. Kothe and E. F. Aziz, Phys. Chem. Chem. Phys., 14, 5331-5338 (2012)] - Reproduced by permission of the PCCP Owner Societies.

Measurements investigating ultrafast dynamics of liquids and diluted systems need stable conditions over many hours to obtain a good signal-to-noise ratio. The low concentration of the species of interest in diluted systems reduces the signal in comparison to the background originating from the solvent. Additionally, the excitation of only a fraction of this species into the excited state reduces the ratio between the desired transient signal and ground state and background further. Here, I will describe how to improve this technique to measure in principle continuously. Since this improvement was originally developed for laser pump - soft X-ray probe experiments on diluted systems, its necessity, performance and advantages are discussed in that context.

Until today spectroscopic measurements on liquids using the microjet technique that require vacuum conditions freeze the liquid downstream the jet in a liquid nitrogen cooled container. Typically, a pressure of at least 10^{-4} mbar in the vacuum chamber must be maintained in those experiments. Even though this method has proven to fulfill the required vacuum conditions, one needs to interupt the measurement to vent the system regularly to remove the frozen sample and to clean the chamber. For pump - probe experiments, which are highly sensitive to precise spatial alignment between the light pulses and the microjet, this procedure is not feasible. These experiments require measurements of several hours or even days to obtain a significant signal-to-noise ratio.

Previous long-term laser pump - XAS probe experiments on oxygen K-edge of liquid water upon infrared laser pump [119, 120, 121] and transient X-ray absorption studies on the L-edge of the transition metal complex $[Fe(tren(py)_3)]^{2+}$ dissolved in acetonitrile [122, 123] were performed using a flow-cell type of measurements. Here, the samples were prepared as a drop between two Si_3N_4 membranes, and the X-ray absorption was measured in transmission mode. However, while this approach of introducing solution to HV conditions is working in the above mentioned cases, it would not be suitable for many biochemical systems. In such systems the required high-intensity X-ray and laser irradiation can cause sample damage due to photochemistry or heating. Figure 12(a) illustrates our new recycle sample delivery system. This method is membrane-free and allows in

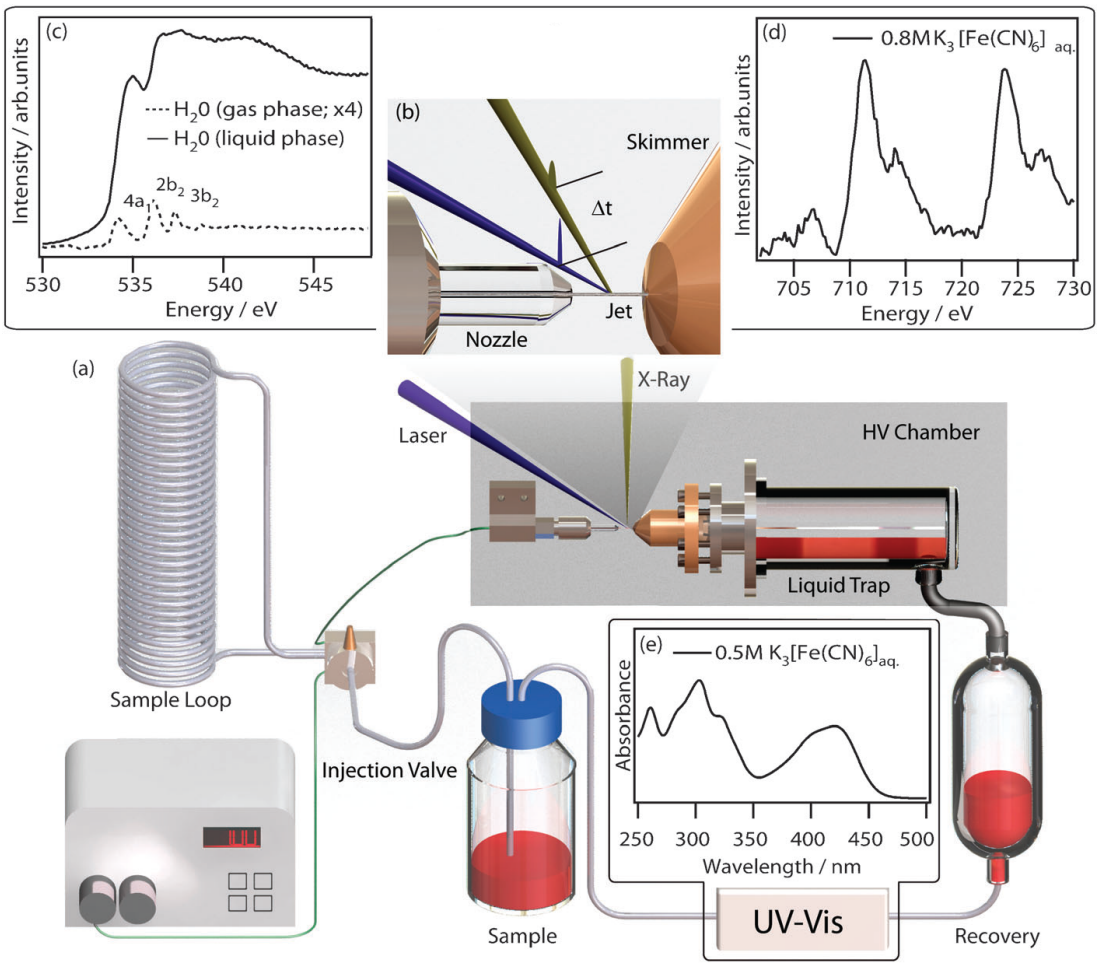

Figure 12: (a) Schematic of the recycle microjet technique for pump - probe measurements. See text for detailed description. (b) Enlargement of the overlap area of the microjet, pump- and probe beam. (c) XA spectrum of the oxygen K-edge of gas phase water and liquid water. (d) XA spectrum of the iron L_3-edge of $K_3[Fe(CN)_6]_{aq.}$. (e) UV-Vis spectrum of $K_3[Fe(CN)_6]_{aq.}$. From [118].

principle continuous laser pump and soft XAS probe measurements in the fluorescence yield (FY) mode to investigate ionic and molecular systems in solution. An enlarged detail for the laminar part of the jet is presented in Fig. 12(b). This novel installation permits the collection of the liquid sample from the microjet and its recovery from the chamber without interrupting the measurements. Usually, the installation is operating by pumping 120 ml of a filtered sample solution with an HPLC pump from a sample storage loop through a microjet nozzle of approximately 25 μm diameter. This nozzle is attached to a holder mounted on a xyz-motorized stage. The liquid jet travels ca. 4 mm through the HV chamber before it enters the liquid trap through a 150 μm pinhole of a temperature controlled copper catcher. This catcher is thermally decoupled by ceramics and by a knife-edge to the liquid trap side. This permits heating of the skimmer during alignment to avoid adhesion of the solvent on the pinhole. Depending on the temperature, the pressure in the liquid-trap is between 10 and 15 mbar for aqueous solutions and for acetonitrile approx. 50 mbar.

The trap is connected to the recovery outside of the chamber through a tube with a valve. To retrieve the sample, the recovery is pumped to a pressure of less than the pressure in the liquid trap. After venting, the sample can be taken out and measured in an UV-Vis or IR spectrometer to compare with a fresh sample. If no radiation damage occured, the sample can be loaded to the storage loop again for further measurements. Fig.12(c) shows the XA-FY spectrum of the oxygen K-edge of liquid water (saturated spectrum), obtained from the microjet, and in comparison with a gas phase spectrum obtained by shifting the jet 100 mm from the focus of alignment. Both spectra are in good agreement with former results. Evidently, this result demonstrates the efficiency of our newly designed recycle liquid trap for maintaining good vacuum conditions and ensures measuring the liquid micro-jet with negligible gas phase background. Fig. 12(d) shows the L3-edge XA spectrum of iron obtained from 800 mM $K_3[Fe(CN)_6]_{aq.}$ The spectrum shows a multiplet feature corresponding to the low-spin configuration, where the 5 electrons in the d-MOs are in the t_2g states built in an O_h crystal field of 4.6 eV with 6 CN ligands around the Fe(III) center. The low spin configuration of this complex in its solid state has been shown. Interestingly, the complex in solution also prefers the low-spin configuration. Note that, the in situ optical absorption spectrum of this complex is shown in Fig. 12(e). Originally experiments on different complexes should be performed using a pump-probe scheme similar to the one presented in reference [124]. The plan was to investigate the molecular structure and the nature of chemical bonds of the active centers of proteins with different ligands (e.g. O_2, CO, ...).

With the above described technique high vacuum conditions can be achieved in the sample chamber. After aligning the jet to the catcher a turbo molecular pump (Pfeiffer, HiPace 2300) with a pumping speed of 2300 l/s is used to reach a pressure of 10^{-3} mbar. In operation, a cyrostatic pump filled with liquid nitrogen further reduces the pressure to the range of 10^{-5} mbar through the adhesion of the evaporated water molecules from the jet onto its surface.

4.2 The electron time-of-flight spectrometer

This section is in part reprinted with permission from [A. Kothe, J. Metje, M. Wilke, A. Moguilevski, N. Engel, R. Al-Obaidi, C. Richter, R. Golnak, I. Yu. Kiyan and E. F. Aziz., Time-of-flight electron spectrometer for a broad range of kinetic energies, Rev. Sci. Instrum., 84:023106, 2013], Copyright [2013], AIP Publishing LLC.

4.2.1 Design of the spectrometer

For our experiments on liquids and functional materials in solutions we designed and built an electron TOF spectrometer to detect photo-excited liquid samples probed by photons in the eXtreme UV (XUV) and soft X-rays energy range. It allows to probe the electronic structure of valence and inner shells of compound molecules. In addition, we used multi-photon excitation in the UV range to demonstrate the feasibility of pump - probe measurements on the liquid microjet using this spectrometer. The results of these measurements are discussed in chapter 5. It was also employed to investigate the process of electron emission from solute targets exposed to a strong infrared laser pulse with a peak intensity of up to 10^{16} W/cm^2 [125].

Since aqueous solutions or functional materials in solutions are typically rather diluted samples, the detection of a solutes signal against the strong solvent background requires a large collection efficiency. Therefore we use additional magnetic fields to form a magnetic bottle to collect PE emitted over 2π steradians into a beam of a half angle 2°. This design was first developed and implemented by P. Kruit and F. H. Read [126].

An illustration of the magnetic field is illustrated in Figure 13. It consists of a strong inhomogeneous magnetic field from a permanent magnet (1 T) near the sample position, and a weaker homogeneous magnetic field (∼1 mT) generated by a coil around the TOF tube. From the sample, which acts in a good approx-

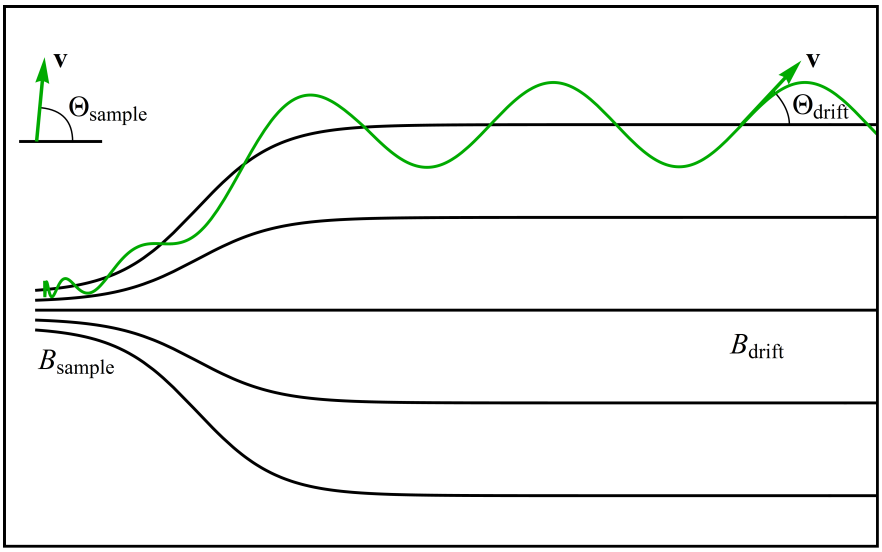

Figure 13: Two dimensional cut of the magnetic field used in magnetic bottle type TOF spectrometers. The projection of a possible electron trajectory onto the plane and the changes of its propagation vector $\mathbf{v}$ is depicted by the green line.

imation as a point-source, PEs are emitted in all directions. The Lorentz force causes the electrons to move on helical trajectories, whose slopes increase with decreasing magnetic field strength. Thus, the propagation vectors of the PEs are parallelized, while conserving their kinetic energy. The angle Θ_{sample} between the propagation vector of the PE just after emission and the symmetry axis of the magnetic field is related to the angle Θ_{drift} between the propagation vector of the electron and the symmetry axis in the region of constant magnetic field in the drift tube by

$$\frac{\sin\Theta_{\text{drift}}}{\sin\Theta_{\text{sample}}} = \sqrt{\frac{B_{\text{drift}}}{B_{\text{sample}}}} \tag{24}$$

with the magnetic field strength B_{sample} and B_{drift} at the sample and the detector position, respectively [126]. Considering the above mentioned values for B_{sample} and B_{drift} emission in the half-sphere from 0° to 90^o gives a maximum angle of $\Theta_{\text{drift}} \leq 1.8°$.

Since the time-of-flight (TOF) of the PEs in direction towards the detector depends greatly on the angle Θ_{sample} near the sample, the area of the strong inhomogeneous magnetic field is kept short compared to the region of constant magnetic field. In the region of a constant magnetic field strength the TOF t_{TOF} is given

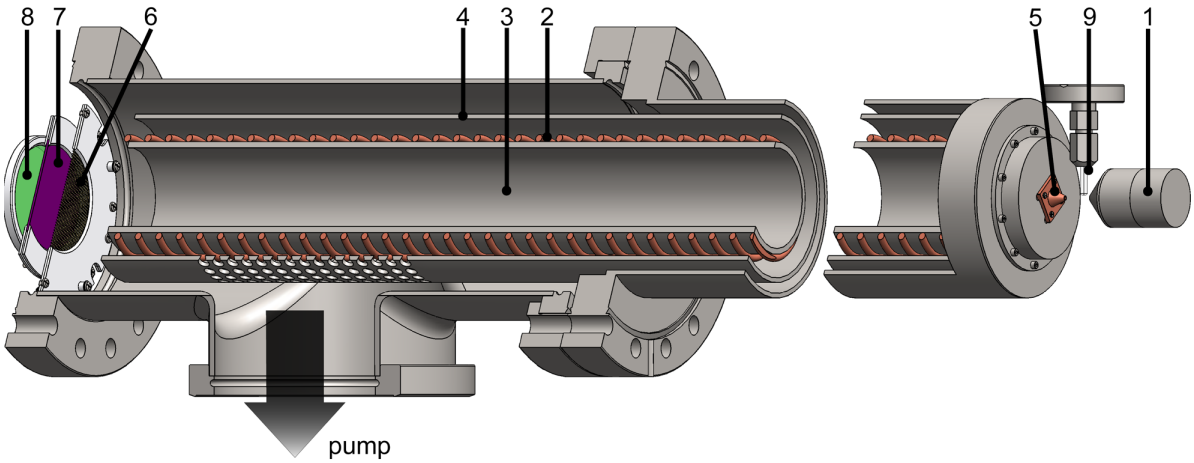

Figure 14: Illustration of the design of the TOF electron spectrometer: (1) permanent magnet with a soft iron cone, (2) solenoid, (3) drift tube, (4) μ-metal shield, (5) skimmer of 500 μm size, (6) copper mesh, (7) double-stack of MCP, (8) fluorescence screen, (9) nozzle to introduce the sample. From [127].

by

$$t_{\mathrm{TOF}} = \frac{l_{\mathrm{TOF}}}{v_{\mathrm{long}}} \approx \frac{l_{\mathrm{TOF}}}{v}\left(1 + \frac{B_{\mathrm{drift}}\sin^2\Theta_{\mathrm{sample}}}{2B_{\mathrm{sample}}}\right) \quad , \tag{25}$$

where l_{TOF} is the distance between the sample and the detector, $\mathbf{v}$ is the total velocity and v_{long} is the velocity parallel to the axis of symmetry, respectively. This is almost independent of Θ_{sample} [126]. Thus, the reduction in energy resolution of a magnetic-bottle TOF spectrometer is minor compared to a field-free TOF spectrometer. In the framework of liquid spectroscopy, where the states exhibit significantly broader energy-distributions compared to gas or solids, this disadvantage becomes even less relevant, while the significant increase in collection efficiency makes it possible to perform measurements on diluted systems in an acceptable time.

The spectrometer design is illustrated schematically in Figure 14. The magnetic bottle effect is generated by a strong inhomogeneous magnetic field B_{sample} of 1 Tesla created by a permanent magnet (1) and a weak homogeneous magnetic field B_{drift} of $\sim$1 mT generated by a coil around the TOF drift tube (2). The permanent magnet consists of two Sm_2Co_{17} pellet-shaped cylinders with a diameter of 25 mm and a length of 15 mm each (IBS Magnet, DE2515). A soft iron cone with a 42° angle at its base and a tip size of 3 mm diameter increases the field strength further in the interaction region located close to the tip. The coil is

made of a Kapton-isolated copper wire of 0.8 mm thickness, wrapped around the non-magnetizable stainless steel tube (3) with 500 turns per meter. The drift tube has a length of 97 cm and is perforated with holes of 2 mm diameter for pumping purposes (not shown in the Figure). A typical coil current of 2 A, generating a magnetic field $B_{\text{drift}} \simeq 1.26$ mT inside the drift tube, was used during the tests of the spectrometer. In the measurements conducted in the laser pump - laser probe scheme on aqueous sodium iodide (see chapter 5) we used a coil current of 1 A. This value gives the smallest FWHM of the contributions in the PE signal from Argon gas. The 2 mm thick μ-metal shield (4) around the solenoid prevents penetration of external magnetic fields into the drift region and, thus, preserves homogeneity of the B_{drift} field and its direction parallel to the spectrometer axis. In order to facilitate pumping of the TOF region, the μ-metal cylinder is also perforated with holes of 5 mm diameter in the area facing the turbo-pumps. The skimmer (5) of 500μm size defines the entrance for electrons into the spectrometer. The distance between the skimmer and the magnet tip was 2 mm in the characterization measurements.

We use double-stacked micro-channel plates (MCPs) (TOPAG, MCP50-10-4) (7) and a fluorescence screen (ProxiVision) (8) mounted behind them to detect electrons passing through the drift tube. A copper mesh (6) of 88 % transmission[4] in front of the MCPs is used to accelerate electrons before they hit the detector. The mesh is grounded to the drift tube, while an acceleration voltage of +300 V is applied to the front surface of the MCPs. This ensures efficient detection of electrons generated with low kinetic energies. According to the MCPs' characteristics, the gain is nearly constant for electron detection in the energy range from 300 to 1000 V. A voltage of 1500 V is applied across the MCP stack to amplify the electron signal. Amplified electrons are accelerated to the fluorescence screen by applying a potential difference of 3000 V between the back MCP surface and the conductive layer of the screen. While fluorescence light, recorded by a CCD (Charge-Coupled Device) camera, is used to visualize the detected electrons for allignment purposes, the conductive layer serves as an anode that collects electrons and generates an electric pulse. The pulse signal is decoupled from the high potential of the screen by a capacitor. After amplification, the pulse width generated by a single electron event is in the order of 2 ns. The signal is recorded by a time-to-digital converter card (RoentDek, fADC4) with a bin width of 200 ps. This card is triggered by a signal coinciding with the light pulses generating the PE. For the characterization experiments this signal is the

[4] 88 % transmission refers to the area without material of the mesh. Transmission for electrons will differ from this value and also depend on the kinetic energy of the electrons. Slow electrons will hit the mesh with a higher probability due to their mirror-charge.

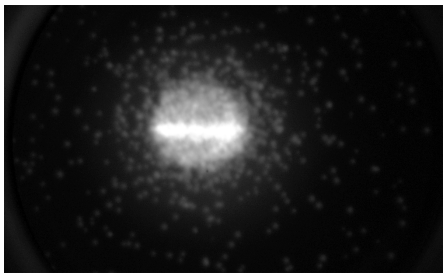

Figure 15: Image of the fluorescence screen recorded with an exposure time of 100 ms of the CCD camera at a count rate of approximately 20000 events per second. From [127].

1.25 MHz single-bunch clock, while in the laboratory JULiq the signal controlling the Pockels Cells of the regenerative amplifier of the laser system (5 kHz) is used as trigger. The data acquisition program offers two measurement options. In event-counting mode, the time between the trigger and the electric pulses from the fluorescence screen is recorded and displayed in a histogram. This mode requires a clear seperation of the electric pulses. In integration mode the complete oscilloscope traces of the electric signal from the fluorescence screen are recorded between two trigger signals and added. Here the amount of electrons detected per pulse can be higher since the signal strength of overlapping electric pulses will be reflected in the spectrum. Usually, we reduce the laser intensity to several nJ in order to have only 15-20 ionization events per laser shot. Background/dark noise produces around 0.2 events per shot.

4.2.2 Characteristics of the spectrometer

Calibration procedure

Calibration and characterization of the spectrometer were performed at the undulator beamline U41-PGM of BESSY II light source at HZB in single-bunch operation mode. The beamline provides horizontally polarized light pulses with a pulse length not longer than 100 ps at a repetition rate of 1.25 MHz. The photon energy can be adjusted in the range from 180 to 1700 eV. The spectrometer was attached to the experimental chamber "LIQUIDROM" in the horizontal plane so that its axis was collinear to the polarization of the X-rays. The beamline electronics provide trigger pulses at the synchrotron repetition rate, which were used to trigger the converter card. A typical acquisition time of a TOF spectrum accounted two minutes at a sampling rate of up to 40000 events per second.

Argon was used as a sample due to its known electronic structure and ionization

cross sections[128]. The gas was fed into the experimental chamber using the microjet setup and entered the interaction region through the glass nozzle (9) mounted in the vicinity of the skimmer (see Fig. 14). The gas flow was controlled by a dosing valve. A typical pressure of 2×10^{-4} mbar was maintained during the experiment. Small variations in the pressure of less than 2 % over hours ensured basically constant Ar density in the interaction region. Using a skimmer with a 500μm aperture, a pressure of 3×10^{-8} mbar in the TOF region was achieved.

An image of the fluorescence screen recorded by the CCD camera with an exposure time of 100 ms is presented in Fig.15. The image shows a magnified filament of PEs created by the X-ray beam along its propagation direction which is confined by the skimmer aperture. The filament exhibits a thickness of approximately 1 mm on the fluorescence screen, corresponding to a magnification factor $M \simeq 20$ for the 50μm beam size in vertical direction. Using the relation $M = (B_{sample}/B_{drift})^{1/2}$ given in reference [126] and taking the value $B_{drift} = 1.26$ mT into account, the magnetic field in the interaction region is estimated to be $B_{sample} =\sim 500$ mT.

The spectrometer calibration was performed by measuring the arrival time of PEs ionized from the $2p$ core-orbital of Argon. This ionization channel has the largest cross section in the photon energy range considered in this work [86]. The $2p$ orbital possesses a spin-orbit structure. The ionization potentials related to the $2p_{1/2}$ and $2p_{3/2}$ components of this structure are 250.8 and 248.6eV, respectively [85]. The high repetition rate of the X-ray pulses restrict the calibration energy range to 4.9 eV and higher. This is because electrons with lower kinetic energies do not arrive at the detector within the time interval of 800 ns between two X-ray pulses, while the converter card already receives the next trigger pulse. Therefore, the lowest photon energy used for calibration was 255.5 eV, which ensured that electrons ionized from both the $2p_{1/2}$ and $2p_{3/2}$ orbitals arrive at the detector within 800 ns after the ionization event.

The calibration data recorded in the photon energy range from 255.5 to 1000 eV are presented in Figure 16. The TOF spectra are vertically shifted in the figure, whereas the shift of a given trace is proportional to the photon energy used to record the spectrum. The photon energy scale is given by the vertical axis on the right-hand side of the figure, respectively. This facilitates observing the arrival time of electrons, manifested by peaks in the spectra, as a function of the excitation energy. Apart from the peaks associated with ionization of the $2p$ states, the spectra reveal contributions from ionization of the $2s$ and $3s$ shells, as well as from Auger LMM decays of the $2p$ hole. The Auger spectrum is in good agreement with the results presented in reference [129]. The relation between

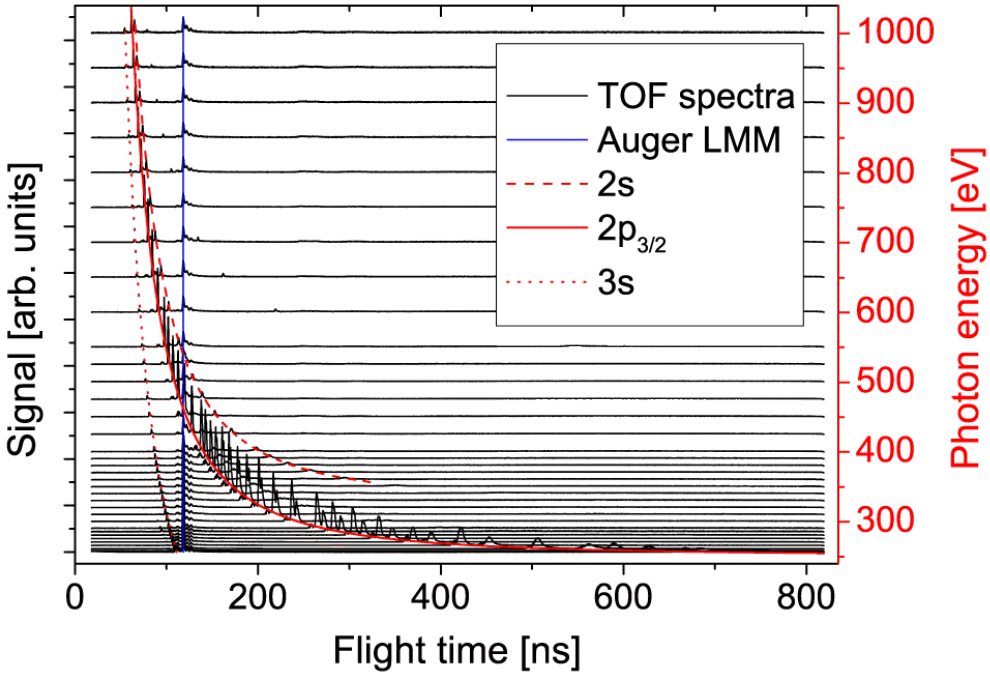

Figure 16: TOF spectra of Ar (black lines) shifted vertically according to the photon energy (right scale). The Auger LMM peaks are depicted by the vertical blue line. The red curves represent the calibration functions (26) for ionization of the Ar $2s$ (dashed line), $2p_{3/2}$ (solid line) and $3s$ (dotted line) shells. From [127].

the electron kinetic energy E_{kin} and the arrival time t measured by the converter card is given by

$$E_{\mathrm{kin}} = \frac{m_{\mathrm{e}}}{2} \frac{L^2}{(t - t_0)^2} \quad , \tag{26}$$

where m_{e} is the electron mass, L is the path length of electrons from the X-ray focus to the detector, and t_0 accounts for the time offset of the trigger. For a given ionization channel, the kinetic energy is calculated as $E_{\mathrm{kin}} = E_{\mathrm{ph}} - E_{\mathrm{IP}}$, where E_{ph} is the photon energy value provided by the beamline, and E_{IP} is the ionization potential of the initial state. The sequences of the peaks in the TOF spectra associated with ionization of the $2p_{1/2}$ and $2p_{3/2}$ states were fitted to Eq. (26) with the fit parameters L and t_0. The values of their ionization potentials were taken from reference [85]. The fit result for the $2p_{3/2}$ state is shown in Figure 16 by the red solid curve. The calibration procedure yielded the value $L = 102$

cm for the distance between the interaction region and the detector.

Performance characteristics

The energy resolution and the collection efficiency of PEs represent important characteristics of the spectrometer. Typically an increase of one of these parameters leads to a decrease of the other. It represents a challenging task to achieve high energy resolution simultaneously with high collection efficiency. In this section we consider the performance characteristics of the newly built magnetic-bottle TOF spectrometer. In the analysis we use the performance of the same instrument, but without magnetic bottle, as a reference. In the latter case the permanent magnet was disassembled and a μ-metal shield was mounted around the interaction region. The field-free spectrometer configuration represents the limiting case, where the electron collection is minimal and is solely defined by the cone that comprises straight electron trajectories from the interaction region to the detector. While using the spectrometer without magnetic bottle, a significant improvement in the signal-to-noise ratio was achieved by applying a coil current of the order of 1 A. The induced magnetic field prevented background electrons, originating from surfaces inside the drift tube or the hot cathode of the gauge, from reaching the detector. Though such an unusual field configuration resulted in a slight broadening of the TOF peaks, it had no effect the analysis of characteristics of the magnetic-bottle TOF spectrometer presented below.

Energy resolution

The TOF spectra shown in Figure 16 were transformed from time to energy scale, E, using equation (26) with $E = E_{\text{kin}}$ and L and t_0 obtained from the fit. The transformation factor $dE/dt \sim E^{3/2}$ was taken into account in these calculations.

The energy resolution, defined by the width of energy peaks, was obtained from Gaussian fits to the energy spectra. The two peaks arising from the Ar($2p$) fine structure are well separated in the spectra recorded at low excitation energies and could be fitted to single Gaussian profiles. The individual fits yielded comparable widths for the $2p_{1/2}$ and $2p_{3/2}$ peaks. With the increase of the excitation energy, the fine-structure peaks start overlapping each other. Therefore, at higher kinetic energies the peaks were fitted together to a sum of two Gaussian profiles with equal widths

$$y(E) = A_1 e^{-\left(\frac{E-E_0}{w}\right)^2} + A_2 e^{-\left(\frac{E-E_0-\Delta E_{\text{SO}}}{w}\right)^2} \quad , \tag{27}$$

where E_0 denotes the energy position of the $2p_{1/2}$ peak, $\Delta E_{\text{SO}} = 2.2$ eV is the energy of the fine structure splitting, w is the Gaussian width of peaks, while A_1 and A_2 are their amplitudes, respectively. These four parameters are the fit

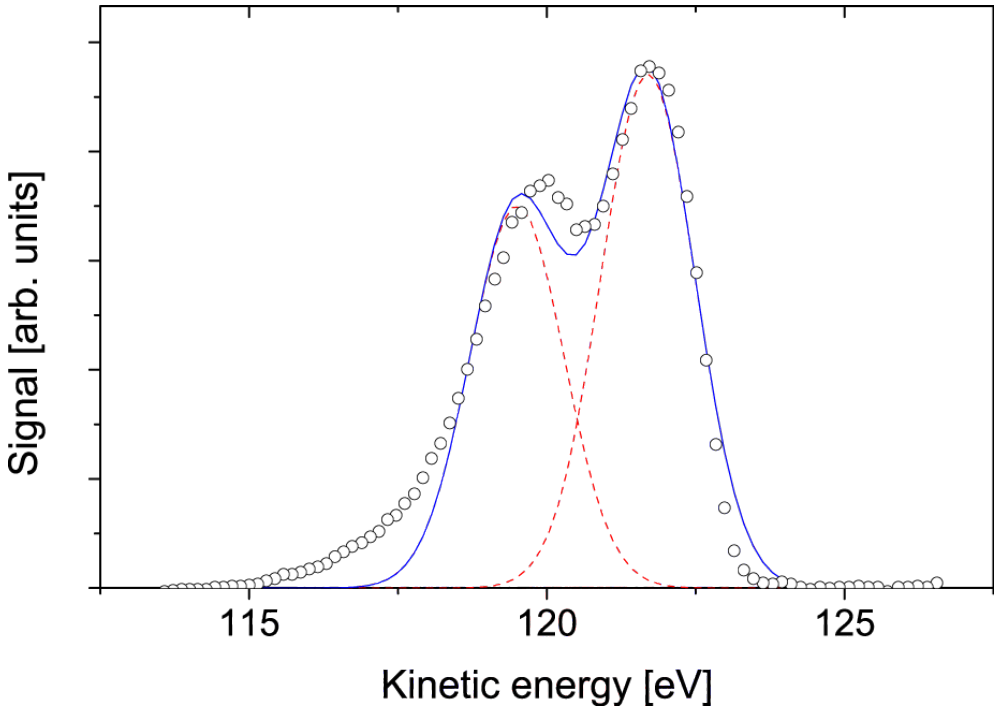

Figure 17: Energy peaks of the Ar $2p_{1/2}$ and $2p_{3/2}$ electrons generated at a kinetic energy of $\sim$ 120 eV. Solid line represents the fit of Eq. (27) to the experimental spectrum. The individual peak contributions are shown by dashed lines. From [127].

parameters in the calculations. The Gaussian width w is transformed to a full width at half maximum (FWHM). As an illustration, Figure 17 shows the results of the fit to a spectrum for which electrons are generated with kinetic energies of approximately 120 eV. In this spectrum the fine structure splitting is still resolved. At kinetic energies higher than 250 eV the $2p_{1/2}$ and $2p_{3/2}$ peaks merge and are not distinguishable.

PE peaks in the energy spectra are asymmetric, with a steeper slope at the high-energy flank. The peak asymmetry is discussed in detail in reference [126]. It was shown that a slight displacement of the source of monoenergetic electrons from the magnetic-bottles axis of symmetry can result in an essential asymmetric broadening of the energy peak, as well as in a change of its position on the energy scale (see Figure 13 in Ref.[126]). Here, the electron source represents a filament, limited by the skimmer aperture of 500μm (see Figure 15), and, therefore, the peak asymmetry is unavoidable. Nevertheless, the fit of Gaussian functions to asymmetric peaks yielded FWHM values which are in good agreement with values obtained from a manual estimation of widths.

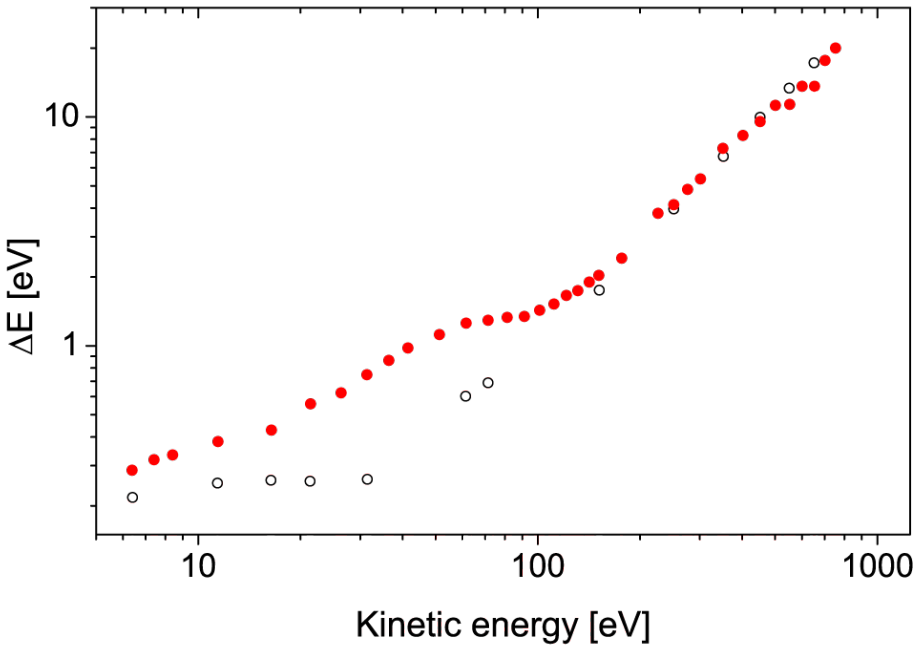

Figure 18: Energy resolution obtained for the magnetic-bottle (closed circles) and the field-free (open circles) spectrometer configurations. From [127].

Figure 18 shows the energy resolution obtained for both the magnetic-bottle and the field-free spectrometer configurations in the range from 5 to 750 eV. The two curves are displayed on a double logarithmic scale for better visualization of the low energy region. In this region the resolution of the field-free spectrometer is limited due to the coil current used to reduce the background signal. One can see that the resolution obtained with the magnetic-bottle configuration is generally worse at lower kinetic energies. This is due to the collection mechanism leading to a spread in the path length of helical trajectories.

The resolution curve obtained for the magnetic-bottle configuration exhibits a short plateau at kinetic energies higher than 50 eV, where the relative resolution $\Delta E/E$ improves. In this region we observe losses in the collection of photoelectrons. With the increase in kinetic energy, electrons emitted at a given angle with respect to the spectrometer axis of symmetry are captured by the magnetic field at a larger distance from this axis. Thus, the electron trajectories become less localized and can be screened by the skimmer. This results in a decrease of the acceptance angle and, simultaneously, in an improvement of the relative energy resolution, which reaches a value of 1.6 % at the kinetic energy of 100 eV. This value is comparable to that of a TOF spectrometer reported in reference [129].

At higher kinetic energies, the collection mechanism becomes even less efficient and the resolution of the magnetic-bottle spectrometer approaches the resolution of the field-free spectrometer. Figure 18 shows that at energies higher than 200 eV the resolution curves are basically identical. In this range the finite response time of 2 ns of the detection setup to a single event represents the limiting factor for both the field-free and the magnetic-bottle spectrometer configurations. Due to this limitation, $\Delta E/E$ gradually changes from 2 to 2.8 % in the range from 300 to 750 eV.

Collection efficiency and acceptance angle

The collection efficiency T is defined by the ratio of the number of detected electrons, S, to the number of electrons generated in the ionization process, Y. Using the electron yield in the $2p$ ionization channel, this quantity is calculated as:

$$T = \frac{S_{2\mathrm{p}}}{Y_{2\mathrm{p}}} \ , \tag{28}$$

where $S_{2\mathrm{p}}$ represents the integrated signal of the $2p_{1/2}$ and $2p_{3/2}$ peaks in the energy spectrum, and the ionization yield is given by

$$Y_{2\mathrm{p}} = \rho_{\mathrm{Ar}}\, \Phi\, \tau\, \sigma_{2\mathrm{p}}\, D \ . \tag{29}$$

Here ρ_{Ar} is the Ar density, Φ is the flux of X-ray radiation, τ is the acquisition time, $\sigma_{2\mathrm{p}}$ is the partial ionization cross section of the 2p shell, and D is the accepted length of the interaction region along the X-ray beam.

In our analysis we use the fact that the signal in the LMM Auger peaks S_{A}, arising in the spectra at kinetic energies between 190 and 220 eV, is proportional to the ionization yield $Y_{2\mathrm{p}}$. [129] The kinetic energy of the Auger electrons is independent of the excitation energy and, therefore, their collection efficiency remains unchanged for different photon energies. Hence, by normalizing the $S_{2\mathrm{p}}$ signal to the Auger signal S_{A} recorded in the same spectrum, we obtain the functional dependency of the collection efficiency T on the kinetic energy, though its absolute scale remains undefined.

The absolute value of T can be easily calculated for the field-free configuration since in this case the acceptance angle $\theta_{\mathrm{max}}^{\mathrm{FF}}$ is unambiguously defined by the geometry of the spectrometer. In the present setup $\theta_{\mathrm{max}}^{\mathrm{FF}} \simeq 1.1^{o}$, determined by the MCP aperture of 40 mm and the distance of 102 cm from the interaction region to the MCP. The absolute value of collection efficiency was obtained by evaluating the integral

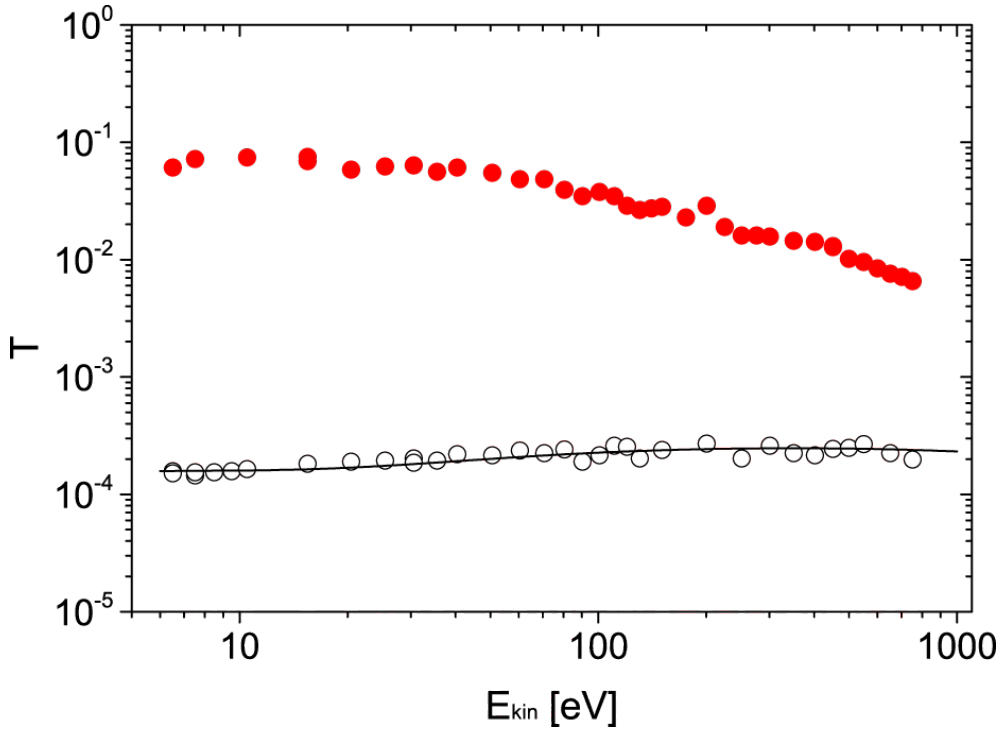

Figure 19: Collection efficiency of the $2p$ electrons obtained for the magnetic-bottle (red filled circles) and the field-free (black open circles) spectrometer configurations. The solid line represents calculated results for 1.1° acceptance angle by using Eq. (30). From [127].

$$T = \int_{\Omega} \frac{1 + \beta P_2(\cos(\theta))}{4\pi} \, \mathrm{d}\Omega \; . \tag{30}$$

The integrand represents the angular distribution of photoelectrons, expressed in terms of the asymmetry parameter β and the Legendre polynomial $P_2(\cos(\theta))$, and θ denotes the emission angle with respect to the X-ray polarization axis.[130] Since the X-rays are polarized colinear to the spectrometer axis, the integration is carried out over a solid angle Ω limited by a cone with $0 < \theta < \theta_{\mathrm{max}}^{\mathrm{FF}}$ and $0 < \phi < 2\pi$. The β parameters for ionization of the $2p$ shell of Ar were taken from Ref.[86] The results of these calculations are presented by a solid line in Figure 19. The energy dependency of T, derived from the experimental data as the ratio $S_{2\mathrm{p}}/S_{\mathrm{A}}$, was multiplied by a constant to obtain the best fit to the calculated value of T in the considered energy range. The results of this normalization are shown in Figure 19 by open circles, and demonstrate an excellent agreement between the measured and the calculated energy dependencies of T obtained for the field-free

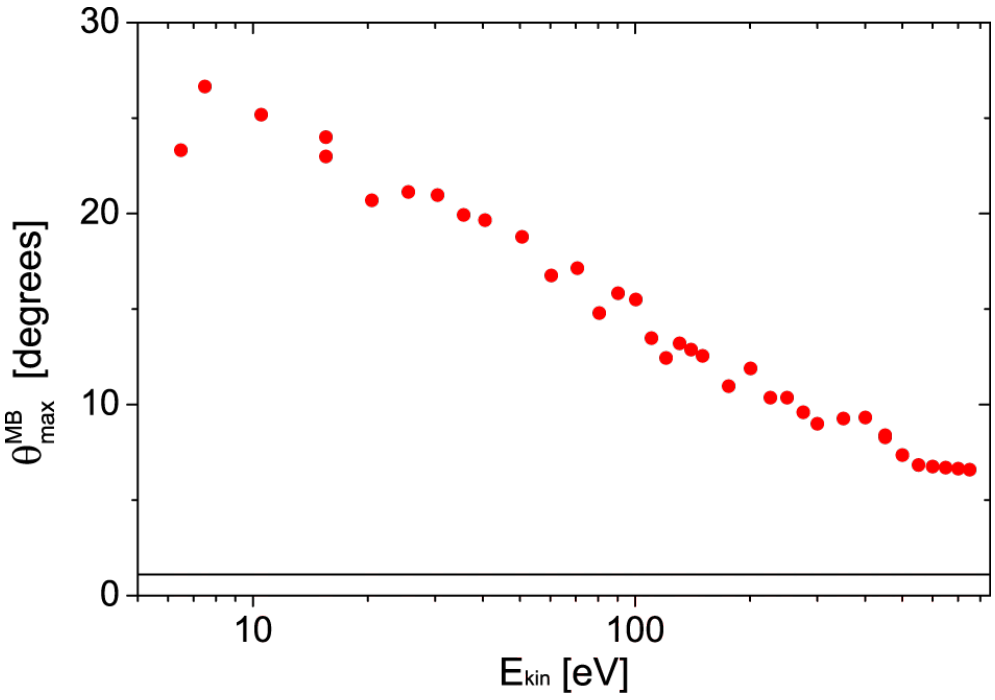

Figure 20: Dependency of the acceptance angle on the kinetic energies for the magnetic-bottle spectrometer configuration. The acceptance angle of 1.1° of the field-free spectrometer is depicted by a solid line. From [127].

spectrometer configuration.

In order to determine the absolute value of T for the magnetic-bottle configuration, we calculated the absolute ratio of collection efficiencies of the magnetic-bottle and the field-free spectrometer configurations at a fixed kinetic energy of 80 eV. In these calculations, recorded at the excitation energy of 330 eV, the S_{2p} signals were first normalized to the measured experimental parameters Φ, τ, and the gas pressure. The absolute ratio of efficiencies was obtained by dividing the normalized signals by each other. The energy dependency of S_{2p}/S_A, obtained for the magnetic-bottle configuration, was then multiplied by a constant in order to match the calculated ratio of efficiencies at $E_{kin} = 80$ eV. The obtained results are shown in Fig. 19 by filled circles. The presented results demonstrate that, with the use of the magnetic bottle, an enhancement by more than two orders of magnitude in the collection efficiency is achieved. This enhancement remains nearly constant up to kinetic energies of 50 eV. At higher energies the magnetic field is not strong enough to catch electrons emitted at larger angles, and the efficiency monotonically decreases by an order of magnitude with the increase of the kinetic energy to 750 eV.

The energy dependency of the acceptance angle for the magnetic-bottle spectrometer, $\theta_{\max}^{\mathrm{MB}}$, can be obtained by using Eq. (30) from the data shown in Figure 19. The results of these calculations are presented in Figure 20. The acceptance angle monotonically decreases with the increase of the kinetic energy, which results in the loss of photoelectrons, as discussed above. Its maximum value is 25° in the low energy limit which is substantially less than the angle of $\pi/2$ reached in other setups.[126, 131] This is due to the screening of electron trajectories by the small skimmer aperture in front of the drift region.

4.3 The laser system

The basis of the newly built HHG laboratory JULiq is a Ti:Sapphire laser system. It consists of a modelocked seed laser (Coherent; Vitara), which generates pulses with an energy of 7 nJ at a repetition rate of approximately 80 MHz. The central wavelength is 800 nm at a bandwidth which exceeds 125 nm. These pulses are coupled into a double stage amplifier (Coherent, Legend Elite) at a repetition rate of 5 kHz. The pulses first take several roundtrips in a regenarative amplifier before they are amplified in a two pass parametric amplifier. The emitted pulses exhibit a shortest pulselength of 22 fs. Their spectral bandwidth is specified by 77 nm FWHM at a central wavelength of 798 nm (center of gravity of the spectrum) at a pulse energy of 2.4μJ (total power 12 W). The beamprofil is Gaussian-shaped with a diameter of 12 mm in both, horizontal and vertical, directions. The polarization of the beam is horizontal.

A beamsplitter is used to obtain a beam with a power of 5 W which is introduced into an Optical Parametric Amplifier (OPA) (Light Convertion, OPerA-Solo). In the experiments demonstrated in chapter 5, the compression was set for optimum output power of the OPA at a wavelength of 350 nm, which was 20 mW. The reflected beam with a power of 7 W passes a delaystage (Newport, FMS300), which controls the time delay between both beams. The delaystage can be operated by the Data AQuisition (DAQ) program.

For the generation of the third harmonic, the beam is reduced to a diameter of 6 mm using a telescope. This beam passes a Beta-Bariumborat (β-BaB_2O_4 or BBO) crystal (EKSMA, BBO-601H) of 0.1 mm for second harmonic generation. A calcite plate accounts for the velocity mismatch of the second harmonic (400 nm) and the fundamental beam in the optical elements to overlap the pulses of both beams in time in another 0.1 mm thick BBO crystal (EKSMA, BBO-609H) for third harmonic generation. Before this crystal, a dual waveplate rotates the polarization of the fundamental beam by 90°, since the 400 nm beam exhibits

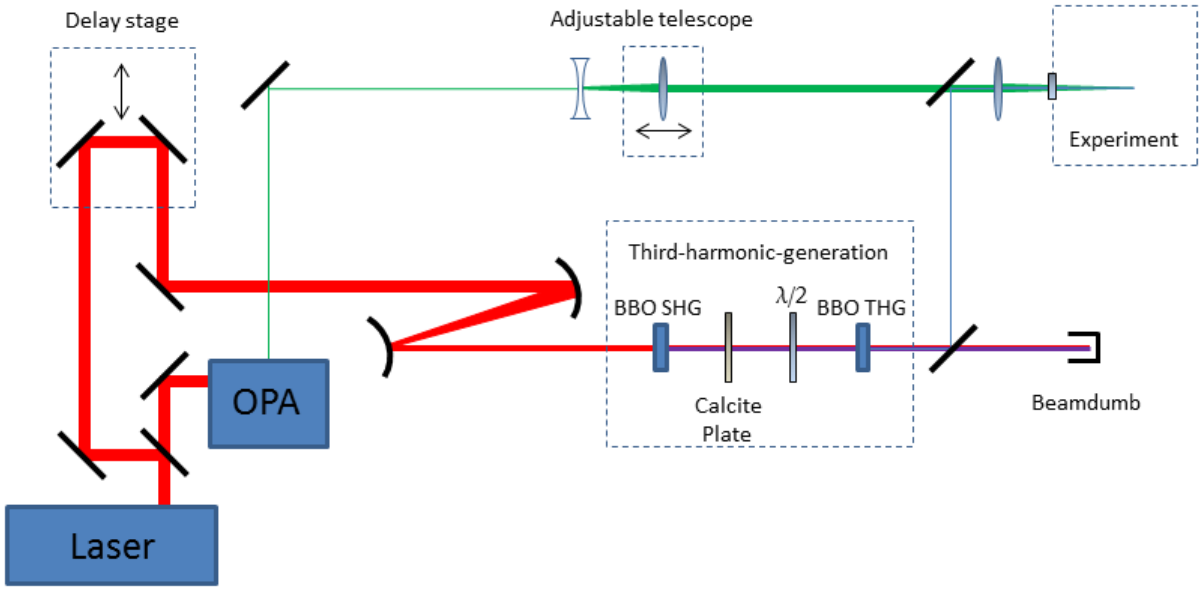

Figure 21: Optical setup used in the pump - probe experiments. Both laser beams 266 nm and 350 nm are focus 266 nm and 350 nm onto the jet in the experimental chamber. Further details are described in the text.

vertical polarization. The resulting beam is composed by three wavelength, 800 nm, 400 nm and 266 nm. A dichroic mirror reflects only the 266 nm beam with a power of 5 mW and horizontal polarization, while the other components pass through the mirror and enter a beam dump, where they are absorbed. Another dichroic mirror overlaps the 266 nm beam with the 350 nm beam. Before both beams enter the vacuum chamber through a 3 mm uncoated UV-fused silica window, a lens made of calcium fluorid focuses both beams to approximately 40 μm on the microjet. Reflective neutral density filters are used to attenuate each beam individually. Shutters can block each of both beams to switch between recording the spectra for PE emission from a single beam and the excited system, when both beams hit the microjet.

The pulse duration of both pulses is approximately 60 fs. This approximation is based on the pulse duration of 25 fs of the fundamental 800 nm beam, which is close the Fourier-transform limit, and the measured optical spectrum of both pulses shown in appendix 30, which gives a Fourier-transform limited pulse duration of 23.1 fs (350 nm probe pulse) and 47.7 fs (266 nm pump pulse) when considering a Gaussian shaped temporal envelopes. Additional broadening occurs due to the optics described above. These values represent the shortest pulse

possible for each beam.

5 Results and discussion

This chapter is reproduced in part from [A. Kothe, M. Wilke, A. Moguilevski, N. Engel, B Winter, I. Yu. Kiyan and E. F. Aziz, Phys. Chem. Chem. Phys. 17, 1918-1924 (2015)] - Reproduced by permission of the PCCP Owner Societies.

The results obtained in the pump - probe experiments from an aqueous NaI solution presented in this chapter represent the main part of this thesis. As opposed to previous studies here two-photon absorption leads to population of the CTTS-like state above the vacuum level, i. e., far above the energy of the lowest CTTS state. First, the preparation of the sample solution is described and experimental details are presented. The measured one-color spectra, which arise from a single pulse only, are discussed. The transient signal of the time-resolved PE measurements is discussed in the subsequent section. A model to describe the temporal evolution of transient PE spectra is developed and discussed. Based on this model, the assignment of the two observed spectral contributions to the CTTS and CTTS+1 state is justified.

5.1 Sample preparation and measurement scheme

The 20 mM NaI aqueous solution was prepared by adding sodium iodide to liquid water, which has been purified in a water purification system (Merck Millipore, Milli-Q). Filters with a pore size of 2 μm made from PEEK (polyether ether ketone) remove residual particles from the solution before it is forced through the nozzle to prevent blocking of its orifice. To avoid (sun)light-induced oxidation of iodide to iodine and the subsequent formation of triiodide (I_3^-), the solution was kept in dark bottles and the sample storage loops were shielded with aluminum foil.

The concentration of 20 mM used here is well within the range of 15 mM to 190 mM, where it has been shown, that the transient spectra of NaI aqueous solutions exhibit no change [71]. The one-color PE spectrum obtained with the 266 nm (4.65 eV) pulses reveals only negligible differences in shape for concentrations above 10 mM [69]. Both findings show that no concentration-dependent effects such as charging of the liquid affect our measurements.

The required transformation from the TOF scale to the scale of kinetic energy according to equation 26 is based on a different method compared to the procedure

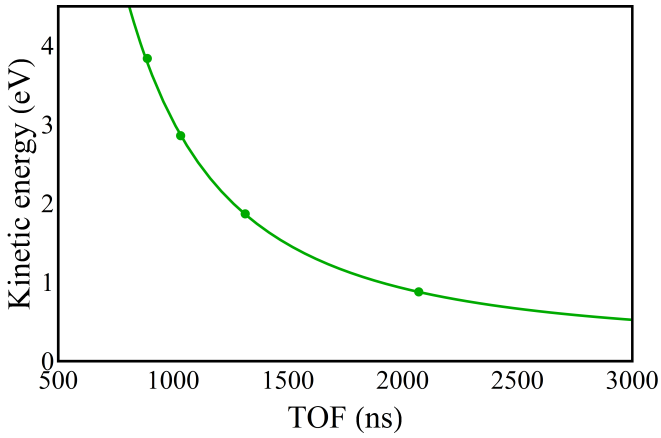

Figure 22: Transformation function from TOF to electron kinetic energy scale used in the experiment. The curve (green line) was obtained in experiments where a strong laser field ionized water vapor [125] and was shifted for a streaming potential of 0.2 eV. The green dots represent the measured points for this experiment on the liquid microjet.

used in the characterization of the spectrometer (see section 4.2.2). The ionization of low-density gaseous samples as described in section 4.2.2 is not convenient, due to too long measurement times for the pulse energies used in the experiment. Thus, the transformation parameters are obtained by changing the voltage at the MCP front from an accelerating +300 V to a decelerating voltage in the range from 1 to 4 V. Thus, all electrons are decelerated between the grounded copper grid and the MCP. This also means, that PEs below a certain minimal kinetic energy will not reach the detector, due to their reversed propagation direction before hitting the MCP. Thus, the recorded TOF-spectra exhibit a cut-off at a certain time, which can be assigned to the kinetic energy of the electrons just decelerated to zero at the MCP front.

The transformation function was obtained using the above described method by irradiating gaseous water using a strong laser field, which yields PEs with kinetic energies that range up to 500 eV [125]. The function can be utilized for the pump - probe experiments on the microjet, when taking into account the streaming potential as described in section 3.1.2. In the case of 20 mM aqueous sodium iodide solution the streaming potential is approximately -0.2 eV [63]. The resulting function is displayed in Figure 22 by the green line, which agrees well with the measured values (green dots) of the pump - probe experiments.

Since a measured pump - probe spectrum contains signal from the transient species as well as both one-color signals, the one-color spectra are substracted

from the corresponding pump - probe spectra to obtain solely the transient spectrum at a certain time delay. Before substraction, each spectrum is corrected for an equally distributed background.

For each measurement, the intensities of the pump and the probe pulses were attenuated to values, where one counting-event per pulse occurs on average at maximum PE yield. The pulses had an energy of 3 nJ for the pump and 200 nJ for the probe pulses, respectively. Taking into account the acceptance angle of the spectrometer in the range of kinetic energies of the PEs, an ionization rate of less than 15 electrons per pulse is estimated, which ensures negligible charging effects [14].

The spectra of the transient PE emission from the 20 mM NaI aqueous solution presented in section 5.3.1 were obtained using the experimental setup described in chapter 4. Three different PE spectra were recorded consecutively before changing the time delay between the pump- and the probe-pulses. These are the two one-color signals, which will be discussed in section 5.2, and the pump-probe spectra, which represents the case, when both pulses hit the sample. The PE spectrum measured with only the probe pulse represents the pure ground state spectrum. The PE spectrum originating from both beams can show additional features originating from the excited system.

The measurement duration of each type of spectrum is the same, typically on the order of 10 to 20 s. After one spectrum is recorded, the data is transferred from the converter card to the Data AcQuisition (DAQ) program to save the spectrum. The next measurements starts after the shutter movements are finished. This results in a measurement time of 20 to 35 minutes per delay scan consisting of 20 different delaystage positions. Several delay scans are summed up to obtain a sufficient signal-to-noise ratio. This minimizes the influence of long-time instabilities. For example, the pump or the probe beam may drift following a reduced overlap between both laser beams. A total loss of overlap would result in a featureless transient spectrum even though the transient state has not yet fully decayed. Thus both beams were routinely re-aligned every 1 to 2 hours.

5.2 One-color photoelectron spectra of NaI aqueous solution

Before presenting the electron-emission spectra from the transient electronic states, we examine the photoelectron spectra obtained when using a single laser beam. Measured one-color spectra are shown in Figure 23, where the top and the bottom panels display results for 4.65 and 3.55 eV photon energy, respectively. The

kinetic energy scale was corrected for the streaming potential. With a correction value of -0.2 eV, which is in good agreement with reference [63], both one-color spectra can be fully explained by contributions solely from ionization of the water $1b_1$, $3a_1$ states, and from ionization of iodide into the $e^-+I^0(^2P_{1/2})$ and the $e^-+I^0(^2P_{3/2})$ continuum states associated with the formation of the iodine atom in the $^2P_{1/2}$ and $^2P_{3/2}$ spin-orbit states, respectively; these contributions are denoted by $I(^2P_{1/2})$ and $I(^2P_{3/2})$ in the following. This is inferred from fitting a sum of Gaussian profiles, representing these contributions to the experimental spectra. The results of the fit are shown in Figure 23, and the respective ionization channels are listed in Table 1. Individual Gaussian fits applied for each peak are in good agreement with widths and energy positions obtained from one-photon ionization spectra of iodide aqueous solution using soft X-ray photon energies [132].

State	BE (eV)	N_{pump}	E_{kin} (eV)	N_{probe}	E_{kin} (eV)
H_2O $(3a_1)$	13.08	3	0.87	4	1.12
H_2O $(1b_1)$	11.31	3	2.64	4	2.89
$I(^2P_{1/2})$	8.96	2	0.34	3	1.69
$I(^2P_{3/2})$	8.03	2	1.27	3	2.62

Table 1: Binding energies (BE) of the initial states of water and iodide and the corresponding number of absorbed photons of the pump beam (N_{pump}) and of the probe beam (N_{probe}), and the resulting kinetic energies (E_{kin}) of photoelectrons. The BEs are taken from reference [63].

Signal from the ground-state solvated electron (BE is $\sim 3.4 - 3.6$ eV [14, 44, 45, 43]) is not apparent in the one-color spectrum measured at 4.65 eV photon energy (pump beam) because the laser pulse duration is shorter than the formation time of solvated electrons. This interpretation of the spectrum differs from the one in reference [14], where initial cold and hot states of the solvated electron have been postulated.

5.3 Time-resolved photoelectron spectra of NaI aqueous solution

5.3.1 Transient photoelectron spectra

In our measurements, the transient spectra are featureless when the 3.55 eV pulses arrive first, implying that no transient states are populated, which could

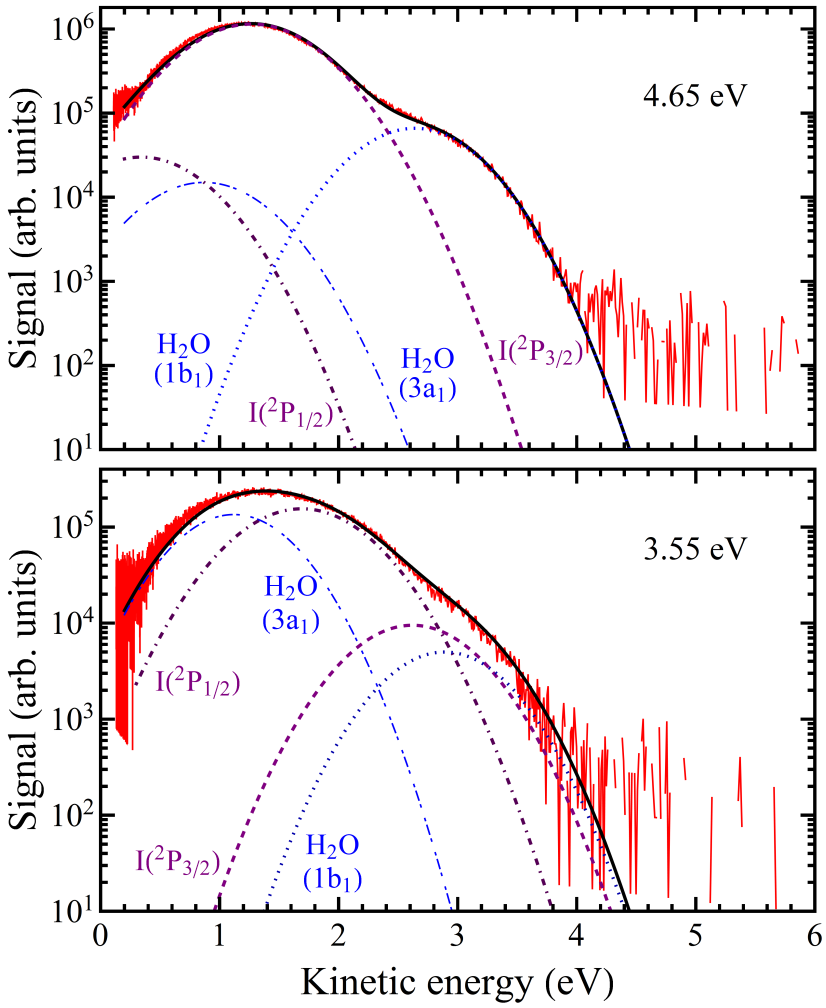

Figure 23: One-color spectra of 20 mM NaI aqueous solution obtained with the use of the pump (4.65 eV, top) and the probe (3.55 eV, bottom) beams. Black solid curves show the results of Gaussian fits. Contributions to the spectra arise from the ionisation of H_2O ($3a_1$) (blue, dash-dotted), H_2O ($1b_1$) (blue, dotted), I($5p_{1/2}$) (purple, dash-dotted), and I($5p_{3/2}$) (purple, dashed). Note the logarithmic scale of the signal intensity.

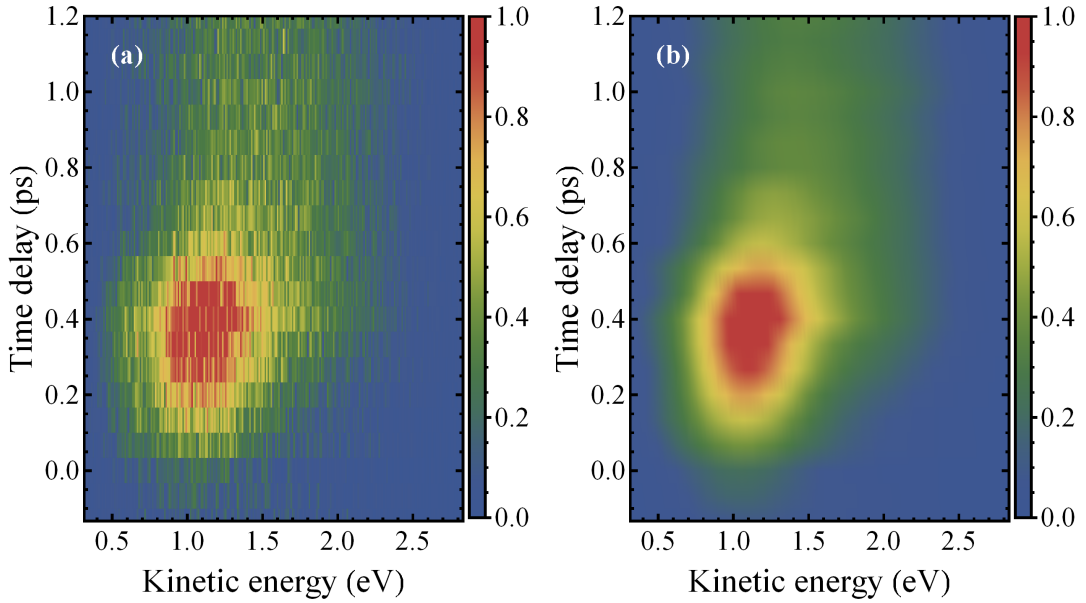

Figure 24: Normalized contour plots of the transient spectra: **(a)** Raw data. Due to the transformation function from TOF to eKE according to equation 26, the raw data is represented by an equidistant grid of 0.02 eV resolution on the eKE scale. **(b)** Transient spectra according to the fit developed in section 5.3.2. From [133].

be probed by the 4.65 eV pulses. Therefore, this case is assigned to negative delay times. Time zero ($\Delta t = 0$) was determined by modeling the dynamics of the transient signal, and will be discussed later (see section 5.3.2).

A transient spectrum at a certain delay is usually obtained by substraction of the ground state spectrum from the spectrum of the excited system.

The raw data of the transient spectra shown in Figure 24 (a) is the sum of six delay scans. Since the non-linear transformation function from the TOF- to the kinetic energy scale results in a high density of data points for small kinetic energies, the data is represented by an average to an equidistant grid with 0.02 eV resolution on the kinetic energy scale for visibility.

The analysis of the transient spectra for each delay time seperately revealed that the transient spectra can be fitted to a sum of two Gaussian-shaped distributions, which is described by

$$A_1 \, e^{-\frac{(x-\mu_1)^2}{\sigma_1^2}} + A_2 \, e^{-\frac{(x-\mu_2)^2}{\sigma_2^2}} \quad . \tag{31}$$

Chosing the starting values $\mu_1 = 1.25$ and $\mu_2 = 1.95$ from a rough manual

fit for its mean value and a fixed standard deviation of $\sigma_{1,2} = 0.5$ in the first iteration step yields an estimate for the amplitudes $A_{1,2}$ of the contributions at different times. Further iterative fitting of all values, while refining their limit, leads to the fits shown in Figure 25, examplary for the two delay times Δt. The tansient spectrum at $\Delta t = 400$ fs in Figure 25 (a) represents the instance where the electron yield of the transient signal is maximal, while at $\Delta t = 1200$ fs the transient spectrum is dominated by the signal for only one contribution as shown in Figure 25 (b). This procedure results in the values for the mean value and the standard deviation given in the following Table 2:

	μ	σ	FWHM
CTTS	1.03 eV	0.42	0.69 eV
CTTS+1	1.48 eV	0.82	1.37 eV

Table 2: Mean value and standard deviation of fitting the data according to equation 31 of the transient spectra representing the central BE and width of the CTTS and CTTS+1 states, respectively.

In summary, the pump-probe PE signal reveals two peaks at the kinetic energies of 1.03 eV and 1.48 eV at positive time delays. Considering the 3.55 eV photon energy of the ionizing probe pulse, the two peaks are assigned to transient species with 2.52 eV and 2.07 eV electron BE. Here, one-photon ionization is assumed. In the spectrum recorded at $\Delta t = 400$ fs the signal contribution of the peak at lower kinetic energy is larger than for the peak with higher kinetic energy. When increasing Δt, the relative contributions eventually invert as can be seen in the spectrum recorded at $\Delta t = 1200$ fs, qualitatively reflecting the different lifetimes of the involved transient states. A plot of the pump-probe PE signal reconstructed from the Gaussian fits to the raw spectra, as a function of both the kinetic energy and the time delay, yields the contour-plot presented in Figure 24(b).

Comparing the data of Figure 24 with the data from V. Vilchiz et al. [68], Y. Tang et al. [61] and F. Buchner et al. [69] (see Figure 4), where an energy shift of the transient signal to higher BE was observed and assigned to the formation of the solvation shell around the solvated electron, reveals a significant difference. The transient spectra presented here show higher kinetic energies at later times, which corresponds to smaller BE. This excludes an analogue interpretation of the formation of the solvation shell of solvated electrons. Since a decrease in BE of a state requires energy, our observation cannot be explained by a shift. The transition of the transient state with 2.52 eV BE into the other transient state with 2.07 eV BE can be excluded.

Both the 2.52 and the 2.07 eV BE peaks are seen to remain at constant energy over the delay scan.

The transient state corresponding to a BE of 2.52 eV can be assigned to the CTTS of iodide in very good agreement with the literatur value of 2.5 eV [61]. An emergence of this transient signal simply from the cross-correlation of both pulses can be excluded. The duration of the pulses should be approximately 200 fs providing both pulses exhibit similar temporal profiles. In the case of one pulse being short (∼60 fs), the duration of the other pulse must exceed 300 fs. The pulse durations used here are aproximately 60 fs. A cross-correlation can also be excluded, since there is no BE in the ground state system (see table 1) which would lead to an electron kinetic energy of 1.02 eV by multiphoton ionization in which at least one photon of each pulse contributes.

Due to the small probe photon energy of 3.55 eV applied in the present experiment, signal contributions from ionization of species evolving with yet higher BE cannot be accurately quantified. But the data suggests that there is no or only minor transformation from the CTTS into the I:e^- pair, which eventually equilibrates to the solvated electron while increasing its BE. This shift, as observed in other studies [61, 14], is not observed.

A negative transient signal, which could originate from a decreased population of a ground state after excitation, is not observed. This can be explained by the low excitation and ionization yield of the sample solution, which still leaves most molecules and ions in their ground state. Thus the change in the concentration of iodide due to ionization is minimal. The missing information about the concentration of the excited species prevents the quantification of the ionization yield of the transient signal.

There is another channel to generate solvated electrons other than excitation into the CTTS state of iodide. This is the transformation of an electron in the conduction band into a solvated electron as explained in section 2.2.1. This channel was not observed most probably due to a very small ionization cross-section of the quasi-free electrons in the conduction band. Since the photon energy of the probe pulse and the collection efficiency of the spectrometer prohibit the detection of fully solvated electrons, the dynamics of the two population channels can unfortunately not be determined here and will be the basis for future experiments.

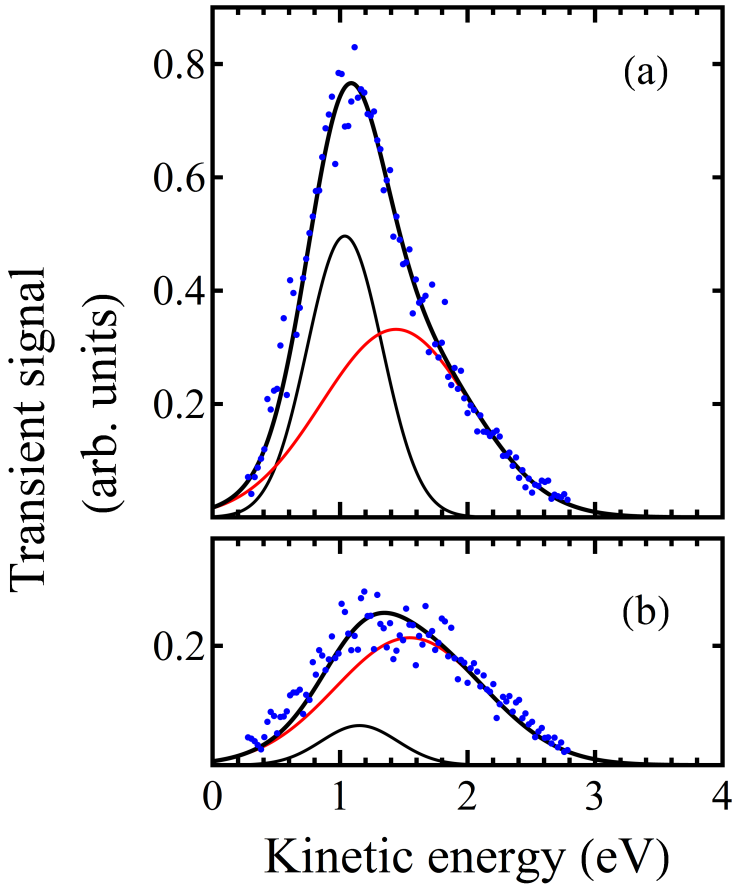

Figure 25: Transient signal at the pump-probe delay times of 400 fs (a) and 1200 fs (b) of 20 mM NaI aqueous solution. Dots (blue) represent the experimental data. Black and red curves show individual contributions of the two Gaussian peaks (CTTS and CTTS+1, respectively) obtained from the fit. Their sum is represented by the thick black curve. From [133].

5.3.2 Electron dynamics, kinetics, and modeling

Modeling the dynamics of the solution is based on the transient signal discussed in the previous section 5.3.1. The underlying data is the integrated Gaussian contributions from both states, which is plotted in Figure 26.

Since the transient state with the BE of 2.52 eV is already identified as the I^-_{aq} CTTS state, the assignment of the other transient state at a BE of 2.07 eV is given upfront: It is the I^-_{aq} CTTS+1 state. This assignment is based on the population and de-excitation dynamics of the system as will be explained

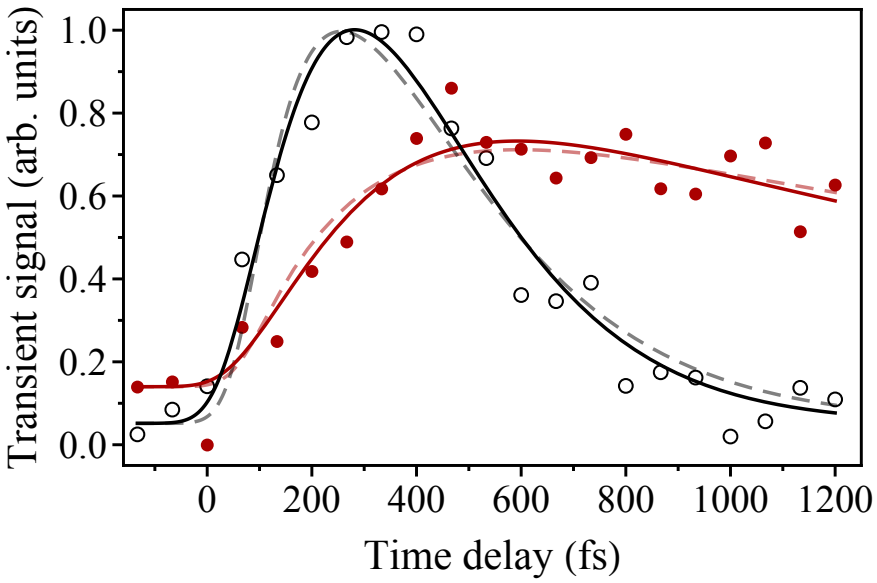

Figure 26: Time dependency of the ionization yield from the transient states of 2.52 eV (black circles) and 2.07 eV (red dots) binding energies. Solid curves represent results of the model described by equation (32). The dashed curves show results of the model with the intermediate state I being excluded.

in the following. This rules out excitation of the CTTS+1 state, which lies energetically above the CTTS state, due to one-photon absorption. The pump pulse photon energy of 4.65 eV is not high enough to populate the observed I^-_{aq} CTTS state with a BE centered at $\sim$ 2.5 eV [61] by one-photon absorption. Figure 3 compares the spectral shape of the pump pulse used in this experiment with the absorption spectrum of an iodide aqueous solution. Even though both curves are well separated in the figure, there is still the possibility of populating the low-energy tail of the CTTS band, as suggested in the recent fluorescence study by Messina et al. [72]. They used a similar pulse with a wavelength also centered at 267 nm (4.65 eV) to excite the lowest CTTS state of iodide.

The observation of the transient species at an electron kinetic energy of 1.48 eV (assigned to the CTTS+1 state) via absorption of two photons of the probe beam can be ruled out due to energy mismatch. The BE of this transient state would be centered at 5.5 eV, which is 2.5 eV above the lowest BE of 8.03 eV of the system (see Table 1). Considering the FWHM $\Delta BE \approx 1$ eV of this state [63], the difference of 2.5 eV is too large to probe an excited high-energy tail of this state via two-photon absorption. Also electronically excited transient states in water have not been observed under comparable two-photon excitation in conjunction with a third probe photon [134].

In our experiment, the CTTS and the CTTS+1 states are populated via two-photon excitation of iodide, which results in two excited states $X_{1,2}$, where electrons exhibit an energy of 0.3 and 1.3 eV above the vacuum level. A scheme of the excitation process is depicted in Figure 27 (a). These energies are defined by the difference between the absorption energy of two photons and the BE of iodide attributed to the $I^-_{(aq)}(5p_{1/2})$ and the $I^-_{(aq)}(5p_{3/2})$ initial ground-state energies, respectively. The exact nature of $X_{1,2}$ is not known though but it is likely of CTTS character as well, analogous to the findings in a chloride aqueous solution [135], where energies of 0.4 and 1.9 eV above the vacuum level were observed as well. Here, the continuum states $X_{1,2}$ are not explicitly observed in the transient spectra most probably because of a low ionization cross section of these states, and due to insufficient time resolution of the experiment. But they are needed in order to explain the population and relaxation dynamics of the observed transients as will be shown next.

In order to determine the population and relaxation dynamics of the CTTS and CTTS+1 transient states observed in the PE spectra, the respective time-dependent ionization yields displayed in Figure 26 are examined. The yields are obtained by integration of the PE signal for a given delay time. Since both transient peaks are sufficiently well separated in the energy spectra, the kinetics of the electron population can be analyzed individually for each of the two spectral components. This makes modeling in principle more unique, as compared to fitting the total electron yield of the transient in which case important information remains unconsidered. On the other hand, the system is yet too complex for a complete and accurate description of the relaxation dynamics. The reason is that experiments, the one reported here and previous time-resolved PE or transient absorption studies, probe only a fraction of all possible channels, namely the ones leading to population of the CTTS states. Unless all competing relaxation channels, which can be of non-radiative or radiative character, are taken into account quantification of the electron dynamics is elusive. And yet, with the experimental information of Figures 24, 25 and 26, several conclusions regarding the excitation and immediate de-excitation dynamics in NaI aqueous solution can be drawn. This is achieved by developing a model that describes the observed temporal evolution of ionization yields in Figure 26.

The main model ingredients include the first excited states $X_{1,2}$, which are treated as a single state X for simplicity, one intermediate state I and both observed CTTS and CTTS+1 states. The simplification of the excited states to a single state X implies either that both states undergo similar relaxation dynamics, or only one of those states is populated and relaxes into the lower-lying CTTS states.

First trail simulation showed, that a decay from the first excited state directly into the CTTS and CTTS+1 states does not result in an acurate description of the rising edge of the CTTS state. Therefore the introduction of an intermediate state I is required into which the first excited state decays and whose subsequent decay populates the observed CTTS and CTTS+1 states. This model is depicted in Figure 27 (b) in a combined energy-level - electronic-transition scheme.

Both the X and I states are also allowed to decay via other channels, not leading to population of the CTTS states. An additional decay channel can be in competion to the population of the CTTS states, but our experiment does not allow its detection. For example, we are unable to detect photons originating from a possible fluorescence channel. Thus, the nature of these channels is not detailed here. Finally, the CTTS and CTTS+1 states are allowed to decay. This leads to the following system of differential equations which is used to describe the temporal evolution of the electron yields of the measured transient spectra:

$$\begin{aligned} \dot{n}_X &= -\frac{1}{\tau_X}\, n_x + P(t) \quad , \\ \dot{n}_I &= w_{X\to I}\, n_X - \frac{1}{\tau_I}\, n_I \quad , \\ \dot{n}_{C_0,C_1} &= w_{I\to C_0,C_1}\, n_I - \frac{1}{\tau_{C_0,C_1}}\, n_{C_0,C_1} \quad . \end{aligned} \tag{32}$$

Here n_{X,I,C_0,C_1} denote the populations of the X, I, CTTS, and CTTS+1 states, respectively, τ_{X,I,C_0,C_1} represent their lifetimes, $w_{X\to I}$, $w_{I\to C_0}$, and $w_{I\to C_1}$ are the rates of the relaxation transitions depicted in Figure 27(b), and $P(t)$ describes the time-dependent population rate of the X state with the actual temporal envelope of the pump pulse taken into account, which is assumed to be Gaussian. Apart from the decay rates of the X and I states considered in equations (32), other relaxation channels of these states are represented by the rates w_X^r and w_I^r, respectively. These channels decay can be of radiative and non-radiative character, for example caused by geminate recombination of electron-iodine pairs or by direct relaxation to the solvated electron state. The relation between the lifetimes and the decay rates of the X and I states can be expressed as

$$\begin{aligned} \frac{1}{\tau_X} &= w_{X\to I} + w_X^r \quad , \\ \frac{1}{\tau_I} &= w_{I\to C_0} + w_{I\to C_1} + w_I^r \quad . \end{aligned} \tag{33}$$

The system of differential equations in equations 32 was solved numerically with the initial condition that all involved states were unpopulated at $t \to -\infty$. The

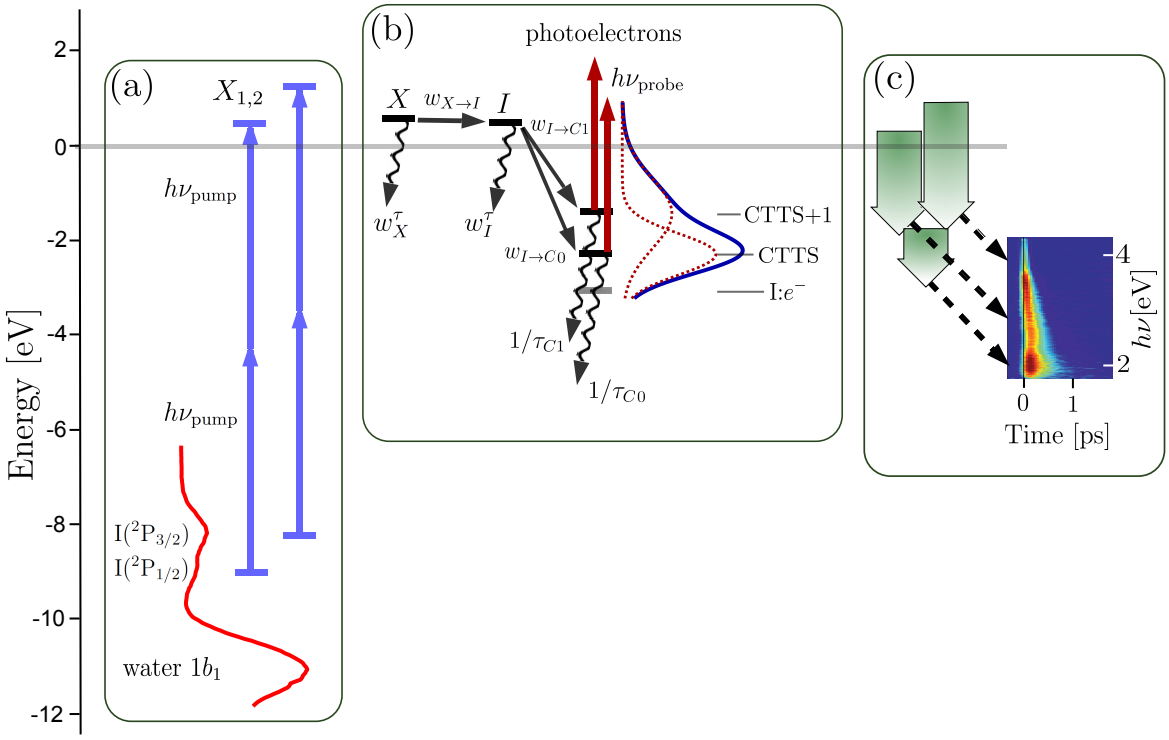

Figure 27: **(a)** Depiction of the two-photon absorption process leading to population of the $X_{1,2}$ states above the vacuum level. All energies are drawn to scale. The PE spectrum (red curve) was measured from 3M NaI aqueous solution using synchrotron radiation of 180 eV photon energy [136]. Peaks due to ionization of I^-(aq) with the formation of $I(^2P_{1/2})$ and $I(^2P_{3/2})$ states, and ionization of the water valence orbital, $1b_1$, are labeled. **(b)** Decay scheme of the $X_{1,2}$, I, CTTS, and CTTS+1 states, modeled with the use of Eq. 32, and depiction of ionization of the transient CTTS and CTTS+1 states. The PE spectrum is a reproduction of the one in figure 25(a). **(c)** Depiction of de-excitation transitions, $X_{1,2}$ $\rightarrow$ CTTS/CTTS+1 and CTTS/CTTS+1 $\rightarrow$ $I_0{:}e^-$. Right: Reproduction of the time-resolved fluorescence spectrum from reference [72]. The correspondence in energies with the present experiment is indicated by dashed arrows.

ionization signal from the CTTS and CTTS+1 states was calculated by convolution of $n_{C_0}(t)$ and $n_{C_1}(t)$ with the temporal Gaussian envelope of the probe pulse (see Figure 30), assuming that the probe step is non-saturated. The numerical model is fitted to the experimental data by means of a Nelder-Mead algorithm [137].

The fitting results are presented in Figure 26 by the solid lines and show a good agreement with the experimental data. However, not all time constants of the transitions depicted in Figure 27 (b) can be unambiguously defined from the fit. In particular, the fit results are insensitive to the branching between $w_{X\to I}$ and w_X^r rates for the decay of the X state. Only the lifetime τ_X can be inferred from the fit as a robust parameter. This is also the case for characterization of the I state. The fit does however yield a robust value for the lifetime τ_I but the decay branching into the CTTS and CTTS+1 states and other channels cannot be reliably determined. This restriction is directly related to the fact that we probe solely the populations of the CCTS and CTTS+1 states.

Model	τ_X	τ_I	τ_{C_0}	τ_{C_1}
$X \to I \to C_{0,1}$	150 fs	150 fs	130 fs	1.5 ps
$X \to C_{0,1}$	220 fs	-	170 fs	2.0 ps

Table 3: Lifetimes of the X, I, CTTS, and CTTS+1 states obtained from the modeling of the population and relaxation dynamics according to equations 32, and from the modeling with the intermediate state I being excluded.

The inferred lifetimes are presented in Table 3. We find that the decay time constants of the CTTS and CTTS+1 states are ~ 130 fs and ~ 1.5 ps, respectively. Their decay products are not specified here. The time constant for the decay of the CTTS state derived here agrees well with the results from resonant-excitation experiments [61]. This is perhaps not surprising when we assume the presence of a potential barrier for reaching the CTTS state. This barrier may be already small for transient states with energy of ≥ 1 eV above the lowest CTTS state.

We also applied a model, similar to the one described above, where we excluded the intermediate state I. The results of this model are also shown in Figure 26 by the dashed line. One can see that they reproduce the experimental data less satisfactory. In addition, simulations were performed where both the two-step and the direct decay of the X state into the CTTS and CTTS+1 states was allowed. The respective fit to experimental data revealed that the two-step relaxation rate is dominant. Therefore, we conclude that the intermediate state I needs to be involved in the interpretation of our experimental observations.

The nature of the intermediate state I cannot be clearly identified. When assuming the excitation into higher-lying CTTS-like states above vacuum similar to [135], where the electron remains in the proximity of its parent atom, the system might relax through a lower lying CTTS-like state before the electron is situated in the CTTS or the CTTS+1 state. Another interpretation of the nature of the I state can be inferred from the results of earlier studies on capture of slow electrons in gaseous media [138]. It was discussed that at high medium densities the three-body collisions of an electron and two neighboring molecules become probable. This gives rise to a two-step process of non-radiative electron recombination via formation of a short-lived intermediate quantum system. This system represents a vibrationally excited molecular negative ion, which can be de-excited in a second collisional step. Analogously, one can consider that the I state belongs to a $H_2O^* : e^-$ system, with a total energy matching the energy level of the X state. The latter interpretation does not necessary require the excitation of the electron into a state above the vacuum level, which is related to the parent atom. But it must return to an iodine atom, due to the low concentration this is most probably the parent atom, to transfer into the CTTS or CTTS+1 states.

Very similar results can be obtained when assuming that CTTS+1 and CTTS states are independent or coupled. Here, the coupled case represents a decay from the CTTS+1 state into the CTTS state. In a theoretical work by Sheu and Rossky [65] the excitation into a state above the CTTS state is discussed based on the experimental data by Long et al., where pulses of 312.5 nm wavelength ($\sim$ 4 eV, well below the photodetachment threshold of 5.5 eV [11]) illuminated a 1 M NaI solution [139] and excite the CTTS states via two-photon process. Later W.-S. Sheu and P. J. Rossky simulated the decay from higher-lying CTTS states into the lowest CTTS state. They concluded, that in addition to direct photodetachment, which is a minor channel, the transition of this higher-lying CTTS state into the lowest CTTS state and subsequent photodetachment happens on a time scale of 0.7 - 1 ps. The lifetime of 1.5 ps to 2 ps found in our experiments differ from the theoretical values by a factor of $\sim$2. This deviation might be due to a quite different structure motif of an iodide-electron pair in terms of the surrounding solvent cage arrangement, and may be related to the excited state X solvation structure formed at large excess energy ($>$ 9 eV photon absorption process). However, no experimental information was obtained that supports such a hypothesis and further investigations are needed to clarify this matter. It cannot be excluded that the unexpected long lifetime of the 2.07 eV BE species might indicate that the broad width of this energy peak is not exclusively due

to CTTS+1 photoemission. In either case, coupled or independent, successful modeling requires a two-step relaxation of $X_{1,2}$ via an intermediate state I to populate the CTTS states.

The discussion of the experimental data would be incomplete without attempting to connect to the study of Messina et al. [72], summarized in section 2.2.2, which uses the same photon energy, similar pulse energy, and only the NaI concentration is different, 1M versus 20 mM in the present study. What is curious here is that the two studies are seemingly sensitive to entirely different excitation routes, and hence very different relaxation channels are probed in each case. Messina et al. considers electronic excitation at the very onset of the CTTS absorption band, while the present work explores an indirect pathway, populating CTTS states through a continuum state. In our attempt to find out how these two studies possibly connect in terms of the information extracted (state assignment, relaxation mechanism) we noticed that the time-dependent fluorescence appears to match remarkably well the processes presented in Figure 27 (b). Specifically, a good match between the emission wavelengths and the electron BEs and, in part, even with the respective temporal characteristics can be found. The former case is illustrated in Figure 27 (c) which depicts the principle transitions from the $X_{1,2}$ states and from the lower-energy CTTS states. In the figure we also include the sovated electron. Downward arrows represent the electronic decay transitions, and the arrow lengths correspond to actual energy differences. For example, $\mathrm{BE}_{X_1}-\mathrm{BE}_{\mathrm{CTTS}}$ represents the largest energy difference of 3.8 eV (center to center), and $\mathrm{BE}_{X_2}-\mathrm{BE}_{\mathrm{CTTS+1}}$ has the smallest value of 2.4 eV. The lower arrow depicts the analogous energy release corresponding to the transition of the CTTS+1 and CTTS states into the solvated electron. Dashed cross-linking arrows mark the corresponding energy ranges in the fluorescence spectrum which is reproduced from reference [72] at the right of Figure 27 (c). The incomplete correspondence to the lowest-energy transition of $\sim$ 1 eV is of technical reason that caused a cutoff at $\sim$ 1.8 eV (700 nm) in the experimental fluorescence spectrum [72]. So far we have no satisfactory suggestion how to simultaneously interpret these two studies.

To reinforce the interpretation of our data, the most promising aspect would be the use of higher photon energies as a probe. This would facilitate the confirmation of the relaxation of the CTTS state into the solvated electron and could possibly also resolve the relaxation of the CTTS+1 state. This is accompanied with a higher possibility of an excitation of the system by this beam, for example one-photon excitation into the CTTS manifold if the photon energy exceeds the value of 4.65 eV of the pump pulses photon energy. Thus a photon energy of

7.5 eV (fifth harmonic of the Ti:Sapphire laser) or even higher (XUV pulses) is a good basis for future experiments. Additional benefits of the use of XUV pulses as a probe are discussed in section 6.2.

6 Outlook

6.1 Polarisation dependent transient photoelectron spectra

The transient PE spectra presented in chapter 5 was recorded with the polarization vectors of both laser beams being parallel to the (averaged) detection axis of the spectrometer. In addition pump-probe spectra for different polarization vectors of the pump laser beam were recorded. This approach is conceptually different from typical experiments investigating the PAD as described in section 3.1.1, where the angle between the polarization vector of the probe beam and the detection axis of emitted electrons is varied. The idea of such an experiment was motivated by the question wether the laser pump pulse may have an effect on the symmetry of the excited intermediate which is then interrogated by the ionization pulse, the probe pulse.

For the data acquisition three different PE spectra (pump, probe and pump - probe) were recorded to obtain the transient spectrum at a certain time delay and polarization vector of the pump beam. The latter was varied between 0° and 180° in steps of 10° using a $\lambda/2$ plate with 0° representing a parallel polarization vector of the pump beam with respect to the (averaged) detection axis. Figure 28 shows the integrated transient signal intensity obtained for the 0.28 to 1.62 eV BE window, which includes signal from the CTTS state. Measured data (black dots) are presented for time delay of 200 fs as a function of the angle α between the polarization vector of the pump pulse and the detection axis. Interestingly, the data shows a dependence of the PE signal in this energy range on the polarization vector of the pump beam with a maximum at $\alpha = 0°$ and a minimum at $\alpha = 90°$.

The black curve in Figure 28 is a fit to the experimental data using the following equation

$$S \propto A(1 + \beta' P_2(\cos\alpha)) \quad , \tag{34}$$

where S is our transient signal strength, P_2 is the Legendre polynominal of second order, α is the angle between the pump beam and the detector axis, and A and β' are fitting parameters. This function is derived from equation 6 and reproduces the experiment quite well. However, we believe that rather empirical function does not reflect the physics at play. In fact, we would argue that the polarization vector of the pump laser pulse has an effect on the PAD implies some induced electronic orientation characteristic of the intermediate state. If this is the case one of the main assumptions of equation 34, namely the random orientation of

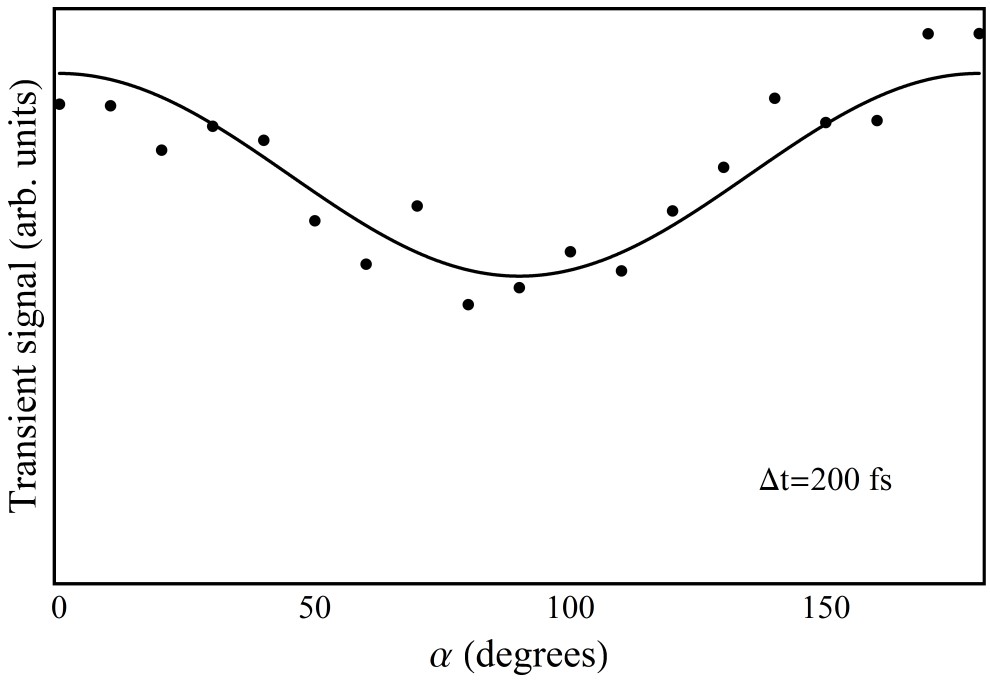

Figure 28: Dependence of the transient signal of the contribution assigned to the CTTS state on the polarization of the pump beam at a time delay $\Delta t = 200$ fs. An angle of 0° corresponds to horizontal polarization. The dots represent the measured PE, while the line shows the fit according to equation 34.

molecules, may be violated to some extent. Hence, our findings seem to resemble the situation where a laser pulse is used for molecular orientation, and this will considerably alter the PAD probed by the subsequent ionization laser pulse. As discussed in several works [90, 93] the modified PAD can adopt very complex forms, and cannot be described by equation 6.

To explore such pre-orientation in further detail analogous measurements were performed for different delay times revealing that such polarization dependence occurs only for short time delays. Results are shown in Figure 29, where the data of the CTTS+1 state is also included. The black dots and red squares represent the fitting parameter β' for the CTTS and CTTS+1 state, respectively, according to equation 34 for each individual scan at various time delays. For comparison of the temporal evolution β', the recorded total ionization yield from the CTTS (grey shade) and CTTS+1 state (red shade) as discussed in the previous chapter, see also Figure 26, is presented in the shaded background.

Our findings of Figure 29 suggest that the CTTS+1 state does not exhibit any noticeable dependence on the polarization vector. A more conclusive interpreta-

tion of the several observations in Figure 28 and 29 cannot be provided here as this would require more systematic measurements, exploring for instance fluence dependence of the pump laser pulse. But also the use of higher-photon-energy probe pulses, now available by our new HHG source, may be very useful, allowing quantification of photoionization cross section effects. For the moment we can only speculate on the origin of our experimental findings. Probably the most important questions to answer are whether the observed polarization dependence is a ground state effect or whether it is indeed due to some dynamical processes connected with the preparation of the excited state. Second question is why the effect is absent for the CTTS+1 state. One could argue that the promotion of an electron from the iodide p-orbital into the CTTS state indeed exhibits an angular dependence, and the situation may be different for the CTTS+1 state with different symmetry. In this picture the 300 fs window, within which polarization matters, could be perhaps assigned to the same solvent-shell rearrangements as discussed in chapter 2.

6.2 High-order harmonic generation (HHG) as a probe

There are many advantages, both of physical and technical nature, of a table-top HHG source for laser pump - XUV probe experiments. These advantages include the availability of photon energies in the range from 20 eV to over 100 eV depending on the separated harmonic and noble gas used in the generation process (cut-off). This enables to probe the system by one-photon ionization of the valence electrons of the system under investigation. Compared to multi-photon ionization, spectra in which all contributions originate solely from one-photon ionization are easier to interpret. One reason is that in the latter case the ionization- and absorption cross-section of many atoms and molecules has been measured and is theoretically predictable. This also includes different aggregate phases of the elements. The cross-section of multi-photon ionization is more difficult to predict, since the ionization-yield can be enhanced through bound states, which act as an intermediate step. The level of this resonance enhancement depends strongly on the photon energy and therefore adds another degree of freedom. The fact that states of a system with different BE, which obviously yield well seperated contributions in the one-photon regime can be ionized by a different amount of photons in the multi-photon regime possibily leading to an overlap of the contributions in the spectra measuring the electron kinetic energy. An example is the one-color spectra shown in Figure 23, where the contributions from $H_2O(1b_1)$ (4-photon ionization, $E_{kin} = 2.89$ eV) and the $I(^2P_{3/2})$ (3-photon ionization, $E_{kin} = 2.62$ eV) are separated by less than 0.3 eV even though their

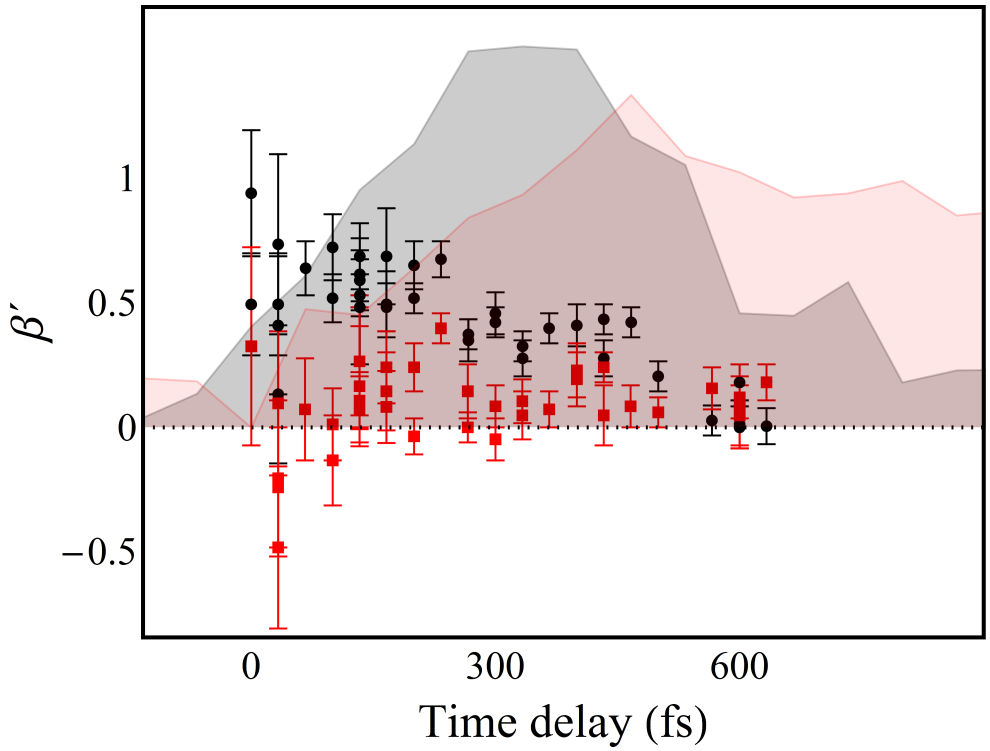

Figure 29: The difference in the PE yield of the CTTS (black dots) and CTTS+1 (red squares) expressed in terms of the parameter β' according to equation 34 at different time delays Δt. Errorbars represent solely the accuracy of the fit. For comparison with the total PE yield at parallel polarization, the data of figure 26 is shown in the shaded background.

BEs differ by more than 3 eV (see also table 1). This makes it more difficult to assign precise ratios between these contributions.

Another major advantage of using XUV pulses is their clear designation as the probe. This designation follows from the different energy regions of the PE originating from the XUV- and the laser pulses. While the laser pulses usually yield PEs with kinetic energies below 5 eV, the PEs from the valence band ionized by XUV photons are typically above 10 eV. The latter region is the region of interest for a possible transient species since the excitation yields the transfer of electrons into higher-lying states of the valence band or states above the valence band (e. g. CTTS states). There is no competition between excitation and ionization. Pulses with similar wavelength in the visible or UV can lead to excitation of the system by both pulses. Thus, depending on the time delay between both pulses the designation as pump and probe reverses. Depending on the intensity, different wavelength and different amount of photons can even yield excitation into

the same state of the system making the analysis and interpretation difficult.

Since the XUV-probe is solely a one-photon ionization process, measuring the PAD can lead to clear assingments concerning the orbital configuration of the probed state. This applies also for excited states giving access to a more detailed analysis of the orbitals of these states and even their temporal evolution.

A clear separation in photon energy between the pump pulse and the probe pulse is also possible by using X-rays produced at synchrotrons or Free-Electron Lasers (FEL) as probe. An advantage of X-rays produced at synchrotrons is the broad range of available photon energies acompanied with high resolution. For example, the beamline U41-PGM at BESSYII can be set to any photon energy in the range from 170 eV to 1800 eV at a resolution of > 2000 while maintaining a photon flux of $10^{12} - 10^{13} 1/s$ [140, 141]. Here the K-edge of the lighter elements, like carbon (284.2 eV), nitrogen (409.9 eV) or oxygen (543.1 eV) can be excited and ionized[5]. Additionally the L- or M- shells of heavier elements can be excited. Resonant excitation of the L-edge can reveal information about the LOMO. The major disadvantage of laser pump - X-ray probe experiments at synchrotrons is the duration of the X-ray pulses, which are on the order of $\sim$ 50 ps and thus prohibits the investigation of femtosecond processes. Also, the pulses of the laser used for excitation must be synchronized to the pulses of the synchrotron, which requires significant additional technical effort.

Femtosecond dynamics can be probed at synchrotrons by using the slicing technique [143, 144, 145, 146]. Here, the electron bunch, a cloud of electrons exhibiting the shape and dimensions of an ordinary needle, from which the light originates due to moving through the magnetic field of an undulator is deformed by a synchronized femtosecond laser pulse creating a bump. Apertures after the undulator only pass the light generated by this bump. Pulse durations of 100 fs can be achieved. Even though this technique is designed to investigate femtosecond dynamics, the decreased photon flux of approximately 50 photons per pulse at a repetition rate of 6 kHz at the slicing beamline at BESSYII [147], which is $\sim$ 3 orders of magnitude lower than in normal operation, complicates experiments on diluted systems by the increased data accquisition times. Besides solid samples, the only diluted systems investigated using the slicing technique were aqueous $[Fe(bpy)_3]^{2+}$ in the hard X-ray regime [148] and $[Fe(tren(py)_3)]^{2+}$ dissolved in acetonitrile in the soft X-ray regime [123], where in both cases the femtosecond dynamics were investigated by TA measurements in transmission mode. In the latter case, the liquid sample was prepared in a static cell, i.e. between two SiN-membranes. There are 3 synchrotron facilities worldwide pro-

[5]Values are taken from [142]

viding femtosecond pulses (ALS, SLS and BESSYII), from which only BESSYII is still in operation today.

The principle of light production in a FEL is similar to the one at synchrotrons. The sinusoidal motion of the electrons in the magnetic field of the wiggler exhibits a larger amplitude compared to the undulator used at synchrotrons. A FEL generates a broader spectrum and an orders of magnitude higher maximum photon flux. Due to a longer pathway with more alterations of the magnetic field and the synchronization of the velocity of the electron bunch and the generated electric field, the electron bunch undergoes so-called microbunching. The sinusoidal motion of the electrons produce an electric field, which forces the electrons to clump within the period of this field producing a coherent photon pulse, which exhibit a duration of a hundred or a few hundredths of femtoseconds. Due to the fact that free electrons do not have discrete energy levels, in principle the emitted photon energy can be set with infinite variability over the range from microwaves to hard X-rays. The first measurements investigating the ultrafast dynamics of a solution, aqueous $[Fe(bpy)_3]^{2+}$, have been conducted at an X-ray FEL (XFEL) in 2013 via femtosecond time-resolved X-ray Absorption Near-Edge Spectroscopy (XANES) [149]. Here jitter of the electronic signals for synchronization of the pump laser and the XFEL probe exceeds the necessary requirements for femtosecond resolution. Hence, for each shot the time delay between both pulses must be measured. Since an XFEL typically offers the operation of only 1 or sometimes 2 beamlines in parallel, experimental time is rare.

The tabletop HHG system designed for UV-vis pump - XUV probe experiments on liquids [150] uses the same laser as described in section 4.3. The HH are generated in a gas cell filled with argon gas at approximately 20 mbar into which the 25 fs laser pulses are focused. The separation is accomplished using an off-axis zone-plate monochromator [151, 152], and a slit only passes the desired harmonic. A toroidal mirror fucuses this harmonic into the interaction region. The UV-vis pump beam is intruduced into the experimental chamber through a vacuum window (UV-fused silica) and an adjustable mirror, which is positioned so the XUV beam can just pass and both beams cross the interaction region under an angle of less than 2° with respect to each other. A drawing of the design of the main parts can be found in appendix B. The pump beam can be generated in the OPA in the range from ∼250 nm to ∼1.9 μm and is intrinsically synchronized to the XUV-probe pulses, since they are generated by the same laser source.

The alignment of the optical elements could be optimized to achieve pulses with a duration of 45 fs [150]. This is on the same order as the pulse duration at XFELs. The spectral bandwidth ΔE_{FWHM} is dependent on the pump irradiance.

A decrease from 2.35×10^{14} W/cm^2 to 1.5×10^{14} W/cm^2 yields a change from $\Delta E_{\mathrm{FWHM}} = 0.81eV$ to $\Delta E_{\mathrm{FWHM}} = 0.3eV$, respectively. The photon flux was measured by the photodiode positioned behind the slit to 10^6 photons per pulse at an irradiance of 2.35×10^{14} W/cm^2.

7 Conclusions

Using liquid-jet time-resolved photoelectron spectroscopy in conjunction with femtosecond UV laser pulses this thesis has explored the early-time dynamics of CTTS population of iodide in water. Near-threshold ionization of NaI aqueous solution, which leads to the instantaneous population of highly excited states with energies above the vacuum threshold, is shown to be an alternative route for populating CTTS states so far not considered in previous works. The same CTTS states are accessed by resonant photodetachment from iodide, and are known to dissociate with a high probability for subsequent formation of the hydrated electron. Based on measured population times, the present data indicates that the character of the initial solvent cage structures around the two-photon excited iodide is similar to the case of one-photon induced detachment. Also subsequent dynamical response of the water solvent is similar, as the large excess energy is rapidly dissipated via relaxiation. Although the present study has demonstrated the differences of above-vacuum excitation for populating CTTS states the work also raises several questions that could not be fully answered here. This particularly refers to the nature of the near-vacuum transient CTTS-type states, and it also takes future studies to resolve the very different relaxation dynamics observed for the CTTS and CTTS+1 states. Further experiments will also explore the importance of water multi-photon absorption and also the origin of the anisotropic angular distribution of the emitted photoelectrons due to ionizing CTTS state remains to be understood.

Experiments reported in this thesis were carried out in the newly built setup presented in chapter 4.2 which was initially constructed for measurements using XUV radiation generated by HHG in the laboratory. This latter source became operative only during the end of my studies, and experiments were rather performed with the laser system. The magnetic-bottle time-of-flight electron spectrometer was well suited also for the detection of few-eV photoelectrons. Its initial optimization was performed for larger kinetic energies, up to 1000 eV, for probing the photoelectrons ionized by soft X-rays, available at the synchrotron facility BESSYII in Berlin. The detailed optimization of the spectrometer and the determination of performance parameters (discussed in full in section 4.2.2) was a major part of the first half of my thesis work. My initial work also required development of very stable liquid jet in order to collect photoelectron spectra over the course of many hours due to the low signal intensity from the pump-probe photoelectron experiments from solution. This is achieved by the implementation of the recycle microjet technique (discussed in section 4.1), which offers uninterrupted measurement condition over several hours and the possibility of recycling

expensive or rare sample.

A Spectral widths of the pump and probe laser pulses

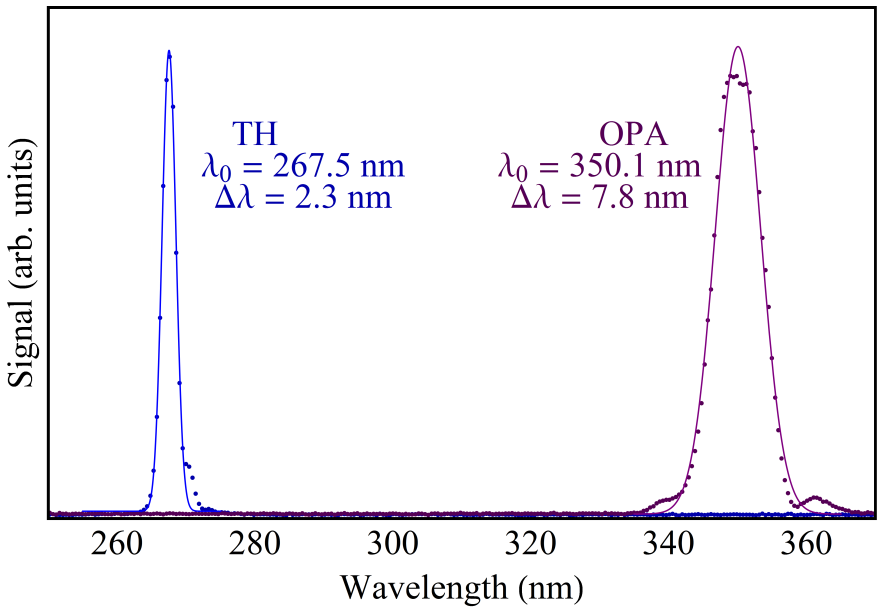

Figure 30: Optical spectrum of the pump (blue) and the probe (purple) pulse. The dots represent the measured values, while the line represents a fit assuming Gaussian shape. λ_0 is the central wavelength and $\Delta\lambda$ the FWHM of the spectral width.

B Design of the HHG setup

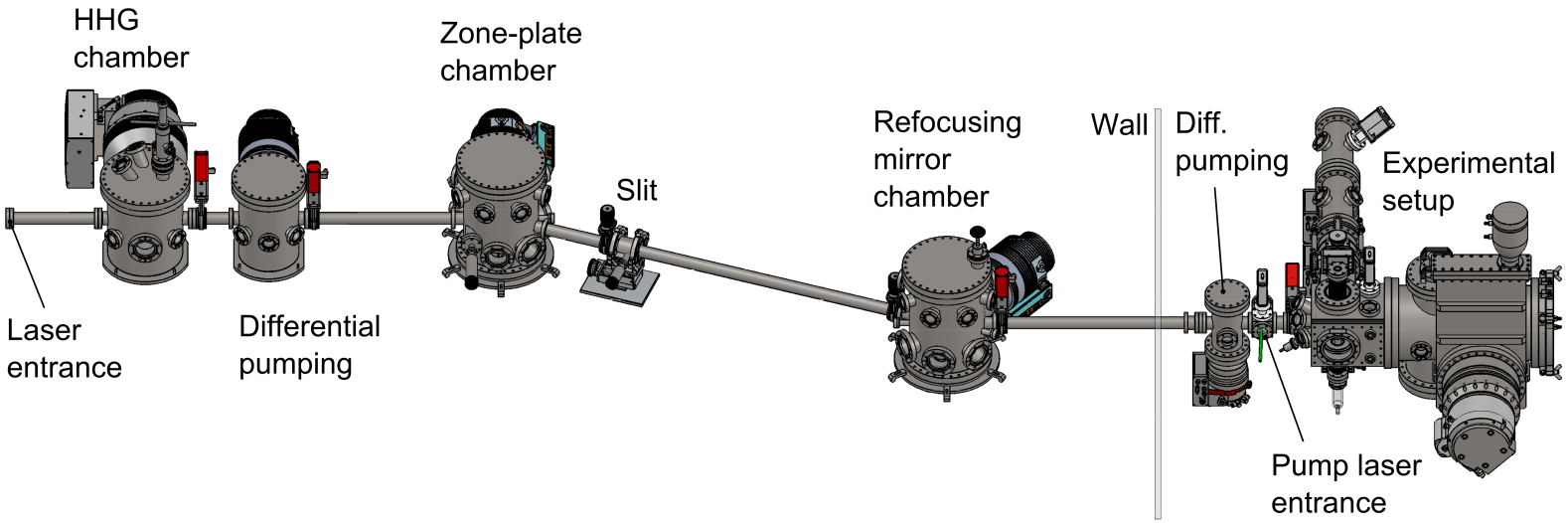

Figure 31: Schemetic of the design of the main parts of the newly built HHG line at FU. For details see [150]

List of Abbreviations

BBO	Beta-bariumborat
BE	Binding energy
BESSYII	Berliner Elektronen-Speicherring Gesellschaft für Synchrotronstrahlung II
CCD	Charge-coupled device
CTTS	Charge-tranfer-to-solvent
DFT	Density functional theory
DAQ	Data acquisition
DNA	Deoxyribonucleic acid
EAL	Electron attenuation length
EMFP	Elastic mean free path
ESCA	Electron spectroscopy for chemical analysis
FEL	Free-Electron Laser
FWHM	Full width at half maximum
FY	Fluorescence yield
HH	High-order harmonics
HHG	High-order harmonic generation
HOMO	Highest occupied molecular orbital
HV	High vacuum
IMFP	Inelastic mean free path
IR	Infra-red
LASER	Light amplification by stimulated emission of radiation
MCP	Micro-channel plate
OPA	Optical parametric amplifier
PAD	Photoelectron angular distribution
PE	Photoelectron
SHG	Second harmonic generation
TA	Transient absorption
THG	Third harmonic generation
TOF	Time-of-flight
TR-TAS	Time-resolved transient absorption spectroscopy
TR-PES	Time-resolved photoelectron spectroscopy

UHV	Ultra high vacuum
UV	Ultra-violett
UV-vis	Ultra-violett and visible
VBE	Vertical binding energy
VDE	Vertical detachment energy
XA	X-ray absorption
XAS	X-ray absorption spectroscopy
XPS	X-ray photoelectron spectroscopy
XUV	Extreme ultra-violett

References

[1] M. Vedamuthu, S. Singh, and G. W. Robinson. Properties of Liquid Water: Origin of the Density Anomalies. *The Journal of Physical Chemistry*, 98(9):2222 – 2230, 1994.

[2] H. Tanaka. Simple Physical Explanation of the Unusual Thermodynamic Behavior of Liquid Water. *Phys. Rev. Lett.*, 80:5750 – 5753, Jun 1998.

[3] C. von Sonntag. *The chemical basis of radiation biology.* London [u.a.] : Taylor & Francis, 1987.

[4] E. Alizadeh and L. Sanche. Precursors of Solvated Electrons in Radiobiological Physics and Chemistry. *Chem. Rev.*, 112:5578 – 5602, 2012.

[5] H. Schüssler, S. Navaratnam, and L. Distel. Rate constants for the reactions of DNA with hydrated electrons and with OH radicals. *Radiat. Phys. Chem.*, 73:163–168, 2005.

[6] B. Boudaïffa, P. Cloutier, D. Hunting, M. A. Huels, and L Sanche. Resonant Formation of DNA Strand Breaks by Low-Energy (3 to 20 eV) Electrons. *Science*, 287:1658, 2000.

[7] J. Berdy, I. Anusiewicz, P. Skurski, and J. Simons. Damage to Model DNA Fragments from Very Low-Energy (<1 eV) Electrons. *J. Am. Chem. Soc.*, 126:6441, 2004.

[8] J. Simons. How Do Low-Energy (0.1-2 eV) Electrons Cause DNA-Strand Breaks? *Acc. Chem. Res.*, 39:772 – 779, 2006.

[9] A. J. Swallow. Hydrated electrons in seawater. *Nature*, 222:369–370, 1969.

[10] L. Turi and P. J. Rossky. Theoretical Studies of Spectroscopy and Dynamics of Hydrated Electrons. *Chem. Rev.*, 112:5641 – 5674, 2012.

[11] M. Blandamer and M. Fox. Theory and applications of charge-transfer-to-solvent spectra. *Chem. Rev.*, 70:59–93, 1970.

[12] X. Chen and S. E. Bradforth. The Ultrafast Dynamics of Photodetachment. *Ann. Rev. Phys. Chem.*, 59:203–231, 2008.

[13] Y.-I. Suzuki, H. Shen, Y. Tang, N. Kurahashi, K. Sekiguchi, T. Mizunoc, and T. Suzuki. Isotope effect on ultrafast charge-transfer-to-solvent reaction from I^- to water in aqueous NaI solution. *Chem. Sci.*, 2:1094, 2011.

[14] A. Lübcke, F. Buchner, N. Heine, I. V. Hertel, and T. Schultz. Time-resolved photoelectron spectroscopy of solvated electrons in aqueous NaI solution. *Phys. Chem. Chem. Phys.*, 12:14629–14634, 2010.

[15] F. Buchner, T. Schultz, and A. Lübcke. Solvated electrons at the water/air interface: Surface versus bulk signal in low kinetic energy photoelectron spectroscopy. *Phys. Chem. Chem. Phys.*, 14:5837 – 5842, 2012.

[16] H. Iglev, A. Trifonov, A. Thaller, I. Buchvarov, T. Fiebig, and A. Laubereau. Photoionization dynamics of an aqueous iodide solution: the temperature dependence. *Chem. Phys. Lett.*, 403:198 – 204, 2005.

[17] L. Kevan. Forbitten matrix proton spin-flip satillites in 70-GHz ESR-spectra of solvated electrons - geometrical model for the solvated electron in methanol glass. *Chem. Phys. Lett.*, 66:578 – 580, 1979.

[18] L. Kevan. Solvated Electron Structure in Glassy Matrices. *Acc. Chem. Res.*, 14:138 – 145, 1981.

[19] J. Schnitker and P. J. Rossky. Quantum simulation study of the hydrated electron. *J. Chem Phys.*, 86:3471, 1987.

[20] D. M. Bartels. Moment analysis of hydrated electron cluster spectra: Surface or internal states? *J. Chem Phys.*, 115:4404, 2001.

[21] L. Turi and D. Borgis. Analytical investigations of an electron-water molecule pseudopotential: II. Development of a new pair potential and molecular dynamics simulations. *J. Chem. Phys.*, 117:6186, 2002.

[22] L. D. Jacobson, C. F. Williams, and J. M. Herbert. The static-exchange electron-water pseudopotential, in conjunction with a polarizable water model: A new Hamiltonian for hydrated-electron simulations. *J. Chem Phys.*, 130:124115, 2009.

[23] R. M. Young and D. M. Neumark. Dynamics of Solvated Electrons in Clusters. *Chem. Rev.*, 112:5553 – 5577, 2012.

[24] Sir H. Davy. *Laboratory Notebook*. Royal Institution, London, 1808.

[25] W. Weyl. *Pogg. Ann.*, 121:601, 1864.

[26] G. Johnstone Stoney. On the physical units of nature. *Phil. Mag. (Ser. 5)*, 11:381, 1881.

[27] J. J. Thomson. Cathode rays. *Phil Mag. (Ser. 5)*, 44:293, 1897.

[28] C. A. Kraus. Solutions of metals in non-metallic solvents; IV. Material effects accompanying the passage of an electrical current through solutions of metals in liquid ammonia. Migration experiments. *J. Am. Chem. Soc.*, 30:1323–1344, 1908.

[29] C. A. Kraus and W. W. Lucasse. The conductance of concentrated solutios of sodium and potassium in liquid ammonia. *J. Am. Chem. Soc.*, 43:2529–2539, 1921.

[30] G. Stein. Some aspects of the radiation chemistry of organic solutes. *Disc. Faraday Soc.*, 12:227, 1952.

[31] E. J. Hart and J. W. Boag. Absorption Spectrum of the Hydrated Electron in Water and in Aqueous Solutions. *J. Am. Chem. Soc.*, 84:4090–4095, 1962.

[32] J. W. Boag and E. J. Hart. Absorption spectra in irradiated water and some solutions. *Nature*, 197:45 – 47, 1963.

[33] T. Ito, S. C. Baker, C. D. Stickley, J. G. Peak, and M. J. Peak. Dependence of the Yield of Strand Breaks Induced by γ-rays in DNA on the Physical Conditions of Exposure: Water Content and Temperature. *J. Int. J. Radiat. Biol.*, 63:289, 1993.

[34] C.-R. Wang, J. Nguyen, and Q.-B. Lu. Bond Breaks of Nucleotides by Dissociative Electron Transfer of Nonequilibrium Prehydrated Electrons: A New Molecular Mechanism for Reductive DNA Damage. *J. Am. Chem. Soc.*, 131:11320 – 11322, 2009.

[35] F. Arnold. Solvated electrons in the upper atmosphere. *Nature*, 294:732 – 733, 1981.

[36] J. V Coe, G.H. Lee, J. G. Eaton, S. T. Arnold, H. W. Sarkas, K. H. Bowen, C. Ludewigt, H. Haberland, and D. R. Worsnop. Photoelectron-spectroscopy of hydrared electron cluster anions, $(H_2O)_{N=2-69}$. *J. Chem. Phys.*, 92:3980 – 3982, 1990.

[37] J. R. R. Verlet, A. E. Bragg, A. Kammrath, O. Cheshnovsky, and D. M. Neumark. Observation of Large Water-Cluster Anions with Surface-Bound Excess Electrons. *Science*, 307:93 – 96, 2005.

[38] J. V. Coe, S. M. Williams, M. Shaun, and K. H. Bowen. Photoelectron spectra of hydrated electron clusters vs. cluster size: connecting to bulk. *Int. Rev. Phys. Chem.*, 27:27 – 51, 2008.

[39] L. Ma, K. Majer, F. Chirot, and B. von Issendorff. Low temperature photoelectron spectra of water cluster anions. *The Journal of Chemical Physics*, 131(14):–, 2009.

[40] R. M. Young, M. A. Yandell, S. B. King, and D. M. Neumark. Thermal effects on energetics and dynamics in water cluster anions $(H_2O)_n^-$. *The Journal of Chemical Physics*, 136(9):–, 2012.

[41] F. Uhlig, O. Marsalek, and P. Jungwirth. Electron at the Surface of Water: Dehydrated or Not? *J. Phys. Chem. Lett.*, 4 (2):338 – 343, 2013.

[42] O. Marsalek, F. Uhlig, J. VandeVondele, and P. Jungwirth. Structure, Dynamics, and Reactivity of Hydrated Electrons by Ab Initio Molecular Dynamics. *Accounts of Chemical Research*, 45(1):23 – 32, 2012. PMID: 21899274.

[43] K. R. Siefermann, Y. Liu, E. Lugovoy, O. Link, M. Faubel, U. Buck, B. Winter, and B. Abel. Binding energies, lifetimes and implications of bulk and interface solvated electrons in water. *Nat. Chem.*, 2:274 – 279, April 2010.

[44] Y. Tang, H. Shen, K. Sekiguchi, N. Kurahashi, T. Mizuno, Y.-I. Suzuki, and T. Suzuki. Direct measurement of vertical binding energy of a hydrated electron. *Phys. Chem. Chem. Phys.*, 12:3653–3655, 2010.

[45] A. T. Shreve, T. A. Yen, and D. M. Neumark. Photoelectron spectroscopy of hydrated electrons. *Chem. Phys. Lett.*, 493:216 – 219, 2010.

[46] T. Suzuki. Time-resolved photoelectron spectroscopy of non-adiabatic electronic dynamics in gas and liquid phases. *Int. Rev. Phys. Chem.*, 31:265 – 318, 2012.

[47] Jun Kim, Israela Becker, Ori Cheshnovsky, and Mark A. Johnson. Photoelectron spectroscopy of the missing hydrated electron clusters $(h_2o)_n^-$, n=3, 5, 8 and 9: Isomers and continuity with the dominant clusters n=6, 7 and 11. *Chem. Phys. Lett.*, 297:90 – 96, 1998.

[48] Y.-I. Yamamoto, Y.-I. Suzuki, G. Tomasello, T. Horio, S. Karashima, R. Mitríc, and T. Suzuki. Time- and Angle-Resolved Photoemission Spectroscopy of Hydrated Electrons Near a Liquid Water Surface. *Phys. Rev. Lett.*, 112:187603, 2014.

[49] I. G. Draganic and Z. D. Draganic. *The Radiation Chemistry of Water*. Academic Press, New York, 1971.

[50] Farhataziz and A. J. Rodgers, editors. *Radiation Chemistry, Principles and Applications*. VCH Verlagsgesellschaft mbH, Weinheim, 1987.

[51] D. M. Bartels, A. R. Cook, M. Mudaliar, and C. D. Jonah. Spur Decay of the Solvated Electron in Picosecond Radiolysis Measured with Time-Correlated Absorption Spectroscopy. *The Journal of Physical Chemistry A*, 104(8):1686–1691, 2000.

[52] B. Winter, R. Weber, W. Widdra, M. Dittmar, M. Faubel, and I. V. Hertel. Full Valence Band Photoemission from Liquid Water Using EUV Synchrotron Radiation. *J. Phys. Chem. A*, 108:2625 – 2632, 2004.

[53] A Hertwig, H Hippler, A. N. Untereiner, and P. Vohringer. Ultrafast relaxation dynamics of solvated electrons in water. *Ber. Bunsenges.*, 102:805–810, 1988.

[54] C. L. Thomsen, D. Madsen, S. R. Keiding, J. Thogersen, and O. Christiansen. Two-photon dissociation and ionization of liquid water studied by femtosecond transient absorption spectroscopy. *J. Chem Phys.*, 110:3453–3453, 1999.

[55] R. Laenen, T. Roth, and A. Laubereau. Novel Precursors of Solvated Electrons in Water: Evidence for a Charge Transfer Process. *Phys. Rev. Lett.*, 85:50–53, 2000.

[56] D. H. Son, P. Kambhampati, T. W. Kee, and P. F. Barbara. Delocalizing Electrons in Water with Light. *J. Phys. Chem. A*, 105:8269 – 8272, 2001.

[57] R. A. Crowell and D. M. Bartels. Multiphoton Ionization of Liquid Water with 3.0 - 5.0 eV Photons. *The Journal of Physical Chemistry*, 100(45):17940–17949, 1996.

[58] T. W. Kee, D. Hee Son, P. Kambhampati, and P. F. Barbara. A Unified Electron Transfer Model for the Different Precursors and Excited States of the Hydrated Electron. *J. Phys. Chem. A*, 105:8434–8439, 2001.

[59] C. G. Elles, A. E. Jailaubekov, R. A. Crowell, and S. E. Bradforth. Excitation-energy dependence of the mechanism for two-photon ionization of liquid H_2O and D_2O from 8.3 to 12.4 eV. *J. Chem. Phys.*, 125:044515, 2006.

[60] M. F. Fox and E. Hayon. Far UV spectroscopy of the iodide ion. *J. Chem. Soc. Faraday Trans. 1*, 73:1003 – 1016, 1977.

[61] Y. Tang, Y.-I. Suzuki, H. Shen, K. Sekiguchi, N. Kurahashi, K. Nishizawa, P. Zuo, and T. Suzuki. Time-resolved photoelectron spectroscopy of bulk liquids at ultra-low kinetic energy. *Chem. Phys. Lett.*, 494:111 – 116, 2010.

[62] R. Seidel, S. Thümer, J. Moens, P. Geerlings, J. Blumberger, and B. Winter. Valence Photoemission Spectra of Aqueous $Fe^{2+/3+}$ and $[Fe(CN)_6]^{4+/3+}$ and Their Interpretation by DFT Calculations. *The Journal of Physical Chemistry B*, 115(40):11671–11677, 2011. PMID: 21809848.

[63] N. Kurahashi, S. Karashima, Y. Tang, T. Horio, R. Abulimiti, Y.-I. Suzuki, Y. Ogi, M. Oura, and T. Suzuki. Photoelectron spectroscopy of aqueous solutions: Streaming potentials of NaX (X = Cl, Br, and I) solutions and electron binding energies of liquid water and X. *J. Chem. Phys.*, 140(17):174506, 2014.

[64] M. Smith and M. C. R. Symons. Solvation spectra. Part 1.-The effect of environmental changes upon the ultra-violet absorption of solvated iodide ions. *Trans. Faraday Soc.*, 54:338–345, 1958.

[65] W. S. Sheu and P. J. Rossky. Charge-transfer-to-solvent spectra of an aqueous halide revisited via computer simulation. *J. Am. Chem. Soc.*, 115:7729–7735, 1993.

[66] C. M. Moore. *Atomic energy levels : as derived from the analyses of optical spectra. 3. The spectra of molybdenum, technetium, ruthenium, rhodium, palladium, silver, cadmium, indium, tin, antimony, tellurium, iodine, xenon, cesium, barium, lanthanum-hafnium, tantalum, tungsten, rhenium, osmium, iridium, platinum, gold, mercury, thallium, lead, bismuth, polonium, radon, radium, and actinium.* Washington, DC : U.S. Gov. Print. Off., 1971.

[67] R. Lian, D. A. Oulianov, R. A. Crowell, I. A. Shkrob, X. Chen, and S. E. Bradforth. Electron Photodetachment from Aqueous Anions. 3. Dynamics of Geminate Pairs Derived from Photoexcitation of Mono- vs Polyatomic Anions. *J. Phys. Chem. A*, 110:9071 – 9078, 2006.

[68] V. H. Vilchiz, J. A. Kloepfer, A. C. Germaine, V. A. Lenchenkov, and S. E. Bradforth. Map for the Relaxation Dynamics of Hot Photoelectrons Injected into Liquid Water via Anion Threshold Photodetachment and above Threshold Solvent Ionization. *J. Phys. Chem. A*, 105:1711 – 1723, 2001.

[69] F. Buchner, A. Lübcke, N. Heine, and T. Schultz. Time-resolved photoelectron spectroscopy of liquids. *Rev. Sci. Instrum.*, 81:113107, 2010.

[70] J. A. Kloepfer, V. H. Vilchiz, V. A. Lenchenkov, and S. E. Bradforth. *Molecular mechanisms for photodetachment in water. In Ultrafast Phenomena XIII.* Berlin:Springer Verlag, 2003.

[71] J. A. Kloepfer, V. H. Vilchiz, V. A. Lenchenkov, A. C. Germaine, and S. E. Bradforth. The ejection distribution of solvated electrons generated by the one-photon photodetachment of aqueous I^- and two-photon ionization of the solvent. *J. Chem. Phys.*, 113:6288, 2000.

[72] F. Messina, O. Bräm, A. Cannizzo, and M. Chergui. Real-time observation of the charge transfer to solvent dynamics. *Nat. Commun.*, 4:2119, 2013.

[73] A. Cannizzo, O. Bräm, G. Zgrablic, A. Tortschanoff, A. Ajdarzadeh Oskouei, F. van Mourik, and M. Chergui. Femtosecond fluorescence upconversion setup with broadband detection in the ultraviolet. *Opt. Lett.*, 32:3555 – 3557, 2007.

[74] M. C. Larsen and B. J. Schwartz. Searching for solvent cavities via electron photodetachment: The ultrafast charge-transfer-to-solvent dynamics of sodide in a series of ether solvents. *The Journal of Chemical Physics*, 131(15):154506, 2009.

[75] J. A Kloepfer, V. H Vilchiz, V. A Lenchenkov, and S. E Bradforth. Femtosecond dynamics of photodetachment of the iodide anion in solution: resonant excitation into the charge-transfer-to-solvent state. *Chem. Phys. Lett.*, 298:120 – 128, 1998.

[76] W. C. Gottschall and E. J. Hart. The effect of temperature on the absorption spectrum of the hydrated electron and on its bimolecular recombination reaction. *The Journal of Physical Chemistry*, 71(7):2102 – 2106, 1967.

[77] K. Yokoyama, C. Silva, D. H. Son, P. K. Walhout, and P. F. Barbara. Detailed Investigation of the Femtosecond Pump-Probe Spectroscopy of the Hydrated Electron. *J. Phys. Chem. A*, 102:6957–6966, 1998.

[78] M Assel, R Laenen, and A Laubereau. Femtosecond solvation dynamics of solvated electrons in neat water. *Chem. Phys. Lett.*, 317:13 – 22, 2000.

[79] M. S. Pshenichnikov, A. Baltuska, and D. A. Wiersma. Hydrated-electron population dynamics. *Chem. Phys. Lett.*, 389:171 – 175, 2004.

[80] M H. Elkins, H. L. Williams, A. T. Shreve, and D. M. Neumark. Relaxation Mechanism of the Hydrated Electron. *Science*, 342:1496 – 1499, 2013.

[81] H. Hertz. Über einen Einfluss des ultravioletten Lichtes auf die elektrische Entladung. *Ann. Physik*, 31:983, 1887.

[82] A. Einstein. Über einen die Erzeugung und Verwandlung des Lichtes betreffenden heuristischen Gesichtspunkt. *Annalen der Physik*, 17:132, 1905.

[83] H. P. Bartel and C. Kleint. On the history of photoemission. *Prog. Surf. Sci.*, 48:179, 1995.

[84] E. Aziz, N. Ottosson, S. Bonhommeau, N. Bergmann, W. Eberhardt, and M. Chergui. Probing the Electronic Structure of the Hemoglobin Active Center in Physiological Solutions. *Phys. Rev. Lett.*, 102:068103, Feb 2009.

[85] A. Knop, H. W. Jochims, A. L. D. Kilcoyne, A. D. Hitchcock, and E. Rühl. Zero-kinetic-energy photoelectron spectroscopy of Ar(2p)-excited argon clusters. *Chem. Phys. Lett.*, 223:553 – 560, July 1994.

[86] J.J. Yeh and I. Lindau. Atomic subshell photoionization cross sections and asymmetry parameters: $1 \leq Z \leq 103$. *Atomic Data and Nuclear Data Tables*, 32(1):1 – 155, 1985.

[87] V. Schmidt. *Electron Spectrometry of Atoms using Synchrotron Radiation*. Cambridge University Press, 1997.

[88] S. Hüfner. *Photoelectron Spectroscopy: Principles and Applications*. Springer-Verlag Berlin Heidelberg New York, 2003.

[89] A. A. Kordyuk. ARPES experiment in fermiology of quasi-2D metals (Review Article). *Low Temperature Physics*, 40(4):286 – 296, 2014.

[90] K. L. Reid. Photoelectron Angular Distributions. *Annual Review of Physical Chemistry*, 54(1):397 – 424, 2003. PMID: 12574491.

[91] J. Cooper and R. N. Zare. Angular Distribution of Photoelectrons. *J. Chem. Phys.*, 48:942 – 943, 1968.

[92] E. W. Plummer and W. Eberhardt. *Angle-Resolved Photoemission as a Tool for the Study of Surfaces*, pages 533 – 656. John Wiley & Sons, Inc., 2007.

[93] J. G. Underwood and K. L. Reid. Time-resolved photoelectron angular distributions as a probe of intramolecular dynamics: Connecting the molecular frame and the laboratory frame. *The Journal of Chemical Physics*, 113(3):1067 – 1074, 2000.

[94] H. Lüth. *Surfaces and Interfaces of Solid Materials*. Springer Berlin Heidelberg, 1997.

[95] B. Winter and M. Faubel. Photoemission from Liquid Aqueous Solutions. *Chem. Rev.*, 106:1176–1211, 2006.

[96] R. Wierl. *Verh. d. D. Phys. Ges.*, 11:29, 1930.

[97] H. Siegbahn and K. Siegbahn. ESCA applied to liquids. *J. Electron Spectrosc. Rel. Phenom.*, 2:319–325, 1973.

[98] H. Siegbahn. Electron spectroscopy for chemical analysis of liquids and solutions. *J. Phys. Chem.*, 89:898, 1985.

[99] M. Faubel, S. Schlemmer, and J. P. Toennies. A molecular beam study of the evaporation of water from a liquid jet. *Atoms, Molecules and Clusters*, 10:269–277, 1988.

[100] M. Faubel and Th. Kisters. Non-equilibrium molecular evaporation of carboxylic acid dimers. *Nature*, 339:527, 1989.

[101] M. Faubel, B. Steiner, and J. P. Toennies. Photoelectron spectroscopy of liquid water, some alcohols, and pure nonane in free micro jets. *J. Chem. Phys.*, 106:9013 – 9031, June 1997.

[102] M. Faubel, B. Steiner, and J. P. Toennies. Measurement of He I photoelectron spectra of liquid water, formamide and ethylene glycol in fast-flowing microjets. *J. Electron Spectrosc. Rel. Phenom.*, 95:159–169, 1998.

[103] B. Winter. Liquid microjet for photoelectron spectroscopy. *Nucl. Instrum. Methods Phys. Res. Sect. A*, 601:139 – 150, 2009.

[104] K. M. Lange, R. Könnecke, S. Ghadimi, R. Golnak, M. A. Soldatov, K. F. Hodeck, A. Soldatov, and E. F. Aziz. High resolution X-ray emission spectroscopy of water and aqueous ions using the micro-jet technique. *Chemical Physics*, 377:1 – 5, 2010.

[105] C. A. Arrell, J. Ojeda, M. Sabbar, W. A. Okell, T. Witting, T. Siegel, Z. Diveki, S. Hutchinson, L. Gallmann, U. Keller, F. van Mourik, R. T. Chapman, C. Cacho, N. Rodrigues, I. C.E. Turcu, J. W.G. Tisch, E. Springate, J. P. Marangos, and M. Chergui. A simple electron time-o–flight spectrometer for ultrafast vacuum ultraviolet photoelectron spectroscopy of liquid solutions. *Review of Scientific Instruments*, 85(10):–, 2014.

[106] S. Schreck, A. Pietzsch, K. Kunnus, B. Kennedy, W. Quevedo, P. S. Miedema, P. Wernet, and A. Föhlisch. Dynamics of the OH group and the electronic structure of liquid alcohols. *Structural Dynamics*, 1(5):–, 2014.

[107] M. Faubel. *Photoionization and Photodetachment, Chapter 12 Photoelectron spectroscopy at liquid surfaces*. World Scientific, 2000.

[108] K. R. Wilson, B. S. Rude, J. Smith, C. Cappa, D. T. Co, R. D. Schaller, M. Larsson, T. Catalano, and R. J. Saykally. Investigation of volatile liquid surfaces by synchrotron x-ray spectroscopy of liquid microjets. *Rev. Sci. Instrum.*, 75:725 – 736, 2004.

[109] S. Thürmer, R. Seidel, M. Faubel, W. Eberhardt, J. C. Hemminger, S. E. Bradforth, and B. Winter. Photoelectron angular distributions from liquid water: Effects of electron scattering. *Phys. Rev. Lett.*, 111:173005, 2013.

[110] K. M. Lange. *Structure and Dynamics of Water and Ions in Solution - Soft X-Ray Absorption and Emission Studies*. PhD thesis, Freie Universität Berlin, 2012.

[111] A. Einstein. On the quantum theory of radiation. *Phys. Z.*, 18:63, 1917.

[112] T. H. Maiman. Stimulated Optical Radiation in Ruby. *Nature*, 187:493–494, 1960.

[113] P. F. Moulton. Spectroscopic and laser characteristics of ti:al_2o_3. *J. Opt. Soc. Am. B*, 3:125–133, 1986.

[114] C. Rulliere, editor. *Femtosecond Laser Pulses - Principles and Experiments*. Springer Science+Business Media, Inc., 2005.

[115] M. Schultze, M. Fieß, N. Karpowicz, J. Gagnon, M. Korbman, M. Hofstetter, S. Neppl, A. L. Cavalieri, Y. Komninos, Th. Mercouris, C. A. Nicolaides, R. Pazourek, S. Nagele, J. Feist, J. Burgdörfer, A. M. Azzeer, R. Ernstorfer, R. Kienberger, U. Kleineberg, E. Goulielmakis, F. Krausz,

and V. S. Yakovlev. Delay in photoemission. *Science*, 328:1658 – 1662, 2010.

[116] K. Klünder, J. M. Dahlstrom, M. Gisselbrecht, T. Fordell, M. Swoboda, D. Guénot, P. Johnsson, J. Caillat, J. Mauritsson, A. Maquet, R. Taïeb, and A. L'Huillier. Probing single-photon ionization on the attosecond time scale. *Phys. Rev. Lett.*, 106:143002, 2011.

[117] L. Gallmann, C. Cirelli, and U. Keller. Attosecond Science: Recent Highlights and Future Trends. *Annu. Rev. Phys. Chem.*, 63:447, 2012.

[118] K. M. Lange, A. Kothe, and E. F. Aziz. Chemistry in solution: recent techniques and applications using soft X-ray spectroscopy. *Phys. Chem. Chem. Phys.*, 14:5331–5338, 2012.

[119] N. Huse, H. Wen, D. Nordlund, E. Szilagyi, D. Daranciang, T. A. Miller, A. Nilsson, R. W. Schoenlein, and A. M. Lindenberg. Probing the hydrogen-bond network of water via time-resolved soft X-ray spectroscopy. *Phys. Chem. Chem. Phys.*, 11:3951 – 3957, 2009.

[120] H. Wen, N. Huse, R. W. Schoenlein, and A. M. Lindenberg. Ultrafast conversions between hydrogen bonded structures in liquid water observed by femtosecond x-ray spectroscopy. *The Journal of Chemical Physics*, 131(23):–, 2009.

[121] G. Gavrila, K. Godehusen, C. Weniger, E.T.J. Nibbering, T. Elsaesser, W. Eberhardt, and P. Wernet. Time-resolved X-ray absorption spectroscopy of infrared-laser-induced temperature jumps in liquid water. *Applied Physics A*, 96(1):11 – 18, 2009.

[122] N. Huse, T. K. Kim, L. Jamula, J. K. McCusker, F. M. F. de Groot, and R. W. Schoenlein. Photo-Induced Spin-State Conversion in Solvated Transition Metal Complexes Probed via Time-Resolved Soft X-ray Spectroscopy. *J. Am. Chem. Soc.*, 132(19):6809–6816, 2010.

[123] N. Huse, H. Cho, K. Hong, L. Jamula, F. M. F. de Groot, T. K. Kim, J. K. McCusker, and R W. Schoenlein. Femtosecond Soft X-ray Spectroscopy of Solvated Transition-Metal Complexes: Deciphering the Interplay of Electronic and Structural Dynamics. *The Journal of Physical Chemistry Letters*, 2(8):880–884, 2011.

[124] F. A. Lima, Christopher J. Milne, D. C. V. Amarasinghe, M. H. Rittmann-Frank, R. M. van der Veen, M. Reinhard, V.-T. Pham, S. Karlsson,

S. L. Johnson, D. Grolimund, C. Borca, T. Huthwelker, M. Janousch, F. van Mourik, R. Abela, and M. Chergui. A high-repetition rate scheme for synchrotron-based picosecond laser pump/x-ray probe experiments on chemical and biological systems in solution. *Rev. Sci. Instrum.*, 82(6):063111, 2011.

[125] M Wilke, R Al-Obaidi, A Moguilevski, A Kothe, N Engel, J Metje, I Yu Kiyan, and E F Aziz. Laser-assisted electron scattering in strong-field ionization of dense water vapor by ultrashort laser pulses. *New Journal of Physics*, 16(8):083032, 2014.

[126] P. Kruit and F. H. Read. Magnetic field paralleliser for 2 πelectron-spectrometer and electron-image magnifier. *J. Phys. E: Sci. Instrum.*, 16:313 – 324, 1983.

[127] A. Kothe, J. Metje, M. Wilke, A. Moguilevski, N. Engel, R. Al-Obaidi, C. Richter, R. Golnak, I. Yu. Kiyan, and E. F. Aziz. Time-of-flight electron spectrometer for a broad range of kinetic energies. *Rev. Sci. Instrum.*, 84:023106, 2013.

[128] Uwe Becker and David A. Shirley. *VUV and soft X-ray photoionization.* Plenum Press, New York, 1996.

[129] P. Lablanquie, L. Andric, J. Palaudoux, U. Becker, M. Braune, J. Viefhaus, J.H.D. Eland, and F. Penent. Multielectron spectroscopy: Auger decays of the argon 2p hole. *J. Electron Spectrosc. Relat. Phenom.*, 156 - 158(0):51 – 57, 2007.

[130] S. Hara and M. Nakamura. Determination of the photoionisation asymmetry parameter. *J. Phys. B: At. Mol. Phys.*, 19:L467 – L469, 1896.

[131] T. Tsuboi, E. Y. Xu, Y. K. Bae, and K. T. Gillen. Magnetic bottle electron spectrometer using permanent magnets. *Rev. Sci. Instrum.*, 59:1357 – 1362, 1988.

[132] R. Weber, B. Winter, P. M. Schmidt, W. Widdra, I. V. Hertel, M. Dittmar, and M. Faubel. Photoemission from Aqueous Alkali-Metal-Iodide Salt Solutions Using EUV Synchrotron Radiation. *J. Phys. Chem. B*, 108:4729–4736, 2004.

[133] A. Kothe, M. Wilke, A. Moguilevski, N. Engel, B. Winter, I. Yu. Kiyan, and E. F. Aziz. Charge Transfer to Solvent Dynamics in Iodide Aqueous Solu-

tion Studied at Ionization Threshold. *Phys. Chem. Chem. Phys.*, 17:1918 – 1924, 2015.

[134] A. Hertwig, H. Hippler, and A.-N. Unterreiner. Transient spectra, formation, and geminate recombination of solvated electrons in pure water UV-photolysis: an alternative view. *Phys. Chem. Chem. Phys.*, 1:5633–5642, 1999.

[135] B. Winter, E. F. Aziz, N. Ottosson, M. Faubel, N. Kosugi, and I. V. Hertel. Electron Dynamics in Charge-Transfer-to-Solvent States of Aqueous Chloride Revealed by Cl^- 2p Resonant Auger-Electron Spectroscopy. *J. Am. Chem. Soc.*, 130(22):7130–7138, 2008.

[136] R. Seidel, S. Thümer, and B. Winter. Photoelectron Spectroscopy Meets Aqueous Solution: Studies from a Vacuum Liquid Microjet. *J. Phys. Chem. Lett.*, 2:633 – 641, 2011.

[137] J. A. Nelder and R. Mead. A simplex method for function minimization. *Computer Journal*, 7:308 – 313, 1965.

[138] L. M. Chanin, A. V. Phelps, and M. A Biondi. Measurements of the Attachment of Low-Energy Electrons to Oxygen Molecules. *Phys. Rev.*, 128:219 – 230, 1962.

[139] F. H. Long, H. Lu, X. Shi, and K. B. Eisenthal. Femtosecond studies of electron photodetachment from an iodide ion in solution: The trapped electron. *Chem. Phys. Lett.*, 169(3):165 – 171, 1990.

[140] R. Follath and F. Senf. New plane-grating monochromators for third generation synchrotron radiation light sources. *Nuclear Instruments and Methods in Physics Research Section A: Accelerators, Spectrometers, Detectors and Associated Equipment*, 390(3):388 – 394, 1997.

[141] M.R. Weiss, R. Follath, F. Senf, and W. Gudat. Comparative monochromator studies for a soft x-ray microfocus beamline for BESSY-II. *Journal of Electron Spectroscopy and Related Phenomena*, 101 - 103(0):1003 – 1012, 1999.

[142] A. Thompson, I. Lindau, D. Attwood, Y. Liu, E. Gullikson, P. Pianetta, M. Howells, A. Robinson, K.-J. Kim, J. Scofield, J. Kirz, J. Underwood, J. Kortright, G. Williams, and H. Winick. X-ray data booklet. Lawrence Berkley National Laboratory, University of Claifornia, Berkley, CA 94720, 2009.

[143] A. A. Zholents and M. S. Zolotorev. Femtosecond X-Ray Pulses of Synchrotron Radiation. *Phys. Rev. Lett.*, 76:912–915, Feb 1996.

[144] R. W. Schoenlein, W. P. Leemans, A. H. Chin, P. Volfbeyn, T. E. Glover, P. Balling, M. Zolotorev, K.-J. Kim, S. Chattopadhyay, and C. V. Shank. Femtosecond X-ray Pulses at 0.4 $\AA$ Generated by 90° Thomson Scattering: A Tool for Probing the Structural Dynamics of Materials. *Science*, 274(5285):236–238, 1996.

[145] R. W. Schoenlein, S. Chattopadhyay, H. H. W. Chong, T. E. Glover, P. A. Heimann, C. V. Shank, A. A. Zholents, and M. S. Zolotorev. Generation of Femtosecond Pulses of Synchrotron Radiation. *Science*, 287(5461):2237–2240, 2000.

[146] S. Khan, K. Holldack, T. Kachel, R. Mitzner, and T. Quast. Femtosecond Undulator Radiation from Sliced Electron Bunches. *Phys. Rev. Lett.*, 97:074801, Aug 2006.

[147] K. Holldack, J. Bahrdt, A. Balzer, U. Bovensiepen, M. Brzhezinskaya, A. Erko, A. Eschenlohr, R. Follath, A. Firsov, W. Frentrup, L. Le Guyader, T. Kachel, P. Kuske, R. Mitzner, R. Müller, N. Pontius, T. Quast, I. Radu, J.-S. Schmidt, C. Schüßler-Langeheine, M. Sperling, C. Stamm, C. Trabant, and A. Föhlisch. FemtoSpeX: a versatile optical pump–soft X-ray probe facility with 100fs X-ray pulses of variable polarization. *Journal of Synchrotron Radiation*, 21(5):1090–1104, Sep 2014.

[148] A. Cannizzo, C.J. Milne, C. Consani, W. Gawelda, Ch. Bressler, F. van Mourik, and M. Chergui. Light-induced spin crossover in Fe(II)-based complexes: The full photocycle unraveled by ultrafast optical and X-ray spectroscopies. *Coordination Chemistry Reviews*, 254:2677 – 2686, 2010. 18th International Symposium on the Photochemistry and Photophysics of Coordination Compounds Sapporo, 2009.

[149] H. T. Lemke, C. Bressler, L. X. Chen, D. M. Fritz, K. J. Gaffney, A. Galler, W. Gawelda, K. Haldrup, R. W. Hartsock, H. Ihee, J. Kim, K. H. Kim, J. H. Lee, M. M. Nielsen, A. B. Stickrath, W. Zhang, D. Zhu, and M. Cammarata. Femtosecond X-ray Absorption Spectroscopy at a Hard X-ray Free Electron Laser: Application to Spin Crossover Dynamics. *The Journal of Physical Chemistry A*, 117(4):735–740, 2013.

[150] J. Metje, M. Borgwardt, A. Moguilevski, A. Kothe, N. Engel, M. Wilke, R. Al-Obaidi, D. Tolksdorf, A. Firsov, M. Brzhezinskaya, A. Erko, I. Yu.

Kiyan, and E. F. Aziz. Monochromatization of femtosecond XUV light pulses with the use of reflection zone plates. *Opt. Express*, 22(9):10747–10760, May 2014.

[151] V. V. Aristov, A. I. Erko, and V. V. Martynov. Principles of Bragg-Fresnel multilayer optics. *Revue Phys. Appl.*, 23:1623 – 1630, 1988.

[152] V. V. Aristov, S. V. Gaponov, V. M. Genkin, Yu. A. Goratov, A. I. Erko, V. V. Martynov, L. A. Matveev, N. N. Salashchenko, and A. A. Fraerman. Focusing properties of shaped multilayer mirrors. *J. Exp. Theor. Phys.*, 44:265 – 267, 1986.

Abstract

This thesis explores the early-time electronic relaxation in sodium iodide aqueous solution exposed to a femtosecond ultra-violet laser pulse. Rather than initiating the charge transfer reaction by resonant one-photon photoexcitation of iodide, in the present time-resolved photoelectron spectroscopy study the charge-transfer-to-solvent (CTTS) states are populated via electronic excitation above the vacuum level. This is accomplished via a two-photon process using 266 nm (4.65 eV) laser pulses with a pulse duration of 60 fs. By analyzing the temporal evolution of electron yields from ionization of two transient species, assigned to CTTS and its first excited state, both their ultrafast population and relaxation dynamics were determined. For ionization a femtosecond laser probe photon of 3.55 eV photon energy is used. Comparison with resonant one-photon excitation studies shows that the highly excited initial states populated in the present wotk exhibit similar relaxation characteristics. Implications for structure and dynamical response of the solvation cage are discussed.

The measurements were conducted using a newly constructed experimental setup and time-of-flight electron spectrometer of the magnetic bottle type. The spectrometer was designed to measure the energy spectra of electrons generated from liquids excited by a strong laser field as well as by photons in the range from ultra-violet to soft X-rays. Its energy resolution $\Delta E/E$ is approximately 0.016 at kinetic energies of 100 eV. The collection efficiency of the spectrometer is determined for different kinetic energies, and the values are discussed for the magnetic-bottle configuration and the field-free arrangement. Implementation of the recycle microjet technique offers uninterupted measurement condition over several hours, which is advantageous for time-resolved studies on diluted systems, and the possibility of recycling expensive or rare sample.

Kurzzusammenfassung

In der vorliegenden Doktorarbeit wird die elektronische Relaxation in wässriger Natriumiodidlösung untersucht, die nach der Bestrahlung von ultravioletten, wenige Femtosekunden kurzen Laserpulsen auftritt. Die Ladungsaustauschreaktionen werden hierbei nicht durch eine resonante Ein-Photonen-Anregung des Iodid-Anions initiiert; stattdessen werden die sogenannten Charge-Transfer-To-Solvent (CTTS) Zustände durch eine elektronische Anregung oberhalb des Vakuumniveaus besetzt. Dies geschieht mittels eines Zwei-Photonen-Prozesses, bei dem die Laserpulse eine Photonenenergie von 4.65 eV und eine Pulsdauer von 60 Femtosekunden aufweisen. Aus der Analyse der zeitlichen Entwicklung des Photoelektronensignals lassen sich zwei kurzlebige Zustände bestimmen, die dem CTTS und dessen ersten angeregten Zustand zugeordnet werden. Sowohl die ultraschnelle Besetzungs- als auch deren Relaxationsdynamik wurde ausführlich untersucht. Die Ionisation erfolgt mit Hilfe eines zweiten Femtosekunden-Laserpulses, der eine Photonenenergie von 3.55 eV aufweist. Vergleiche der hier untersuchten hoch-angeregten Erstzustände mit Arbeiten, die auf resonanter Ein-Photonen-Anregung basieren, zeigen ähnliche Relaxationscharakteristika. Die Auswirkungen auf die dynamischen Reaktionsprozesse in der ersten Solvatschale sowie deren Struktur werden diskutiert.

Die Messungen wurden mit einer neu konstruierten Experimentierkammer und einem Elektronen-Flugzeit-Spektrometer mit magnetischer Flasche durchgeführt. Das Spektrometer wurde speziell für die Detektion von Elektronen entwickelt, die aus einer Flüssigkeitsprobe mittels verschiedener Lichtquellen (UV bis weiche Röntgenstrahlung) generiert werden und einen weiten kinetischen Energiebereich abdecken. Die Energieauflösung $\Delta E/E$ beträgt für Elektronen mit einer kinetischen Energie von 100 eV ungefähr 0.016. Die Elektronenausbeute-Effizienz des Spektrometers wurde für verschiedene kinetische Energien bestimmt und die hierbei ermittelten Werte wurden für die Nutzung der magnetischen Flasche sowie für die feldfreie Konfiguration diskutiert. Der Einbau eines "Recycle Mikrojets" ermöglicht die kontinuierliche Messung eines Flüssigkeitsstrahls aus einer einzigen Probenlösung über mehrere Stunden hinweg. Dies ist insbesondere im Hinblick auf die zeitaufgelöste Untersuchung von Flüssigkeiten wichtig, bei der nur eine geringe Menge vorgehalten werden kann.

List of Publications

Parts of this thesis have been published in the following articles:

Charge Transfer to Solvent Dynamics in Iodide Aqueous Solution Studied at Ionization Threshold, A. Kothe and M. Wilke and A. Moguilevski and N. Engel and B. Winter and I. Yu. Kiyan and E. F. Aziz, Phys. Chem. Chem. Phys. 17, 1918-1924 (2015)

Time-of-flight electron spectrometer for a broad range of kinetic energies, A. Kothe and J. Metje and M. Wilke and A. Moguilevski and N. Engel and R. Al-Obaidi and C. Richter and R. Golnak and I. Yu. Kiyan and E. F. Aziz, Rev. Sci. Instrum. 84, 023106 (2013)

Chemistry in solution: recent techniques and applications using soft X-ray spectroscopy, K. M. Lange and A. Kothe and E. F. Aziz, Phys. Chem. Chem. Phys. 14, 5331-5338 (2012)

During my time as a PhD student I contributed to the following publications:

Laser-assisted electron scattering in strong-field ionization of dense water vapor by ultrashort laser pulses, M. Wilke, R. Al-Obaidi, A. Moguilevski, A. Kothe, N. Engel, J. Metje, I. Yu. Kiyan, E. F. Aziz, New J. Phys. 16, 083032 (2014)

Monochromatization of femtosecond XUV light pulses with the use of reflection zone plates, J. Metje, M. Borgwardt, A. Moguilevski, A. Kothe, N. Engel, M. Wilke, R. Al-Obaidi, D. Tolksdorf, A. Firsov, M. Brzhezinskaya, A. Erko, I. Yu. Kiyan, E. F. Aziz, Opt. Expess 22, 10747-10760 (2014)

Chemical Bonding in Aqueous Ferrocyanide: Experimental and Theoretical X-ray Spectroscopic Study, N. Engel, S. I. Bokarev, E. Suljoti, R. Garcia-Diez, K. M. Lange, K. Atak, R. Golnak, A. Kothe, M. Dantz, O. Kühn, E. F. Aziz, J. Phys. Chem. B 118 (6), 1555-1563 (2014)

On the Origin of Dips in Total Fluorescence Yield X-Ray Absorption Spectra: Partial and Inverse Partial Fluorescence Yield at the L-edge of Cobalt aqueous Solution, M. A. Soldatov, K. M. Lange, M. D. Gotz, N. Engel, R. Golnak, A. Kothe, E. F. Aziz, Chem. Phys. Lett. 546, 164-167 (2012)

Origin of Dark-Channel X-ray Fluorescence from Transition-Metal Ions in Water, R. Seidel, S. Ghadimi, K. M. Lange, S. Bonhommeau, M. A. Soldatov, R. Golnak, A. Kothe, R. Könnecke, A. Soldatov, S. Thürmer, B. Winter, and E. F. Aziz, J. Am. Chem. Soc. 134 (3), 1600-1605 (2012)

Breathing Volume into Interfacial Water with Laser Light, A. P. Sommer, K. F. Hodeck, D. Zhu, A. Kothe, K. M. Lange, H.-J. Fecht, E. F. Aziz, J. Phys. Chem. Lett. 2 (6), 562-565 (2011)

Ich versichere, dass ich diese Arbeit selbständig verfasst und keine anderen als die angegebenen Quellen und Hilfsmittel verwendet habe. Der Inhalt dieser Arbeit ist nicht schon einmal in einem früheren Promotionsverfahren eingereicht worden.

Berlin, den 17.12.2014

Alexander Kothe

Acknowledgements

Firstly, I would like to thank my supervisor Prof. Emad Aziz for giving me the opportunity to write my doctoral thesis in his group. During my whole PhD, he was always accessible, closely involed and shared his expertise, even when the group started to grow significantly. His "We´ll make it happen" attitude was very motivating, especially when sudden obsticales emerged.

I thank Prof. Wolfgang Kuch from Freie Universität Berlin for being the second reviewer of my thesis. I very much enjoyed presenting my work in his seminar, where I was amazed by the interest of his group in my experiments.

I want to thank Dr. Igor Kiyan for supervising my PhD thesis. His experience and attention to detail in the experimental experiments and the interpretation of our results was always helpful.

I am greatful for the opportunity to work with Dr. Bernd Winter. His outstanding scientific knowledge in the framework of liquid spectroscopy is the foundation of the interpretation of the findings presented for the NaI aqueous solution.

Very special thanks to Martin Wilke, who supported me in the experiments investigating the ultrafast dynamics in the NaI aqueous solution as well as in the characterization of the spectrometer and the data analysis.

I could not have done the experiments without the support of Alexandre Moguilevski, who always kept the laser and optics in good shape.

I also thank Nicholas Engel for his continued support in many beamtimes. He often stayed until the next morning to finish measurements.

I thank Ronny Golnak very much, who is one of the early group members. I am greatful for his continued support over all the years and the construction of the detector of the spectrometer. I could always rely on him as a fellow scientist and as a friend.

I thank Jan Metje, Ruba Al-Obaidi and Clemens Richter for helping in the charactrization experiments of the spectrometer and the analysis of the recorded spectra.

Fortunately, I met Tobias Bauer from the Goethe-Universität Frankfurt and his collegues at BESSYII. Being associated with digitizer card manifacturers he lent us one of their amplifiers and helped us optimizing the digitizer card during our spectrometer characterization.

I thank Dr. Andrea Lübcke and Franziska Buchner from Max-Born Institut, who provided me with many practical insights into PES on liquids and scientific

discussions. Thank you for sharing the design of the valve of your spectrometer.

The initial topic of my thesis was the development of laser-pump - soft X-ray-probe experiments for the investigation of ultrafast dynamics in liquids at the synchrotron facility BESSYII at Helmholtz-Zentrum Berlin. Although these experiments were not successful, I want to thank the project leader Dr. Kai Hodeck for all his efforts. I thank Dr. Monika Pawłowska, Dr. Georg Achazi and Dr. Albrecht Lindinger from the group of Prof. Ludger Wöste at Freie Universität Berlin for their active participation in the project and Rainer Schumann from Max-Born Institut for his excellent preparation of the laser system for each beamtime and his detailed instruction to its quirks to maintain measurement condition by ourselves. I also thank the former members of the group Dr. Kathrin Aziz-Lange, Samira Ghadimi, Malte Götz, Stefan Kijak, Dr. René Könnecke and Mikhail Soldatov and for their active participation in the beamtimes and their preparation. Furthermore, I want to thank Dr. Christopher Milne and Dr. Frank van Mourik from the group of Prof. Majed Chergui for their introduction to the experimental details. I am thankful for the preparation of the sample, $Fe(bpy)_3Cl_2$, and chemical analysis was provided by Stefanie Kobialka from the group of Dr. Marianne Engeser from Rheinische Friedrich-Wilhelms-Universität Bonn. I could not have produced the sample another two times without the help of Raul Garcia Diez. I also thank Dr. Iver Lauermann for sharing his chemical laboratory of his group and his advise. In addition, I thank Dr. Joana Salta for drying more than 10 liters of $Fe(bpy)_3Cl_2$ solution to obtain 500g of sample.

I thank the workshop at Freie Universität Berlin, especially its head Detlef Müller, Melanie Klockenberg, Dirk Hund and Micheal Kregielski for their precise and fast work during the construction of the experimental chamber and subsequent improvements. I also thank the workshop at BESSYII for their on-the-fly support of my early steps of the construction until the operation of many instruments like the spectrometer. I thank its head Torsten Wagner, Andreas Drescher, Jörg-Michael Heuser and Oliver Schappeit.

During the experiments at BESSYII many people helped by lending me instruments, tools, by sharing consumables, by assisting in the startup of instruments or by generally giving good scientific or technical advice. These people are: Roland Fleischauer, Dr. Karsten Holldack, Rayk Horn, Dr. Torsten Kachel, Christian Kalus, Oliver Kutz, Mathias Mast, Gert Meyer, Dr. Rolf Mitzner, Dr. Ruslan Ovsyannikov, Olaf Pawlizki, Helmut Pfau, Dr. Ullrich Schade, Wolfram von Scheibner, Robert Schulz, Francois-Xavier Talon and Ronny Trebuth.

I thank Dr. Robert Seidel for his support especially in the last weeks of my writing period.

I enjoyed the pleasant and productive working environment over the years and want to thank Dr. Kaan Atak, Mario Borgwardt, Tim Brandenburg, Munirah Khan, Daniel Tolksdorf, Dr. Tristan Petit, Marvin Pohl, Isaak Unger, Dr. Jie Xiao and Dr. Mikhail Yablonskikh.

Last but not least I would like to thank Hanna for her support and tolerance in many ways and my family and friend in general.